

JGR Solid Earth

RESEARCH ARTICLE

10.1029/2023JB027706

Key Points:

- The north-eastern part of the Isua Supracrustal Belt experienced two metamorphic events at 3.69 Ga and 2.85 Ga and one hydrothermal event at 1.5 Ga
- Banded iron formations acquired a chemical remanent magnetization during the first thermal event that was not entirely overprinted by subsequent events
- Paleomagnetic results hint that a record of the Eoarchean geomagnetic field is preserved in the Isua Supracrustal Belt

Supporting Information:

Supporting Information may be found in the online version of this article.

Correspondence to:

C. I. O. Nichols,
claire.nichols@earth.ox.ac.uk

Citation:

Nichols, C. I. O., Weiss, B. P., Eyster, A., Martin, C. R., Maloof, A. C., Kelly, N. M., et al. (2024). Possible Eoarchean records of the geomagnetic field preserved in the Isua Supracrustal Belt, southern west Greenland. *Journal of Geophysical Research: Solid Earth*, 129, e2023JB027706. <https://doi.org/10.1029/2023JB027706>

Received 21 AUG 2023

Accepted 17 MAR 2024

Author Contributions:

Conceptualization: Claire I. O. Nichols, Benjamin P. Weiss







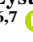

Formal analysis: Claire I. O. Nichols, Benjamin P. Weiss, Athena Eyster, Craig R. Martin, Adam C. Maloof, Nigel M. Kelly, Mike J. Zawaski,

E. Bruce Watson, Daniele J. Cherniak

Funding acquisition: Claire I. O. Nichols, Stephen J. Mojzsis

Investigation: Claire I. O. Nichols, Benjamin P. Weiss, Athena Eyster, Craig R. Martin, Adam C. Maloof, Nigel

Possible Eoarchean Records of the Geomagnetic Field Preserved in the Isua Supracrustal Belt, Southern West Greenland

Claire I. O. Nichols^{1,2} , Benjamin P. Weiss¹ , Athena Eyster³ , Craig R. Martin¹ , Adam C. Maloof⁴ , Nigel M. Kelly⁵ , Mike J. Zawaski^{6,7} , Stephen J. Mojzsis^{6,8,9,10} , E. Bruce Watson¹¹, and Daniele J. Cherniak¹²

¹Department of Earth, Atmospheric and Planetary Sciences, Massachusetts Institute of Technology, Cambridge, MA, USA, ²Department of Earth Sciences, University of Oxford, Oxford, UK, ³Department of Earth and Climate Sciences, Tufts University, Medford, MA, USA, ⁴Department of Geosciences, Princeton University, Princeton, NJ, USA, ⁵Bruker Nano Analytics, Madison, WI, USA, ⁶Department of Geological Sciences, University of Colorado Boulder, Boulder, CO, USA, ⁷Department of Geology and Geophysics, Texas A&M University, College Station, TX, USA, ⁸MTA Centre of Excellence, Origins Research Institute, Research Centre for Astronomy and Earth Sciences (CSFK), Konkoly Observatory, Budapest, Hungary, ⁹Department of Lithospheric Research, University of Vienna UZA 2, Vienna, Austria, ¹⁰Institute for Earth Sciences, Friedrich-Schiller University Burgweg, Jena, Germany, ¹¹Department of Earth and Environmental Sciences, Rensselaer Polytechnic Institute, Troy, NY, USA, ¹²Ion Beam Laboratory, State University of New York at Albany, Albany, NY, USA

Abstract Recovering ancient records of Earth's magnetic field is essential for determining the role of the magnetosphere in protecting early Earth from cosmic radiation and atmospheric escape. We present paleomagnetic field tests hinting that a record of Earth's 3.7-billion-year (Ga) old magnetic field may be preserved in the northeastern Isua Supracrustal Belt as a chemical remanent magnetization acquired during amphibolite-grade metamorphism in the banded iron formation. Multiple petrological and geochronological lines of evidence indicate that the northernmost part of Isua has not experienced metamorphic temperatures exceeding 380°C since the Eoarchean, suggesting the rocks have not been significantly heated since magnetization was acquired. We use “pseudo” baked contact tests (intrusions emplaced 3.26–3.5 Ga ago) and a fold test (folding 3.6 Ga ago) to demonstrate that some samples preserve a ca. 3.7 Ga record of the magnetic field. We recover a field strength of >15 μT. This suggests that Earth's magnetic field may have been weak enough to enhance atmospheric escape during the Archean.

Plain Language Summary Recovering ancient records of Earth's magnetic field is challenging because the magnetization in rocks is often reset by heating during tectonic burial over their long and complex geological histories. We show that rocks from the Isua Supracrustal Belt in West Greenland have experienced three thermal events throughout their geological history. The first event was the most significant, and heated the rocks up to 550°C 3.7-billion-years-ago. The subsequent two events did not heat the rocks in the northernmost part of the area above 380°C. We use multiple lines of evidence to test this claim, including paleomagnetic field tests, the metamorphic mineral assemblages across the area, and the temperatures at which radiometric ages of the observed mineral populations are reset. We use these lines of evidence to argue that an ancient, 3.7 billion year old record of Earth's magnetic field may be preserved in the banded iron formations in the northernmost part of the field area. The magnetization was acquired during mineral transformation associated with the first thermal event and therefore only a lower limit on the strength of the ancient magnetic field was constrained. However, we are able to conclude that the ancient magnetic field was likely comparable with the strength of Earth's magnetic field today.

1. Introduction

Recovering a reliable record of geodynamo strength throughout Earth history is key to understanding the role of magnetic fields in planetary habitability, the thermal evolution of early Earth, and the power sources required to sustain planetary dynamos for billions of years. The geodynamo is currently driven by thermochemical convection in the liquid outer core, although there remains some debate how such a field was sustained for billions of years prior to the onset of core solidification (Landeau et al., 2022; Olson, 2013). The operation of the geodynamo

© 2024 The Authors.

This is an open access article under the terms of the [Creative Commons Attribution-NonCommercial License](https://creativecommons.org/licenses/by-nc/4.0/), which permits use, distribution and reproduction in any medium, provided the original work is properly cited and is not used for commercial purposes.

M. Kelly, Mike J. Zawaski, Stephen J. Mojzsis, E. Bruce Watson
Writing – original draft: Claire I. O. Nichols, Benjamin P. Weiss, Athena Eyster, Craig R. Martin, Adam C. Maloof, Stephen J. Mojzsis
Writing – review & editing: Claire I. O. Nichols, Benjamin P. Weiss, Athena Eyster, Craig R. Martin, Adam C. Maloof, Mike J. Zawaski, Stephen J. Mojzsis, E. Bruce Watson

depends upon the heat flow across the core-mantle boundary, which is a function of both the amount of heat removed by mantle convection and the supply of heat from the core. Recent studies have inferred a gradual decrease in the strength of the dynamo from the Archean until ca. 0.5 Ga based on the existing paleointensity record, which is sparse throughout this time period. These studies propose the inner core began to solidify at the end of this decline (Bono et al., 2019; Davies et al., 2022; Zhou et al., 2022). A relatively young inner core suggests a high core thermal conductivity and a high conductive heat flow of ~15 TW (Landeau et al., 2022). In order for thermal convection to sustain the dynamo prior to inner core nucleation would require the total heat flow out of the core to exceed 15 TW. This heat flow is approaching the upper limit of present day estimates, and would result in an increased number of mantle plumes and a higher degree of mantle melting in Earth's early history suggesting a higher heat flux into the mantle than today. However, petrological observations of both komatiites and cratonic lithosphere suggest secular cooling of Earth with a constant Urey ratio (e.g., constant ratio of radiogenic heating to surface heat flow), indicating the ratio of the heat flux into and out of the mantle has not decreased with time (Herzberg et al., 2010; Lay et al., 2008; Pearson et al., 2021). To reconcile the current paradox, trends in magnetic field strength need to be resolved with greater precision to confirm the age of the inner core. In addition, further work is needed to investigate different dynamo mechanisms and core heat flow requirements for the early geomagnetic field, and whether a decline in, or constant magnetic field strength is expected prior to core solidification (Davies et al., 2022; Landeau et al., 2017).

The preservation of a temperate climate and liquid water on early Earth depends critically upon the strength of the magnetosphere (Sternborg et al., 2011; Tarduno et al., 2014). Recent atmospheric escape models have suggested that both weak (<10 μ T) and strong (>1 mT) magnetic fields could substantially enhance atmospheric escape under present-day solar wind conditions via the polar wind or cusp escape, respectively (Gronoff et al., 2020; Gunell et al., 2018; Lundin et al., 2007). During the Archean, the Sun was rotating faster, generating a stronger stellar dynamo and therefore the solar wind was more intense than today (Vidotto, 2021). An increased solar wind strength causes greater interaction with the upper atmosphere and greater escape of ions assuming a constant level of protection from Earth's magnetosphere. Previous magnetohydrodynamic simulations have suggested that if Earth's magnetic field was half its present day strength 3.5 Ga ago, the area of the polar cap (the area containing open dipolar magnetic field lines, allowing atmospheric escape via the polar wind) could increase by up to 50% (Sternborg et al., 2011). In order to quantify the extent to which atmospheric escape in the Archean was driven by the solar wind, we therefore need robust observations of Earth's magnetic field strength during this time period.

The evolution of Earth's atmosphere played a pivotal role in developing life as we know it; initially the atmosphere was depleted in oxygen (i.e., reduced), creating conditions favorable for the origins of life (Catling & Zahnle, 2020; Sasselov et al., 2020). However, complex life was able to develop following the Great Oxidation Event (GOE) ca. 2.5 Ga, and this may at least in part have been driven by hydrogen loss (Catling, 2013; Zahnle et al., 2013). There is evidence for loss of ionized xenon and hydrogen throughout the Archean (Avice et al., 2018; Zahnle et al., 2013, 2019), and the loss of ionized species is inherently linked to the magnetosphere (Gronoff et al., 2020). In order to assess the extent to which hydrogen and xenon loss were mediated by Earth's magnetic field, we must recover accurate records of its strength prior to 2.5 Ga ago. The maximum amount of hydrogen and xenon escape via the polar wind can be determined from the lower limit on magnetic field strength. Therefore, recovering these limits for the early magnetic field will allow us to determine the relative importance of this escape mechanism for the evolution of Earth's atmosphere prior to the GOE. Atmospheric escape models can rely upon paleomagnetic observations to assess the size of the polar cap under increasing solar wind strengths, and therefore the role of Earth's magnetic field in mitigating or enhancing past atmospheric escape.

Extending the paleomagnetic record back through time becomes increasingly challenging, as ancient rocks have inevitably experienced multiple metamorphic and metasomatic events during their lengthy geological histories. Modern paleointensity studies often focus on fresh lava flows, where the lava acquires a thermal remanent magnetization (TRM) during cooling and crystallization (Valet, 2003). The age of magnetization therefore corresponds to the crystallization age of the lava and a paleointensity can be reliably recovered using thermal demagnetization (Dunlop & Ozdemir, 1993). However, when considering rocks that have undergone metamorphism or metasomatism, rocks will acquire a thermochemical remanent magnetization (TCRM) during mineralogical transformations associated with these events. A TCRM introduces uncertainty in both the timing of magnetization, since the magnetization post-dates the formation age of the rock and, if unrecognized may lead to underestimates of the strength of the recovered magnetization, given that a TCRM has a lower remanence susceptibility than a TRM (Stokking & Tauxe, 1987, 1990).

The previous oldest whole-rock paleomagnetic studies were conducted on rocks from the 3.5 Ga Barberton Greenstone Belt in South Africa and the Duffer Formation, Australia (Biggin et al., 2011; Herrero-Bervera et al., 2016; Tarduno et al., 2010). A paleointensity of 6.4 μT was recovered from the Duffer Formation (Herrero-Bervera et al., 2016), although it remains unresolved whether this value represents a genuinely weak geomagnetic field acquired as a TRM, or a lower estimate on the true paleointensity acquired as a TCRM. Paleomagnetic studies on 4.2–3.2 Ga old single zircon crystals have argued for evidence of an active geodynamo during the Archean and Hadean with a similar field strength to today (Tarduno et al., 2015, 2020, 2023). However, other studies have demonstrated that the magnetic carriers in these zircons are secondary in origin and the magnetization is likely an overprint that post-dates the formation of the zircons by billions of years (F. Tang et al., 2019; Weiss et al., 2015, 2018; Borlina et al., 2020; Taylor et al., 2023). An additional limitation of these single-crystal paleomagnetic studies is that no directional information is preserved (the zircons are detrital). In contrast, for whole-rock samples, the age of magnetization can be assessed using paleomagnetic field tests. The aim of this study is to extend the ancient whole-rock paleomagnetic record beyond 3.5 Ga.

Here, we begin the effort to extend the whole-rock paleomagnetic record to 3.7 Ga ago by recovering natural remanent magnetizations (NRMs) from banded iron formations (BIFs) in the Isua Supracrustal Belt (ISB), southwest Greenland. We compile existing geochronological and petrological observations to determine a thermal history for the ISB and identify three metamorphic and hydrothermal episodes that may have remagnetized these rocks. We present results from paleomagnetic field tests that allow us to verify whether magnetization pre- or post-dates the emplacement of igneous intrusions and folding. We also discuss how the thermal history of the area can be constrained from Pb-Pb isochrons for magnetite, and U-Pb ages for apatite in the BIF.

We argue that the magnetite in Isua should carry a TCRM formed during amphibolite-grade metamorphism ca. 3.7 Ga (Frei et al., 1999; Dymek, 1988; Nutman et al., 2022). The BIF has a whole-rock Rb-Sr age of 3.7 ± 0.14 Ga (Moorbath et al., 1973) and a Pb-Pb apatite age of 3.9 ± 0.2 Ga (Nishizawa et al., 2005). However, it is now commonly accepted that magnetite in BIF is not a primary phase formed directly via precipitation from the water column. Instead, the majority of magnetite in BIFs is now considered to be the product of metamorphism and diagenesis of precursor ferro-ferric oxides and hydroxides (Rasmussen & Muhling, 2018; Konhauser et al., 2017; Nutman, 2017). The magnetite may have grown via direct crystallization, acquiring a CRM by grain growth through a blocking volume (Kobayashi, 1959; Stokking & Tauxe, 1987, 1990). Alternatively, magnetite may have replaced existing phases in the BIF, acquiring a phase-transformation CRM. How this type of CRM becomes magnetized is poorly understood, and in this case is further hampered by the ongoing debate regarding the primary mineralogy in BIFs, which could include green rust, ferrihydrite and greenalite (Halevy et al., 2017; J. E. Johnson et al., 2018; Nutman, 2017; Tosca et al., 2016).

Our results tentatively suggest that the BIF in the northernmost part of the northeastern ISB has escaped metamorphic events exceeding 400°C since 3.7 Ga, and therefore the high temperature component of magnetization preserves a record of the Eoarchean geomagnetic field. We highlight the importance of combining detailed field observations with petrological and geochronological analyses and paleomagnetic field tests; without this context the recovered paleodirections are ambiguous and cannot be reliably interpreted. The approach presented here can now be applied to other Archean terranes in order to build up a robust picture of Earth's earliest geomagnetic field record.

1.1. U-Pb Ages of Magnetite and Apatite as Thermochronometers

The Isua BIF contains abundant magnetite and apatite, for which U-Pb thermochronometry can be used to estimate metamorphic temperatures. U-Pb dating of apatite is a well-established method, and the Isua BIF has previously been dated using this approach (Nishizawa et al., 2005). Magnetite can also contain low but measurable concentrations of U (0.2–0.4 ppm) and Pb (0.2–0.7 ppm) with radiogenic Pb representing ~2% of total Pb (Gelcich et al., 2005). The low amount of U and radiogenic Pb makes it challenging to directly recover a U-Pb isochron from magnetite. However, stepwise leaching allowed both uranium and thorogenic arrays to be successfully recovered and a Pb-Pb isochron to be calculated (Frei et al., 1999).

The apatite observed in the Isua BIF is considered to be associated with early hydrothermal events ca. 3.63 Ga (Frei et al., 1999). Three previous studies have investigated the potential of Pb-Pb dating for magnetite in BIFs (Erel et al., 1997; Frei et al., 1999; Frei & Polat, 2007). These studies were carried out on the Isua BIF and the Brockman Iron Formation from the Hamersley basin, western Australia. Studies on the Isua BIF recovered Pb-Pb

isochron ages of 3.691 ± 0.049 Ga and 3.691 ± 0.022 Ga (Frei et al., 1999; Frei & Polat, 2007). The Pb-Pb age of the magnetite has not been perturbed or reset since this early metamorphic event and no additional magnetite nucleation or growth since this time. However, previous studies were unable to interpret these ages in terms of the subsequent thermal history of the area, since the Pb diffusion rate in magnetite was unconstrained.

Based on Pb diffusion measurements for apatite and magnetite (Cherniak et al., 1991; E. B. Watson et al., 2023), assuming a maximum cooling rate of $100^\circ\text{C Ma}^{-1}$ following peak metamorphic conditions (Figures S1 and S2 in Supporting Information S1), and a maximum grain size of 27 and 100 μm for magnetite and apatite in the Isua BIF, respectively (Figures S3 and S4 in Supporting Information S1), we estimated the peak closure temperature for each system. Pb-Pb isochrons for magnetite will be reset by heating to $>380^\circ\text{C}$, and U-Pb ages in apatite will be reset by heating to $>530^\circ\text{C}$. Since both of these temperatures are below the Curie temperature for magnetite (580°C), these serve as useful reference points for assessing which thermal events may have remagnetized the Isua BIF.

1.2. Geologic Setting

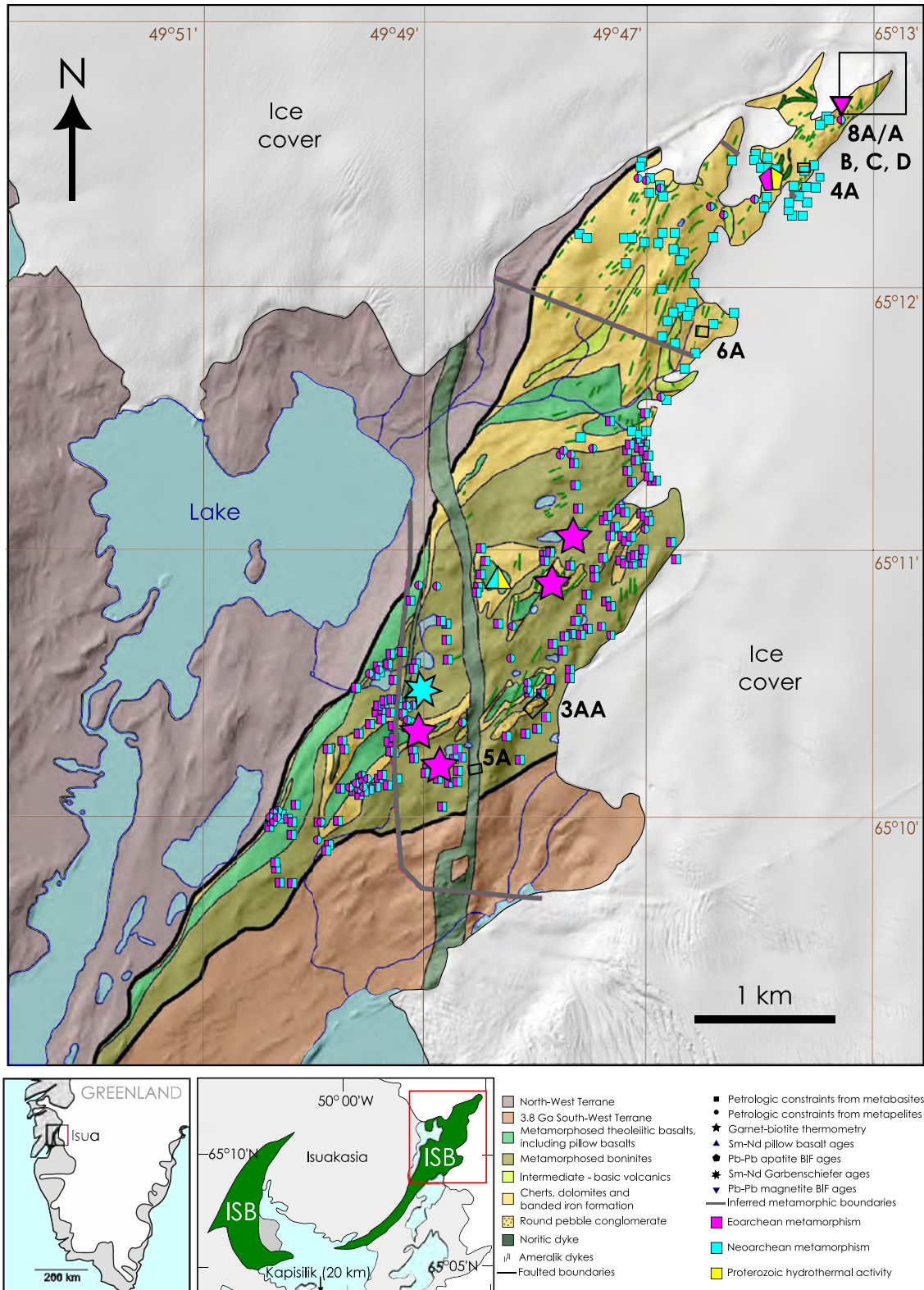
The northeastern part of the ISB is subdivided into three main terranes separated by faults (Figure 1). The 3.7 Ga northern terrane, the focus of this study, is sandwiched between a northwest terrane and the 3.8 Ga southwest terrane (Nutman & Friend, 2009). The southern part of the northern terrane is dominated by metamorphosed boninites, interspersed with dolomites, conglomerates, and basalts. Further north in the field area, magnetite-bearing cherts begin to dominate, and the northernmost extent of the area is almost exclusively made up of BIF. These 3.7 Ga sediments and volcanics were intruded by dykes that are assumed to be part of the Ameralik dyke swarm (based on their composition, distribution and thickness; see Discussion for further details) emplaced 3.26–3.5 Ga ago (ages constrained by U-Pb zircon dating) across much of the Nuuk district of southwest Greenland (Nutman et al., 2004; Nutman & Friend, 2009). The final major intrusive event in the area was the emplacement of a large (>100 m wide) noritic dyke, which trends north-south across the northeast part of the ISB cross-cutting all the major lithologies (Nutman & Friend, 2009). Zircons from the dyke have a U-Pb age of 2.214 ± 0.010 Ga (Nutman et al., 1995).

The Isua BIF, the main focus of this study, has a simple mineralogy comprised of alternating bands of quartz and magnetite with minor amphibole at the boundary between the two phases. The northernmost part of the northeast ISB (north of $65^\circ11'N$) is exceptionally well preserved, with localized regions of low-strain where pillow structures and original sedimentary features are still observable (Nutman & Friend, 2009). We outline several lines of evidence below that suggest this part of the belt (Figure S5 in Supporting Information S1) only experienced one significant ($>380^\circ\text{C}$) metamorphic event ca. 3.69 Ga.

The northern terrane has experienced two metamorphic events during the Eoarchean and Neoproterozoic, and a hydrothermal event during the Proterozoic, evidence for each event is summarized in Table 1. The temperature and timing of the events are summarized in Figure 2. The Eoarchean metamorphic event was upper-greenschist to amphibolite grade, resulting in the formation of a single generation of garnets (Rollinson, 2003) and the growth of grunerite and magnetite in the BIF at 3.69 Ga (Dymek, 1988; Frei et al., 1999). Garnet-biotite thermometry indicates a peak temperature of 470 – 550°C (Rollinson, 2002). This metamorphic event was likely the result of the collision between the 3.7 Ga northern terrane and the 3.8 Ga southern terrane at 3.69–3.66 Ga based on zircon U-Pb ages (Nutman & Friend, 2009).

A Neoproterozoic metamorphic event followed the juxtaposition of the Isukasia and Kapisilik terranes occurred ca. 2.98–2.95 Ga (Nutman et al., 2015; Frei et al., 1999; Gruau et al., 1996; Polat et al., 2003). The metamorphic grade increases from north to south toward the mylonitized region between the two terranes, which lies >20 km south of the ISB. The southernmost part of the ISB experienced temperatures of 500 – 600°C (Gruau et al., 1996). However, peak metamorphic temperatures in the northernmost region remained below 380°C , since neither the BIF apatite or magnetite Pb-Pb ages were reset during this time period (Nishizawa et al. (2005); Frei et al. (1999)). The Ameralik dykes were metamorphosed in this event, with their doleritic assemblage being transformed to actinolite, chlorite, epidote and magnetite-bearing assemblage, indicating lower greenschist grade metamorphism (360 – 400°C ; Komiya et al. (2004); Arai et al. (2014)).

A subsequent thermal perturbation at 1.5–1.6 Ga is not observed in most of the metamorphic assemblages across the area, with the 2.2 Ga noritic dyke retaining its primary igneous mineralogy (Nutman et al., 2022). The only



evidence for this later event is in a partial resetting of the Pb-Pb apatite age in the BIF, and the complete resetting of the Rb-Sr age in the pillow basalts (Nishizawa et al., 2005; Polat et al., 2003). Since neither system has undergone complete homogenization and resetting, this event is interpreted to have been a low temperature ($\sim 320^\circ\text{C}$) overprint and not sufficient to produce new mineral growths or reaction rims on the existing metamorphic mineral assemblages.

1.3. Sample Lithologies

In the southern part of the northeast ISB are outcrops of a round pebble conglomerate (Site 3AA). This conglomerate is sedimentary in origin (Fedo, 2000), with beds defined by variations in the matrix grain size. The conglomerate is made up of rounded clasts that vary from 0.5 to 30 cm in diameter. Pebble clasts have been rotated into the cleavage plane and stretched parallel to this foliation, which most likely developed during Neoproterozoic metamorphism and the collision of the Isukasia and Kapisilik terranes. The clasts have a range of lithologies including amphibolite, quartzite, iron formation, felsic volcanic and sandstone comprised of mafic grains. The conglomerate also contains quartz veins that are boudinaged and comprise crystalline quartz, whereas the quartzite clasts still preserve remnants of individual quartz grains, and variations in grain size within each clast. The variety in the composition, dimensions and morphology of the clasts was used to argue against a purely tectonic origin for the conglomerate (Fedo et al., 2001; Nutman et al., 1984). The conglomerate was metamorphosed to amphibolite grade with peak temperatures of 500–600°C during both the Eoarchean and Neoproterozoic tectonothermal events (Table 1).

A large (>100 m wide) noritic dyke trends north-south across the northeast part of the ISB, cross-cutting all the major lithologies (Nutman & Friend, 2009). Zircons from the dyke have a U-Pb age of 2.214 ± 0.010 Ga (Nutman et al., 1995). This intrusion is a useful target to assess the extent of remagnetization during the Proterozoic metamorphic event. The dyke primarily is composed of coarse, crystalline orthopyroxene, clinopyroxene and plagioclase. The pyroxenes have been partially altered to amphiboles, and the larger crystals are surrounded by a matrix of quartz, K-feldspar, plagioclase, Fe-Ti oxide, hornblende and apatite (Nutman et al., 1995).

BIF forms the northernmost part of field area (Figure 1). It varies from a magnetite-bearing chert to a typical BIF with alternating layers of magnetite and quartz with varying amounts of amphibole and carbonate. The BIF has been variably categorized depending on its mineral assemblage (Aoki et al., 2016; Dymek, 1988). Here, we define BIF as the quartz-magnetite formation defined by Dymek (1988) and the gray-type BIF defined by Aoki et al. (2016). Two generations of magnetite are observed in the BIF, both of which were formed after primary deposition of Fe-clays such as greenalite (Nutman, 2017). The first generation of magnetite replaced the primary mineralogy in the original depositional bands yields a Pb-Pb age of 3.69 ± 0.22 Ga (Frei et al., 1999). A subsequent hydrothermal event at 3.63 ± 0.07 Ga introduced secondary veins of magnetite into the BIF as well as pyrite and apatite (Frei et al., 1999; Nishizawa et al., 2005).

The BIF in the northeast region of the ISB is intruded by part of the Ameralik dyke swarm (Nutman & Friend, 2009), which was emplaced 3.26–3.5 Ga ago across much of the Nuuk district of southwest Greenland (Nutman et al., 2004). We assume that the dykes intruding the BIF are all part of the Ameralik dyke swarm, and refer to them all as Ameralik dykes although previously in the literature some have been referred to as Tarsartôq dykes (White et al., 2000; Nutman et al., 2004; Nutman, 1986). These dykes are mafic in composition and variably deformed and boudinaged, and primary intrusive contacts with the country rock often are sheared (Nutman et al., 2004). The Ameralik dykes were emplaced after the Eoarchean metamorphic events that generated the magnetite in the primary depositional banding in the BIF (Dymek, 1988; Frei et al., 1999), but prior to subsequent Neoproterozoic metamorphism and Proterozoic hydrothermal events. The original mineral assemblage in

Figure 1. A simplified geological map [after Nutman and Friend (2009)] depicts the northeastern part of the ISB. The two smaller maps show the entire extent of the ISB and its location in Greenland. Previous tectonothermal constraints on the metamorphic history of the ISB are shown by the colored symbols, where pink, blue and yellow colors represent evidence for Eoarchean metamorphism, Neoproterozoic metamorphism and Proterozoic hydrothermal activity, respectively. Petrological constraints from metabasites (squares) and metapelites (circles) and the inferred metamorphic boundaries (gray lines; Arai et al. (2014); Komiya et al. (2002)); garnet-biotite thermometry (5-point stars; Rollinson (2002, 2003)); Sm-Nd pillow basalt ages (upwards pointing triangle; Polat et al. (2003)); Pb-Pb apatite ages (pentagon; Nishizawa et al. (2005)); Sm-Nd plagioclase amphibole ages (7-point star; Gruau et al. (1996)); and Pb-Pb magnetite BIF ages (downwards pointing triangle; Frei et al. (1999); Frei and Polat (2007)). The sites where paleomagnetic data were collected as part of this study are labeled 8A/A, B, C, D, 3AA, 4A, 5A and 6A.

Table 1

A Summary of the Evidence for Each of the Three Metamorphic Events Experienced by the Northeast Isua Supracrustal Belt

Eoarchean metamorphic event (ca. 3.69–3.63 Ga)	
The BIF was transformed to an assemblage containing grunerite, cummingtonite, actinolite and magnetite indicating amphibolite grade metamorphism.	Dymek (1988)
Magnetite in the BIF in the northern ISB has a Pb-Pb age of 3.69 Ga.	Frei et al. (1999); Frei and Polat (2007)
Garnet grew during a single metamorphic event at temperatures between 470 and 550°C based on garnet-biotite geothermometry.	Rollinson (2002, 2003)
Apatite and cross-cutting veins of magnetite formed in the BIF at ca. 3.63 Ga during hydrothermal activity	Frei et al. (1999)
Neoproterozoic Metamorphic Event (ca. 2.85 Ga)	
Sm-Nd ages in pillow basalt rims was reset to 2.567 Ga in the southern part of the northeast ISB.	Polat et al. (2003).
The Pb-Pb apatite ages in the banded iron formation are not impacted by this event, suggesting a peak metamorphic temperature below 530°C in northern part of ISB.	Nishizawa et al. (2005).
Ameralik dykes (emplaced 3.26–3.5 Ga) retain primary igneous textures and are only weakly metamorphosed to a greenschist grade assemblage in the northern part of ISB and so must post-date the amphibolite grade event.	A. Nutman et al. (2015); Arai et al. (2014)
Pb-Pb magnetite ages in BIF in the southwestern part of the ISB are reset to 2.84 ± 0.05 Ga. (This age is not recovered in the BIF in the northeastern part of the ISB.)	Frei et al. (1999)
Sm-Nd plagioclase and amphibole ages from the Garbenschiefer unit in the southern part of the ISB are 2.849 ± 0.116 Ga, indicating a metamorphic temperature of 500–600°C.	Gruau et al. (1996)
Proterozoic Hydrothermal Event (ca. 1.5–1.6 Ga)	
Perturbation of Pb-Pb apatite age ca. 1.5 Ga in the BIF suggests an event below 530°C. The Pb-Pb age of magnetite in the BIF was not perturbed by this event, suggesting peak temperatures below 380°C in the northernmost part of the northeast ISB.	Nishizawa et al. (2005); Frei et al. (1999); E. B. Watson et al. (2023)
Perturbation of the Sm-Nd age and resetting of the Rb-Sr errorchron in pillow basalt rims at 1.604 Ga indicates a hydrothermal temperature of $\sim 320^\circ\text{C}$.	Polat et al. (2003)
The 2.2 Ga noritic dyke retains its primary igneous mineralogy, indicating no substantial metamorphism after this time, and only hydrothermal alteration.	Nutman et al. (2022)

the Ameralik dykes contained no magnetite and large multidomain magnetite crystals are thought to have formed during Neoproterozoic greenschist grade metamorphism (Nutman et al., 2004).

2. Materials and Methods

2.1. Paleomagnetic Sampling and Field Tests

We conducted two field campaigns to the ISB between 29 July–6 August 2018 and 16 July–27 July 2019. We carried out geological mapping and collected oriented drill cores and block samples of the pebble conglomerate, the norite dyke, and six sites where mafic Ameralik dykes intrude the BIF. A total of three-hundred-and-eight specimens were used for subsequent paleomagnetic analysis (Table 2).

Sampling was carried out using a water-cooled Pomeroy EZ Core Drill to extract 2.5-cm-diameter cores. Cores were oriented using a Pomeroy Orienting Fixture and both magnetic and sun compass readings were taken. We primarily relied upon sun compass readings, since the BIF generated strong localized magnetic fields which disturbed magnetic compass readings. Cores were extracted using copper beryllium alloy chisels to avoid remagnetizing the specimens.

Conglomerate tests, pseudo-baked contact tests and a fold test were conducted at various sites (Table 2) within the field area (Buchan, 2007; Graham, 1949). For the conglomerate test, individual clasts were drilled, as well as the surrounding matrix. For the pseudo-baked contact tests, both the middle and edge of the dykes were drilled, although chilled margins were not obviously visible. The surrounding country rock was drilled at regular intervals

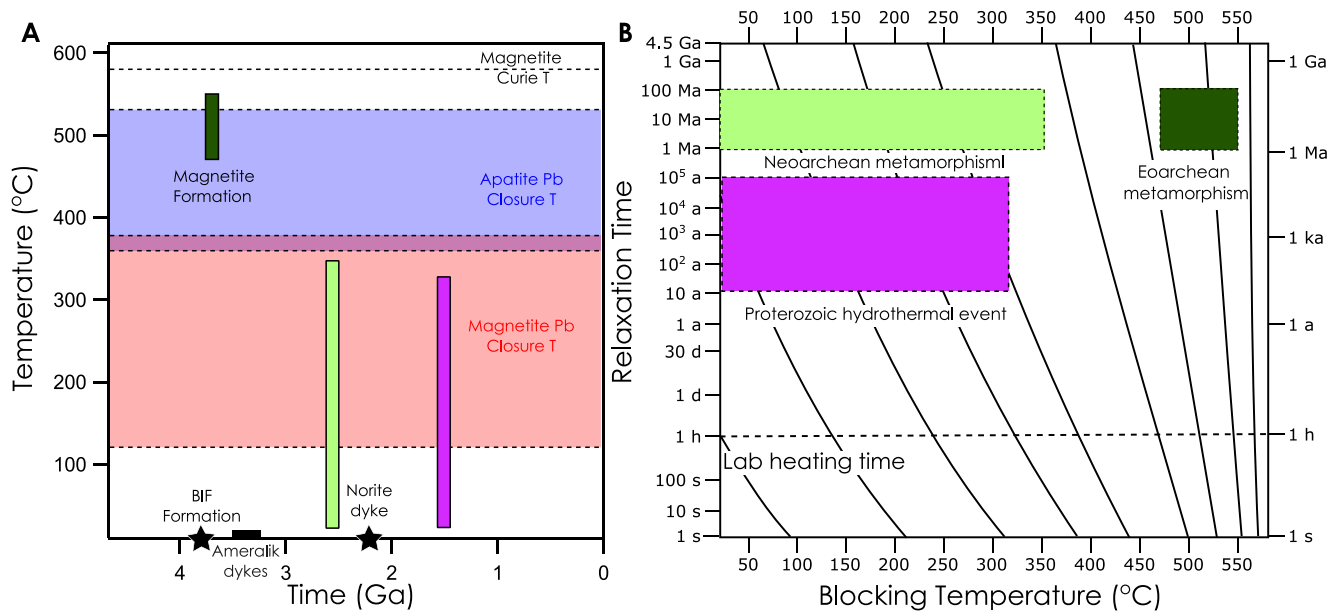


Figure 2. The thermal history of the ISB. (a) The BIF formed ca. 3.7 Ga ago and subsequently experienced an amphibolite grade metamorphic event. This metamorphic event resulted in magnetite growth in the BIF that acquired a TCRM, and set the U-Pb ages for both the magnetite and apatite. The Ameralik dykes were subsequently emplaced, and later experienced greenschist-grade, Neoproterozoic metamorphism. Neither the magnetite nor the apatite U-Pb ages were perturbed by this event, suggesting the maximum metamorphic temperature was below the closure temperature for both systems. A large norite dyke was then emplaced 2.2 Ga ago, and experienced hydrothermal alteration ca. 1.5 Ga ago although its igneous mineralogy was retained. The magnetite U-Pb ages were not perturbed this event, but the apatite U-Pb age was partly altered due to modification by hydrothermal fluids. (b) A Pullaiah diagram (Pullaiah et al., 1975) showing the blocking time as a function of temperature for single domain magnetite. This diagram shows that remanence acquired in any of the metamorphic events can be unblocked in the laboratory during heating times of 1 hr up to temperatures <580°C. The diagram indicates that the Neoproterozoic and Proterozoic events cannot entirely thermally overprint the magnetization carried by single domain grains during Eoarchean metamorphism even during events lasting of order 100 Ma, although they may result in thermal overprints <450°C.

of 0.3–1 m, preferentially targeting regions of rock that were absent of fractures, deformation or veining (Figure S6 in Supporting Information S1). Specimens were acquired up to >3 radii from the dyke to ensure sufficient sampling in the unbaked regions. Each area was explored in detail to ensure no other dykes existed close to the unbaked region which may have influenced the recovered paleomagnetic signals. Watson's V_W statistic was used to determine if paleomagnetic directions close to and far from the dyke have distinct directions. Fold tests were carried out on unbaked BIF directions that passed Watson's V_W test (Tauxe et al., 1991).

Table 2
A Summary of the Sites Where Paleomagnetic Field Tests Were Carried out

Site	Location		No. of specimens measured	Paleomagnetic field test
	Latitude (° N)	Longitude (° W)		
3AA	65.1744	49.8000	28	Conglomerate test - round pebble conglomerate
5A	65.1689	49.8074	8	Paleodirection - norite dyke
4A	65.2073	49.7589	32	Baked contact test - BIF and Ameralik dyke
6A	65.1982	49.7740	25	Baked contact test - BIF and Ameralik dyke (boudinaged)
8A/A	65.2095	49.7579	46	Baked contact test - BIF and Ameralik dyke
B	65.2111	49.7528	54	Baked contact test - BIF and Ameralik dyke
C	65.2106	49.7528	32	Baked contact test - BIF and Ameralik dyke
D	65.2115	49.7533	46	Baked contact test - BIF and Ameralik dyke

Note. All GPS coordinates are given for the World Geodetic System 1984 (WGS84).

2.2. Paleomagnetic Analyses

Drill cores were cut into ~1-cm thick discs using an ASC Scientific dual-blade rock saw at MIT. BIF samples were further cut down to ~1-mm thick slices using a Buehler IsoMet[®] low speed saw in the MIT Paleomagnetism Laboratory due to their exceptionally strong magnetic moments. Other lithologies (conglomerate clasts, matrix and Ameralik dykes) were measured as 1-cm thick discs. Specimens were measured using the 2G Enterprises superconducting quantum interference device (SQUID) rock magnetometer, housed in a magnetically-shielded room made of mu-metal with a background DC field of <200 nT in the MIT Paleomagnetism Laboratory.

Specimens were demagnetized sequentially using several techniques; a subset of specimens were initially placed in liquid nitrogen to remove the majority of the multidomain component (Halgedahl & Jarrard, 1995). In all cases where a liquid nitrogen step was carried out, a sister specimen was also demagnetized without this step in order to ensure this did not introduce any bias into the recovered data. All specimens were then alternating field (AF) demagnetized in steps of 2 mT from 2 to 10 mT along three orthogonal axes using inline coils housed within the magnetometer to clean the specimens of low-coercivity, unstable multidomain components. Specimens were then thermally demagnetized in an ASC Scientific TS-48SC thermal demagnetization oven between 100 and 580°C in gradually decreasing temperature steps ranging from 50 to 5°C. Samples were heated for 1 hr to ensure any magnetization carried by single domain grains acquired during metamorphic events lasting between 10³–10⁶ years was unblocked (Pullaiah et al., 1975).

Stable components of magnetization were identified using principal component analysis (Kirschvink, 1980). Stable, origin-trending components were defined as those where the maximum angular deviation (MAD) is greater than the deviation angle (dAng), and both values are small. Component directions were plotted in geographic coordinates in Stereonet (Allmendinger et al., 2013; Cardozo & Allmendinger, 2013), and Fisher statistics calculated to constrain the mean and α_{95} for each related group of specimens. Where the degree of scatter was large, a Watson test for randomness was also conducted (G. S. Watson, 1965).

A suite of sister specimens was AF demagnetized along three orthogonal axes from 0 to 145 mT in steps of 5 mT, with a small subset demagnetized up to 400 mT in steps of 100 mT between 200 and 400 mT to identify high-coercivity components. Three specimens (A05c, A07c, and C02b) were used for pseudo-Thellier experiments. A 50 μ T anhysteretic remanent magnetization (ARM) applied under a 260 mT AF and 40 mT isothermal remanent magnetization (IRM) were imparted to each specimen and then AF demagnetized up to 145 mT. Demagnetization of the ARM was compared to demagnetization of the NRM to calculate paleointensities, B_{anc} , using

$$B_{anc} = \frac{\Delta NRM}{\Delta ARM} \frac{B_{lab}}{a} \quad (1)$$

where $a = 3.28$ is the calibration factor for magnetite (Paterson et al., 2016). For some specimens, the NRM demagnetization had multiple directional components in opposing directions, resulting in substantial curvature in the orthographic demagnetization plots. To remove this curvature, vector subtraction was used to isolate the moment magnitude in order to calculate $\frac{\Delta NRM}{\Delta ARM}$. The ARM demagnetization was also compared to the IRM demagnetization to verify the paleointensity recording fidelity of the BIF specimens. The recovered paleointensity, B_{rec} , was estimated using the following:

$$B_{rec} = \frac{\Delta ARM}{\Delta IRM} f \quad (2)$$

where $f = 3,000$ (Gattacceca & Rochette, 2004).

The recovered paleointensities were combined to find a weighted average and uncertainty using the following equations:

$$\bar{\mu} = \frac{\sum_{n=1}^i w_i \mu_i}{\sum_{n=1}^i w_i} \quad (3)$$

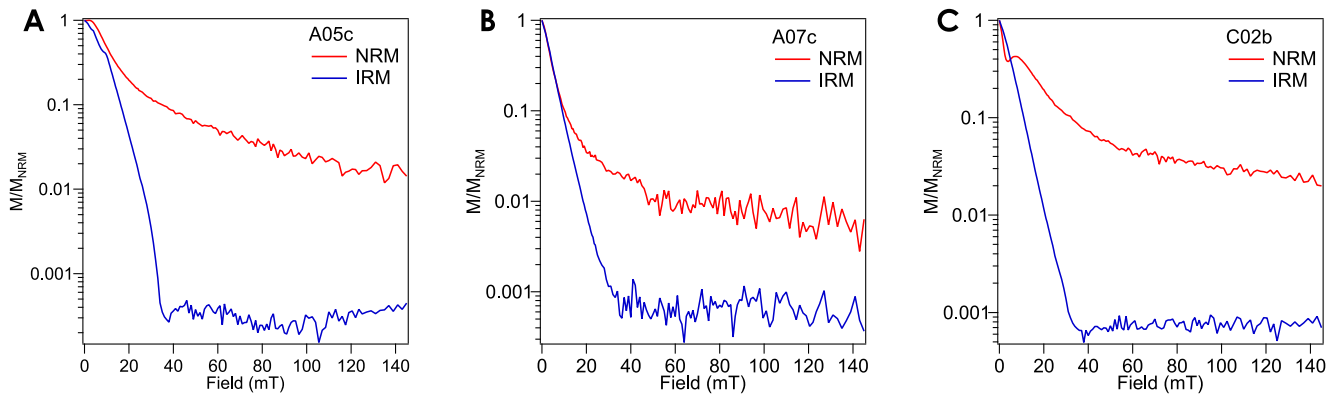


Figure 3. Results of a Lowrie test conducted to determine whether the NRM in BIF specimens is carried by MD or SD grains. The NRM and IRM were demagnetized up to 145 mT. For all three specimens shown, (a) A05c, (b) A07c and (c) C02b, the NRM is retained to higher alternating fields than the IRM, indicating that the NRM is predominantly carried by single-domain magnetite.

where $\bar{\mu}$ is the weighted mean, $w_i = \frac{1}{\sigma_i^2}$ where σ_i is the standard deviation recovered for each individual paleointensity measurement, and μ_i is each recovered paleointensity value. The weighted uncertainty is then calculated using:

$$\bar{\sigma} = \sqrt{\left(\frac{\sum_{n=1}^i w_i (\mu_i - \bar{\mu})^2}{\frac{n-1}{n} \sum_{n=1}^i w_i} \right)} \quad (4)$$

where n is the number of specimens.

2.3. Rock Magnetic Analyses

First-order reversal curve (FORC) diagrams, hysteresis loops, and backfield curves were measured using a Lakeshore Princeton Measurements Corporation (PMC) MicroMag 2900 Series alternating gradient magnetometer (AGM) at the University of Cambridge. Five BIF specimens (4A11, 6A09, 6A15, 8A06 and 8A19) were measured. FORCs were measured with a saturating field H_{sat} of 1 T in field steps of 2 mT. A total of 263 curves were measured with an averaging time of 300 ms. FORC diagrams were processed using the software package FORCinel (Harrison & Feinberg, 2008). Hysteresis loops were measured up to saturating fields of 0.5–1 T in order to calculate the hysteresis parameters M_{rs} , M_s , and H_c which are the saturation remanent magnetization, saturation magnetization and coercivity, respectively. H_{cr} , the coercivity of remanence, was calculated from the backfield curve when the magnetization is zero. Backfield curves were measured up to a saturating field of 1 T. Backfield curves were also used to estimate the coercivity spectra of each population of magnetite grains within each specimen using MAX UnMix (Maxbauer et al., 2016).

3. Results

3.1. Paleomagnetic Carriers

In the BIF samples, scanning electron microscopy (SEM) and petrological analyses revealed that the magnetic carrier is magnetite (Figures S4 and S10 in Supporting Information S1), consistent with a sharp drop in magnetization close to 580°C. The domain state of magnetite in the BIF was characterized by comparing AF and thermal demagnetization, backfield curves and a Lowrie test (Lowrie & Fuller, 1971). The Lowrie test (Figure 3) showed that AF demagnetization of the NRM was significantly more stable than demagnetization of a 40 mT IRM, suggesting that the NRM is primarily carried by stable, single-domain magnetite grains. However, given that the validity of the Lowrie test rests on the form of single grain anisotropy, this conclusion is somewhat uncertain (Newell, 2000). Furthermore, all specimens plot in the multidomain (MD) region of the Day plot, and the FORC diagrams also revealed predominantly MD behavior (Figure 4) suggesting that the single domain (SD)

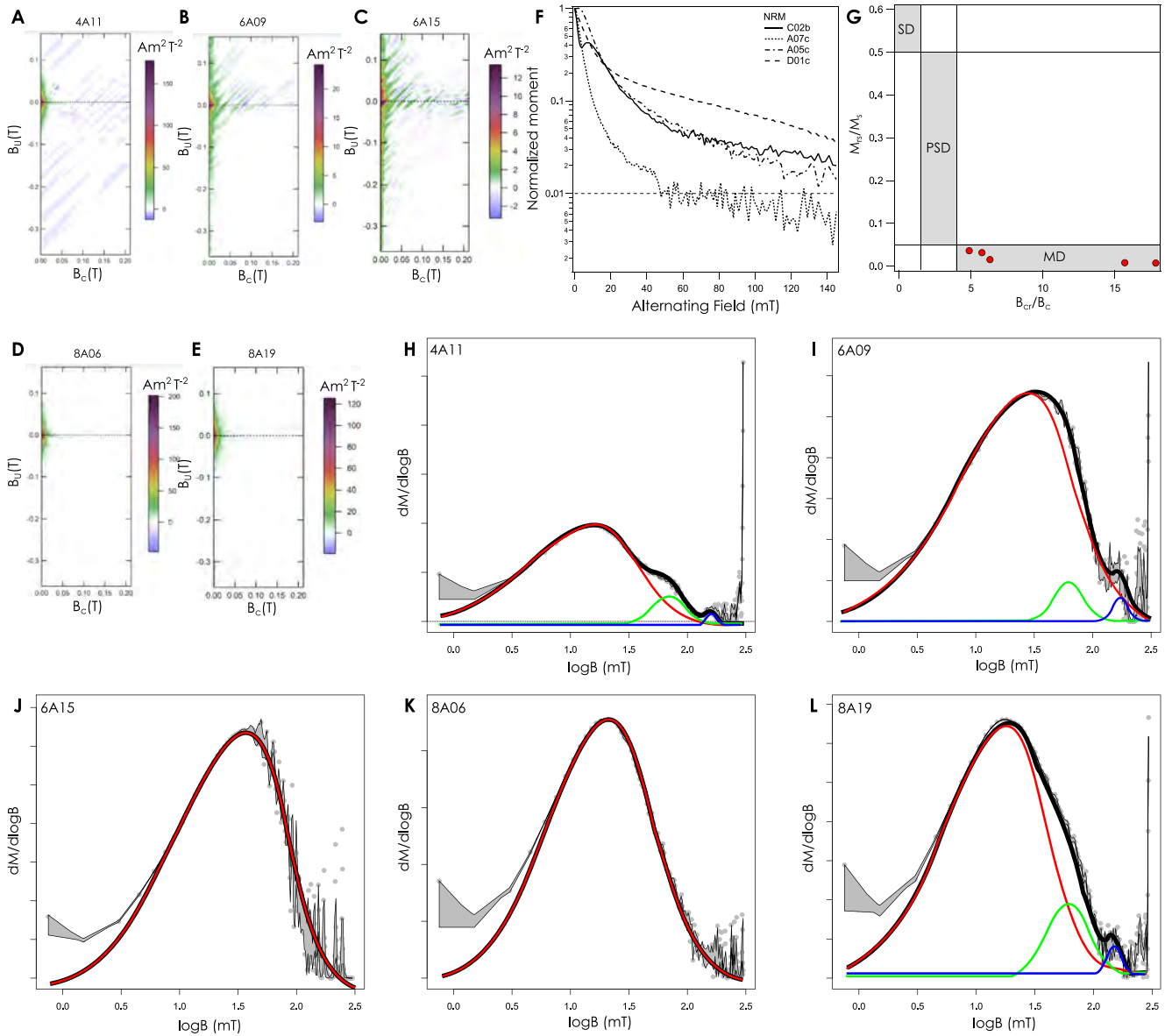


Figure 4. Rock magnetic analyses on banded iron formation specimens. (a), (b), (c), (d), and (e) show first order reversal curve (FORC) diagrams for specimens 4A11, 6A09, 6A15 and 6A19, respectively. In all cases, the FORC diagrams exhibit typical MD behavior, with the signal predominantly spread out over the vertical axis. However, (f) shows that during AF demagnetization, remanence is removed up to fields exceeding 145 mT suggesting stable SV or SD grains are present. (g) A Day plot summarizing the hysteresis behavior of the samples. (h–l) show coercivity distributions derived from backfield demagnetization curves (i.e., demagnetization from saturation state). Three populations of magnetite grains are identified by best-fit Gaussian curves which represent MD (red) and SD/SV (blue/green) populations, respectively.

grains carrying the remanence represent a small proportion of the total population of magnetite grains. SEM images and low temperature demagnetization also demonstrate that the vast majority of magnetite grains have a diameter between 1 and 26 μm (Figures S3 and S4 in Supporting Information S1). Multidomain magnetite was efficiently demagnetized at low field strengths of <10 mT (Hodych, 1982). During NRM demagnetization, multiple directions were recovered representing different directional components of magnetization. Both the high temperature (HT; >400°C) and high-coercivity (HC; >60 mT) components in the BIF were found to be similar (Figure S7 in Supporting Information S1). HT directions are also slightly influenced by low-coercivity, multidomain overprints which are not effectively removed during thermal demagnetization. Backfield curve acquisition revealed three populations of magnetite grains (Figure 4, Table S1); the largest population (64%–100% of grains) is dominated by grains with a mean coercivity of ~10–20 mT, suggesting they are multidomain. A second

population (15%–27% of grains) has a mean coercivity ranging from ~60–70 mT and a third population (<10% of grains) has a mean coercivity of >150 mT. These higher coercivity grains are likely stable single domain or single vortex (SV) magnetite grains (Hodych, 1982).

The NRMs of four lithologies were subjected to thermal demagnetization: conglomeratic clasts (of varying mineralogy, with most being quartz-rich), the norite dyke, dolerite dykes (part of the Ameralik dyke swarm) and the BIF. Thermal demagnetization shows that for the conglomerate clasts and dolerite, the majority of NRM is removed between 300 and 400°C (Figures S8 and S9 in Supporting Information S1). In the norite dyke the majority of magnetization is removed between 500 and 600°C. The magnetic carriers in the norite dyke are thought to carry a primary TRM acquired during initial cooling of the intrusion. However, the magnetic carriers in the conglomerate clasts, Ameralik dykes and BIF are thought have been altered during metamorphism and therefore the magnetization is interpreted as a TCRM imparted during greenschist to amphibolite grade metamorphism (450–550°C). In the BIF, AF demagnetization removed NRM with an intensity <0.1 times that for isothermal remanent magnetization (IRM), indicating that specimens have not been lightning remagnetized (Figure 3).

3.2. Conglomerate Test

A conglomerate test (Site 3AA) was carried out (Figure 1) in the southern part of the area, that experienced amphibolite grade metamorphism in both the Eoarchean and Neoarchean metamorphic events (Table 1). Twenty-five clasts and three matrix specimens were demagnetized up to 585°C (Table S2; Figure S8 in Supporting Information S1). The vast majority of specimens exhibited unstable demagnetization behavior shown by high MAD values $\gg 10^\circ$. Ten clasts and one matrix specimen exhibited at least two clear stable components, at least one of which had a MAD $< 10^\circ$. Eight clasts exhibited a stable high temperature (HT; up to 350°C) component. A test for randomness was carried out on recovered HT directions from these eight clasts. The length of the eight resultant vectors $R = 6.35$ exceeds $R_o = 5.26$, demonstrating that the hypothesis of randomness can be rejected with $p = 0.01$ significance (G. S. Watson (1965); Table S3). Twelve low temperature (LT) components ($T < 100^\circ\text{C}$) from nine clast specimens gave a resultant vector $R = 7.69$ which exceeds $R_o = 6.55$, indicating that the hypothesis of randomness can be rejected. The LT and HT directions defined by the clasts are also similar ($83^\circ/281^\circ$, $\alpha_{95} = 25^\circ$ and $61^\circ/300^\circ$, $\alpha_{95} = 31^\circ$, respectively) suggesting both the HT and LT components have experienced the same overprint (Figure S8 in Supporting Information S1). None of the samples showed a stable component that extended significantly beyond 350°C. The conglomerate test therefore fails and demonstrates that the conglomerate has been remagnetized in later metamorphic events following its original deposition, most likely during both the Eoarchean and Neoarchean metamorphic events, both of which reached amphibolite grade in the southern part of the area.

3.3. Norite Dyke

Eight specimens (including three sister specimens) of the norite dyke were demagnetized up to 580°C (Table S4). The norite dyke shows two distinct types of demagnetization depending on whether samples were collected close to the dyke edge (specimens 5A03, 5A04 and 5A05, collected within 2.4 m of the contact) or from the dyke center (specimens 5A25 and 5A26, collected more than 10 m from the contact). The majority of magnetization is removed close to 580°C, indicating that magnetite is the dominant magnetic carrier. In samples from the dyke center, magnetization drops off more steeply at slightly higher temperatures (Figure 5). Three stable components of magnetization were identified in all norite dyke specimens, with a HT component above 565°C, a medium temperature (MT) component between 510 and 565°C and a LT component between 0 and 375°C. For the specimens from the dyke center, the LT, MT and HT directions are $83^\circ/011^\circ$, $\alpha_{95} = 11^\circ$; $67^\circ/018^\circ$, $\alpha_{95} = 22^\circ$; and $87^\circ/002^\circ$, $\alpha_{95} = 15^\circ$, respectively (Figure 5). These directions are indistinguishable from the present-day magnetic field direction in Isua ($75^\circ/000^\circ$), suggesting that the center of the dyke contains predominantly MD magnetite that has acquired a viscous remanent magnetization from the present-day field.

For the specimens from the dyke edge, the LT, MT and HT components are $49^\circ/025^\circ$, $\alpha_{95} = 18^\circ$; $41^\circ/095^\circ$, $\alpha_{95} = 4^\circ$; and $31^\circ/069^\circ$, $\alpha_{95} = 16^\circ$, respectively (Figure 5). The HT and MT directions are similar to one another, and likely reflect remanence acquired during emplacement of the norite dyke 2.2 Ga. The LT component is distinct from the present-day magnetic field direction.

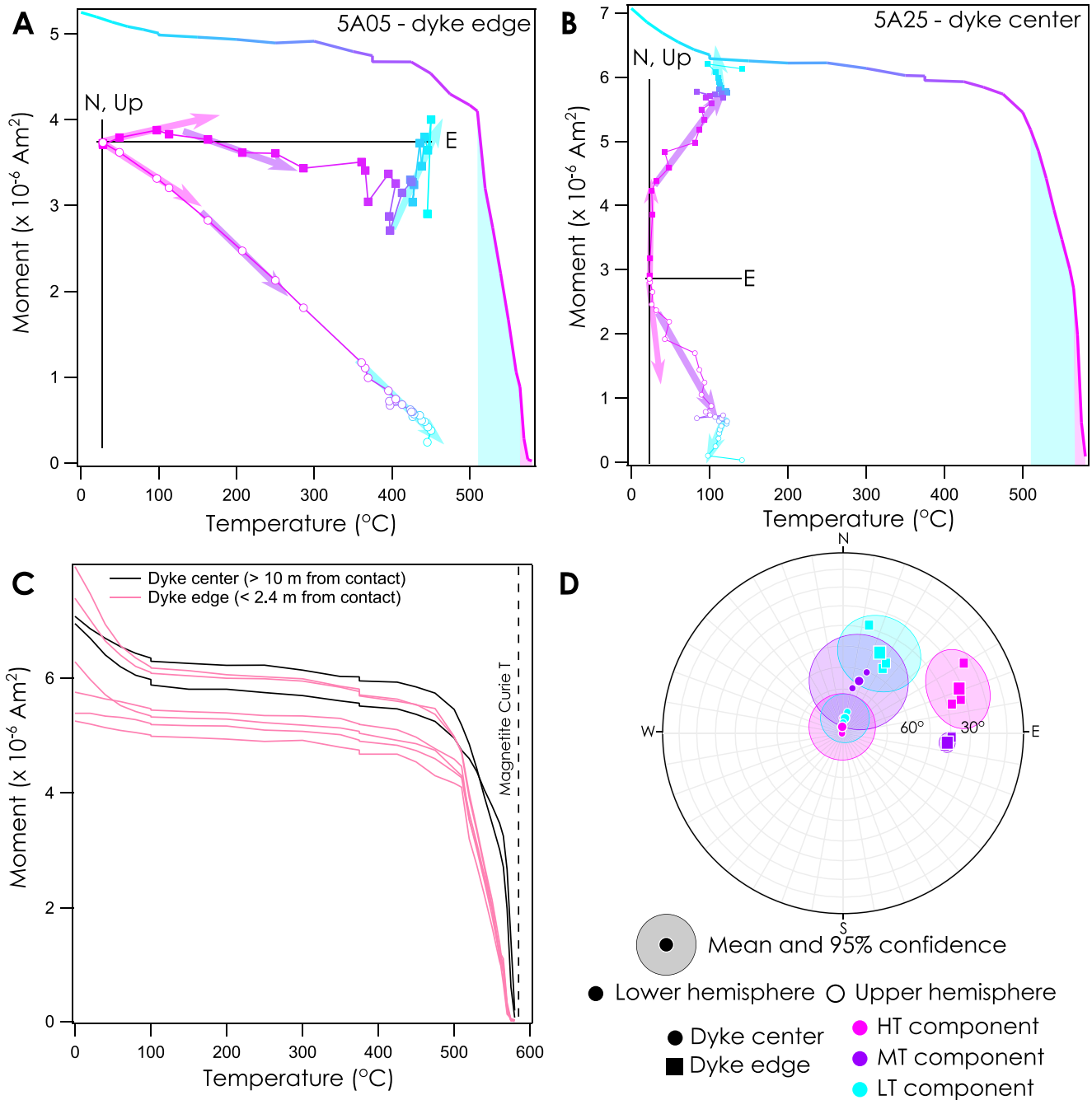


Figure 5. The demagnetization behavior of the edge and center of the large N-S trending norite dyke shown in Figure 1. (a) An example of the demagnetization behavior exhibited by three specimens collected <2.4 m from the edge of the dyke. Inset shows orthographic projections of endpoints of NRM demagnetization on north-east (N-E) and up-east (U-E) directions (Zijderveld diagram). (b) An example of the demagnetization behavior exhibited by two specimens collected >10 m from the edge of the dyke. Inset shows orthographic projections of endpoints of NRM demagnetization on north-east (N-E) and up-east (U-E) directions (Zijderveld diagram). (c) The difference in unblocking temperature between the edge and center of the dyke. The specimens collected closer to the edge of the dyke unblock at slightly lower temperatures than those collected from the center. (d) An equal area stereographic projection showing the recovered directions from the dyke edge and the dyke center. Shallower, eastward trending directions are recovered from the dyke edge, while the dyke center exhibits steeper, northward trending components that may suggest a viscous remanence overprint from the present-day field.

3.4. Pseudo-Baked Contact Tests

As discussed below, we found that the magnetization carried by the Ameralik dykes is inherently unstable. We were therefore unable to carry out traditional baked contact tests, and assume that the magnetization in the

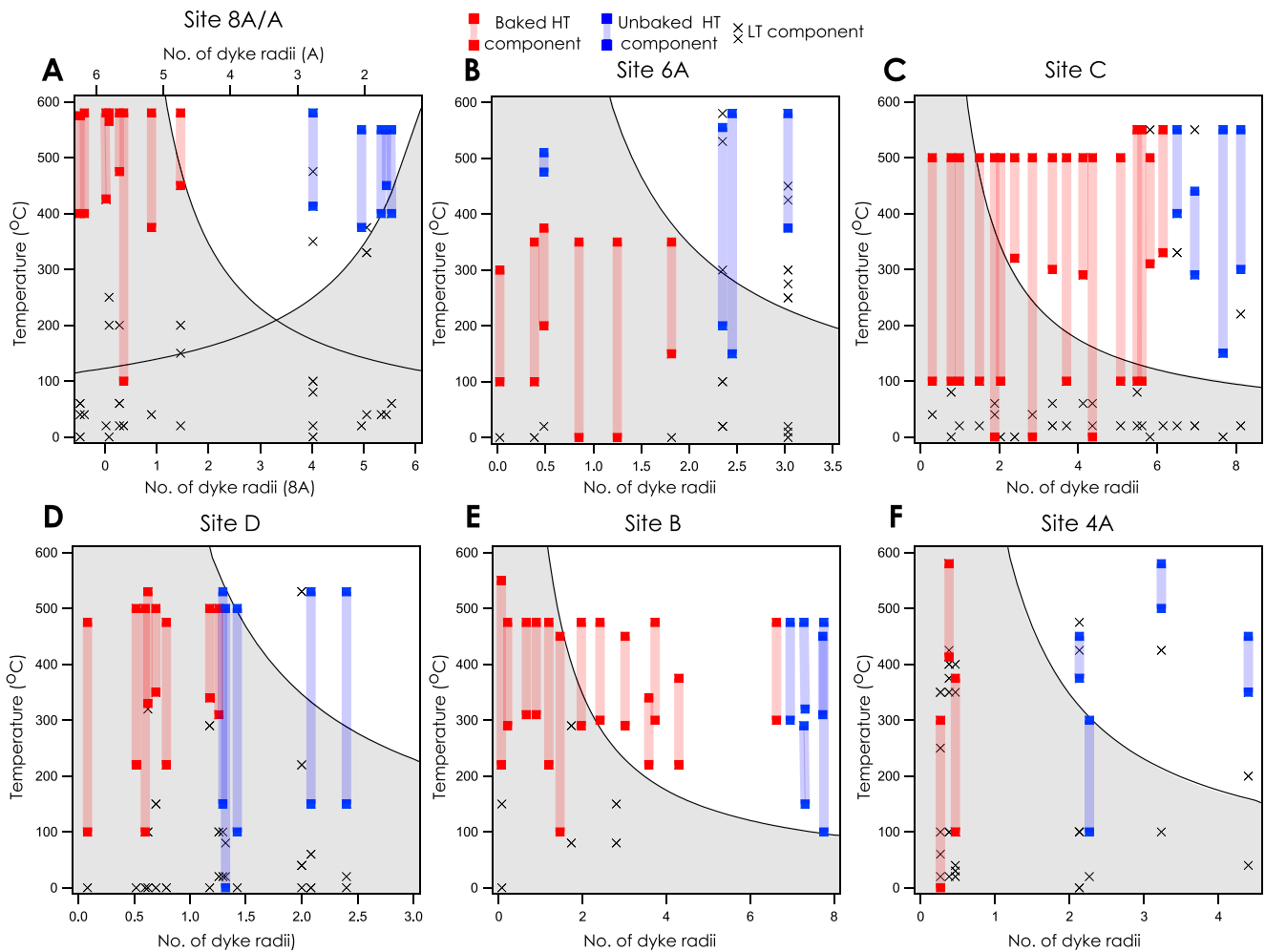


Figure 6. Thermal profiles calculated using the model reported by Jaeger (1964) show a simple estimate of the temperature to which the country rock has been thermally perturbed (gray region) as a function of dyke radius. We show for sites 8A/A, 6A, 4A, C and B that the unbaked components lie predominantly outside of the thermally perturbed region, and minor overlaps can be explained by accounting for factors such as thermal convection and dyke emplacement below the liquidus temperature which are not taken into account by the model used here. At Site D, the unbaked directions extend well into the thermally perturbed zone and we therefore disregard this site in further analysis.

Ameralik dykes post-dates their emplacement and was acquired during greenschist-grade metamorphism during the Neoproterozoic tectonothermal event (Table 1). We therefore carried out pseudo-baked contact tests, where only paleomagnetic directions recovered from the country rock surrounding the dykes (in this case carried by the BIF) are considered. We compare the NRM components close to the dyke that were thermally perturbed by the intrusion to the NRM components in the BIF sufficiently far from the intrusion to be thermally unaffected. The direction carried by the Ameralik dyke itself is not considered. We carried out pseudo-baked contact tests at six sites in the northernmost part of the eastern ISB (Figure 1).

We targeted areas where Ameralik dykes had intruded through the BIF, and therefore represent a distinct, localized thermal perturbation that should only have influenced the BIF immediately adjacent to the dykes. We found that in all cases, the dyke NRM component directions were poorly defined and scattered, with low peak blocking temperatures (<350°C) at each site and between sites (Figure S9 in Supporting Information S1) suggesting variable CRM acquisition during Neoproterozoic metamorphism (Komiya et al., 2004).

We infer the boundary between BIF that was baked and BIF that remained largely unbaked by the dyke intrusion by using a simple thermal diffusion model for a basaltic dyke intruding into silicate country rock (Jaeger, 1964), and by considering the distance at which HT components of the NRM begin to converge on a single direction (Figure 6). The radii of the dykes at Sites 4A, 6A, 8A, A, B, C and D were 3, 3, 5, 6.5, 3.35, 3.35 and 8.5 m, respectively.

The width of the baked region is influenced by a number of factors and the diffusion model shown in Figure 6 gives only an approximate estimate on the width of the baked region at each site. We assume all dykes were emplaced at the same temperature (1200°C) since they all have a doleritic composition (White et al., 2000; Nutman & Friend, 2009; Komiya et al., 2004). We assume that the dykes are emplaced at their liquidus temperature (i.e., they are carrying no crystalline cargo), which is likely an upper limit on the initial temperature. We assume the surrounding country rock is dry, and there is no heat transport away from the intrusion via convection, which would act to reduce the size of the baked region (Annen, 2017; Nabelek et al., 2012). The reported widths of the dykes are upper limits, since tilting will make the apparent width of the intrusions greater than their emplacement width. The shape of the temperature versus distance curves (Figure 6) assumes no thermal convection within the intrusion or rejuvenation of melt supply after initial dyke emplacement.

3.4.1. The Paleomagnetism of the Ameralik Dykes

The Ameralik dykes are highly variable in terms of their paleomagnetic stability and the recovered paleodirections. The dykes at sites 8A/A and 6A show the most stable behavior, with a HT component demagnetized by ~350°C. We suggest this may be because growth of magnetite during metamorphism essentially imparted a partial TRM (pTRM) up to 350°C, although the mechanism of remanence acquisition is currently not well enough constrained to confirm this. The dykes no longer contain any of their primary igneous mineralogy, and the magnetite present is formed during the replacement of olivine (Komiya et al., 2004). It has been noted that the magnetite content varies widely among the dykes most likely reflecting different degrees of equilibration during metamorphism, as well as varying abundances of initial olivine. The inconsistency in paleomagnetic stability between Ameralik dykes can be explained by acquisition of a relatively low temperature (350°C) CRM, as well as variations in the abundance, size and shape of magnetite present.

At site 6A, four specimens of the Ameralik dyke were demagnetized up to 580°C. The NRM of the dyke samples (6A01, 6A02 and 6A03) are demagnetized by 350°C, and define a single direction of 29°/321° ($\alpha_{95} = 13^\circ$). The fourth dyke sample (6A04), which comes from near the edge of the intrusion, was entirely demagnetized at <100°C.

At site 4A, eight Ameralik dyke specimens (including four sister specimens) were demagnetized up to 580°C. The majority of magnetization was removed from the Ameralik dyke specimens by 350°C, and specimens generally show unstable magnetization behavior (e.g., a consistent component cannot be recovered even from sister specimens). Four specimens (4A01-2, 4A02-1, 4A02-2 and 4A04-2) showed a stable component between 100 and 350°C which defined a direction -73°/204° ($\alpha_{95} = 25^\circ$).

At site 8A/A two Ameralik dykes, A and 8A, intrude close to one another (37.5 m apart) through a well exposed section of BIF. The two dykes define distinct directions and have contrasting magnetic properties. Eight specimens (including four sister specimens) of dyke A define a direction of -25°/253° ($\alpha_{95} = 4^\circ$). The magnetization is very stable until ~330°C and the majority (>90%) of magnetization is removed between 325 and 375°C. Six specimens of dyke 8A were demagnetized, five of which had resolvable components and two of which had stable components at temperature exceeding 300°C. The two specimens with stable HT components (8A01 and 8A03B) show broadly similar behavior to dyke A, although the behavior is generally less stable with considerably higher MADs (~20° for the HT components of dyke 8A, compared to 5° for all specimens of dyke A). The two HT components from dyke 8A define the direction -53°/120° ($\alpha_{95} = 39^\circ$).

Sites B, C and D all sample the same Ameralik dyke (Figure S11 in Supporting Information S1). At site B, twelve Ameralik dyke specimens were measured. Nine of the dyke specimens were thermally demagnetized and three were AF demagnetized. The dyke specimens exhibited unstable demagnetization behavior often with a MAD >20°. The majority of magnetization was removed below 300°C for thermally demagnetized specimens, and below 60 mT for AF demagnetized specimens. LT (<150°C) components were highly scattered. However, seven specimens exhibited a stable component up to a maximum temperature of 220–425°C which define a consistent direction of 69°/045° ($\alpha_{95} = 18^\circ$). This component is consistent with the direction 66°/340° ($\alpha_{95} = 32^\circ$) recovered from the three AF demagnetized specimens. At site C, eight dyke specimens (including four sister specimens) were thermally demagnetized. Six of the dyke specimens exhibited highly unstable thermal demagnetizations and no stable components of magnetization could be resolved. Two sister specimens (C24a and C24b) exhibited stable demagnetization up to 550°C (MAD <10°). At site D, six dyke specimens (including two sister specimens) were thermally demagnetized. HT (>300°C) components were recovered from three of the dyke specimens defining

the direction $42^{\circ}/246^{\circ}$ ($\alpha_{95} = 51^{\circ}$). A distinct LT direction ($<300^{\circ}\text{C}$) was also recovered for all four specimens (including averages of sister specimens) defining the direction $53^{\circ}/135^{\circ}$ ($\alpha_{95} = 28^{\circ}$).

3.4.2. Changes in BIF Paleomagnetic Directions With Distance From Ameralik Dyke Intrusions

For each pseudo-baked contact test, Watson's V_W statistic was calculated (G. S. Watson, 1983); this statistic determines whether the mean HT baked and unbaked directions are statistically distinct, representing a passed pseudo-baked contact test, or indistinguishable (i.e., they share a common mean) representing a failed test.

At site 8A/A, fifteen BIF specimens were measured (including one sister specimen; Table 3; Table S5). BIF specimens <7.3 m from the contact with dyke 8A (>30 m from dyke A) exhibited LT ($\leq 200^{\circ}\text{C}$), MT ($\leq 450^{\circ}\text{C}$) and HT ($>500^{\circ}\text{C}$) components with generally stable demagnetization behavior (MAD $<10^{\circ}$). A significant portion of the magnetization is lost by 100°C , with the remaining portion lost by 400°C (Figure 7). Seven baked BIF specimens had a HT component that defined the direction $-24^{\circ}/187^{\circ}$ ($\alpha_{95} = 59^{\circ}$). Unbaked BIF specimens >20 m from dyke 8A and >10 m from dyke A generally exhibited stable MT ($\leq 450^{\circ}\text{C}$) and HT ($>500^{\circ}\text{C}$) components. The HT component defines a direction of $62^{\circ}/025^{\circ}$ ($\alpha_{95} = 47^{\circ}$). The calculated Watson V_W statistic for the unbaked and baked BIF directions exceeds the critical V_W value, indicating a passed pseudo-baked contact test with 95% confidence (Figure 8A).

At site 6A (Figure 9; Table S6), the baked (<5.45 m from the contact) BIF specimens contained an MT component which is demagnetized $<400^{\circ}\text{C}$. Five baked specimens defined a coherent direction of $56^{\circ}/249^{\circ}$ ($\alpha_{95} = 28^{\circ}$). One BIF specimen, 6A10, collected 1.45 m from the dyke had a HT component ($T > 475^{\circ}\text{C}$, Table 3) that was consistent with the direction recovered from three unbaked BIF specimens (6A15, 6A16 and 6A17) collected >5.45 m from the dyke contact, suggesting its original HT magnetization was not overprinted during dyke emplacement. The four specimens demagnetize up to $>500^{\circ}\text{C}$ and define the direction of $46^{\circ}/048^{\circ}$ ($\alpha_{95} = 25^{\circ}$). Watson's V_W value for the unbaked and baked directions exceeds the critical value of V_W , indicating a passed pseudo-baked contact test with 95% confidence (Figure 8b).

At site C, twenty one BIF specimens were both thermally and AF demagnetized (Figure 10; Table S7). Baked BIF specimens taken <20 m from the dyke contact defined a consistent HT (stable up to 500°C) direction of $71^{\circ}/174^{\circ}$ ($\alpha_{95} = 21^{\circ}$). Eleven sister specimens of BIF were also AF demagnetized. Seven of these specimens lie within 20 m of the dyke contact and define a HC direction of $70^{\circ}/208^{\circ}$ ($\alpha_{95} = 26^{\circ}$). When combined, the HC and HT direction is $79^{\circ}/169^{\circ}$ ($\alpha_{95} = 22^{\circ}$). Further than 20 m from the dyke, a distinct direction emerges for both thermally and AF demagnetized BIF samples with a direction of $30^{\circ}/313^{\circ}$ ($\alpha_{95} = 26^{\circ}$) and $53^{\circ}/276^{\circ}$ ($\alpha_{95} = 35^{\circ}$), respectively. When combined, these give a HC and HT direction of $25^{\circ}/294^{\circ}$ ($\alpha_{95} = 18^{\circ}$). Watson's V_W statistic for the combined HC and HT directions exceeds the critical value of V_W , indicating a passed pseudo-baked contact test with 95% confidence (Figure 8c).

At site D, seventeen BIF specimens (including 3 sister specimens) were thermally demagnetized (Figure S12 in Supporting Information S1; Table 4; Table S8). BIF specimens taken <11 m from the dyke contact defined scattered directions at low temperatures ($<290^{\circ}\text{C}$), and define a HT ($>310^{\circ}\text{C}$) direction of $17^{\circ}/229^{\circ}$ ($\alpha_{95} = 79^{\circ}$). BIF samples taken from ≥ 11 m from the dyke contact define a HT ($\geq 500^{\circ}\text{C}$) component defining the direction $48^{\circ}/303^{\circ}$ ($\alpha_{95} = 43^{\circ}$). Using Watson's V_W statistic, we found that the two directions are statistically distinct at the 95% confidence interval (Figure 8d). However, site D is not included in further analysis, since the uncertainty in the recovered directions is large and overlaps, and thermal diffusion modeling suggests sampling did not extend far enough from the intrusion (Figure 6d).

At site B, twenty-one BIF specimens were thermally demagnetized (Figure S13 in Supporting Information S1; Table 4; Table S9). BIF specimens experienced alteration during heating to temperatures exceeding 475°C and it is therefore unclear how far above this temperature these stable components extend. Specimens which exhibited a MAD $<10^{\circ}$ and a stable component up to 475°C were assessed for the pseudo-baked contact test. At a distance of >23 m from the dyke contact, six unbaked BIF specimens define a consistent direction of $302^{\circ}/69^{\circ}$ ($\alpha_{95} = 44^{\circ}$). Baked BIF specimens <23 m from the dyke contact define two broadly antipodal directions. Of the sixteen specimens in this region, seven have a negative inclination and define the direction $186^{\circ}/-43^{\circ}$ ($\alpha_{95} = 23^{\circ}$). The recovered directions for the baked and unbaked BIF are indistinguishable to 95% confidence using Watson's V_W statistic (Figure 8e).

Table 3

A Summary of the Directions Used in the Passed Pseudo-Baked Contact Tests at Sites 8A/A, 6A, and C

Sample	Distance from dyke 1 (m)	Distance from dyke 2 (m)	AF/thermal?	Range (mT or °C)	Dec (°)	Inc (°)	Origin trending?	MAD (°)	dAng (°)
Site 6A baked									
6A05	0.07		Thermal	100–300	188	82	×	1	1
6A09	1.15		Thermal	100–350	262	39	×	17	22
6A10	1.45		Thermal	200–375	329	63	×	11	15
6A11	2.55		Thermal	0–350	282	42	✓	14	5
6A12	3.75		Thermal	0–350	204	68	✓	5	1
6A13	5.45		Thermal	150–350	263	5	✓	21	19
Site 6A unbaked									
6A15	7.05		Thermal	200–555	67	36	✓	13	12
6A16	7.35		Thermal	150–580	42	27	✓	8	7
6A17	9.1		Thermal	375–580	18	65	✓	25	23
6A10	1.45		Thermal	475–510	52	51	✓	19	17
Site 8A/A baked									
8A05	−2.4	39.9	Thermal	400–575	211	−19	✓	9	2
8A06	−2.0	39.5	Thermal	400–580	194	68	✓	11	1
8A09	0.1	37.4	Thermal	426–580	173	28	✓	7	2
8A10	0.4	37.1	Thermal	565–580	236	−28	×	14	37
8A12	1.4	36.1	Thermal	475–580	169	−66	✓	7	5
8A13	1.8	35.7	Thermal	100–580	220	3	✓	11	4
8A15	4.5	33.0	Thermal	375–580	166	42	✓	4	1
8A17	7.3	30.2	Thermal	450–580	194	−70	✓	5	4
Site 8A/A unbaked									
8A19	20.1	17.4	Thermal	413–580	350	45	✓	9	2
A05	24.8	13.3	Thermal	375–550	354	66	✓	14	5
A07	26.7	11.4	Thermal	400–550	58	22	✓	14	10
A08	27.2	10.9	Thermal	450–550	331	49	✓	19	0
A09	27.7	10.4	Thermal	400–550	138	44	✓	16	1
Site C baked									
C23a	1		Thermal	100–500	183	−86	✓	17	2
C22b	2.6		Thermal	100–500	185	69	✓	4	1
C21a	3.3		Thermal	100–500	173	80	✓	11	4
C20a	5		Thermal	100–500	89	39	✓	15	10
C19a	6.3		Thermal	0–500	195	−67	✓	17	2
C18b	6.8		Thermal	100–500	196	29	✓	9	1
C18a	6.8		AF	25–145	182	84	✓	3	3
C17b	8		Thermal	320–500	194	48	✓	11	6
C17a	8		AF	25–145	225	20	×	9	24
C16a	9.5		Thermal	0–500	219	51	✓	4	3
C15a	11.2		Thermal	300–500	327	50	×	8	13
C14b	12.4		Thermal	100–500	189	79	✓	6	2
C13a	13.8		Thermal	290–500	149	28	✓	15	9
C12a	14.6		Thermal	0–500	356	82	×	7	10

Table 3
Continued

Sample	Distance from dyke 1 (m)	Distance from dyke 2 (m)	AF/thermal?	Range (mT or °C)	Dec (°)	Inc (°)	Origin trending?	MAD (°)	dAng (°)
C12b	14.6		AF	30–145	289	48	✓	25	4
C11a	17		Thermal	100–500	161	38	✓	8	4
C11b	17		AF	55–145	205	61	×	12	15
C10a	18.4		Thermal	100–550	38	32	✓	10	4
C09a	18.8		Thermal	100–550	194	76	✓	5	3
C08a	19.5		Thermal	310–500	215	46	✓	20	14
C08b	19.5		AF	10–145	174	84	×	2	4
C06a	20.6		Thermal	330–550	310	25	✓	7	2
Site C unbaked									
C05a	21.8		Thermal	400–550	317	29	✓	23	11
C05b	21.8		AF	10–145	255	2	×	2	5
C04a	23.3		Thermal	290–440	334	38	✓	5	3
C04b	23.3		AF	10–145	318	40	×	2	3
C02a	25.7		Thermal	150–550	328	7	×	3	3
C02b	25.7		AF	10–145	262	19	×	1	5
C01a	27.2		Thermal	300–550	265	43	✓	4	3
C01b	27.2		AF	10–145	281	25	×	13	19

At Site 4A, eleven BIF specimens (including four sister specimens) were demagnetized up to 580°C (Figure S14 in Supporting Information S1; Table 4; Table S10). The BIF specimens showed stable demagnetization, although the recovered directions are highly scattered, even when compared to sister specimens. 4A12 and 4A13, which were collected furthest from the contact at 9.7 and 13.2 m respectively, had MT and HT components which defined the direction 179°/–49° ($\alpha_{95} = 34^\circ$) suggesting that the BIF has been entirely overprinted, or is unable to retain a stable magnetization direction. This result is consistent with the large drop in magnetization during a preliminary liquid nitrogen step, suggesting that the vast majority of magnetite in the specimens is multidomain. The BIF specimens defined a coherent LT direction up to temperatures of 350°C with direction 235°/46° ($\alpha_{95} = 28^\circ$) consistent with an overprint acquired during Neoproterozoic metamorphism. The LT and HT components in the BIFs overlap with the HT component in the dyke, again suggesting a pervasive overprint on this field site. We could not rule out that the mean directions for the baked and unbaked BIF share a common mean. They are indistinguishable to 95% confidence using Watson's V_w statistic (Figure 8f).

3.5. Fold Test

We carried out a fold test on unbaked and baked BIF from the three sites that passed the pseudo-baked contact test: 6A, 8A/A, and C. The structure of a large-scale (several hundred meters) fold was recovered from bedding measurements of the BIF (parallel to the banding in the BIF) in the northernmost part of the area. The fold has a near-vertical axial-plane (calculated as the plane that bisects the fold and intersects the fold axis) with a strike, dip and dip direction of 175°/85°W and the fold axis has a plunge and trend of 54°/181°. Initially, the fold was tilt-corrected to remove the plunge of the fold axis (Figure S15 in Supporting Information S1). Then, each set of baked and unbaked paleomagnetic directions were untilted based on the bedding measurement for each site (Figure 11; Figure S15 in Supporting Information S1). Average bedding measurements for each site were 108°/60° SSW (site C), 145°/67° SW (site 8A/A) and 346°/83° E (site 6A). Each set of measurements were tilted progressively from –10% to 110% tilt correction by changing the dip of the correction and holding the strike constant. For each degree of tilting the primary eigenvalue, τ_1 , was calculated. The larger the value of τ_1 the greater the degree of clustering of directions, regardless of their polarity (Tauxe & Watson, 1994).

For the baked directions, the maximum value of τ_1 was recovered between below 70% untilting (Figure 11). This result suggests that the directions in the baked BIF were acquired post-tilting due to the juxtaposition of the 3.7 Ga

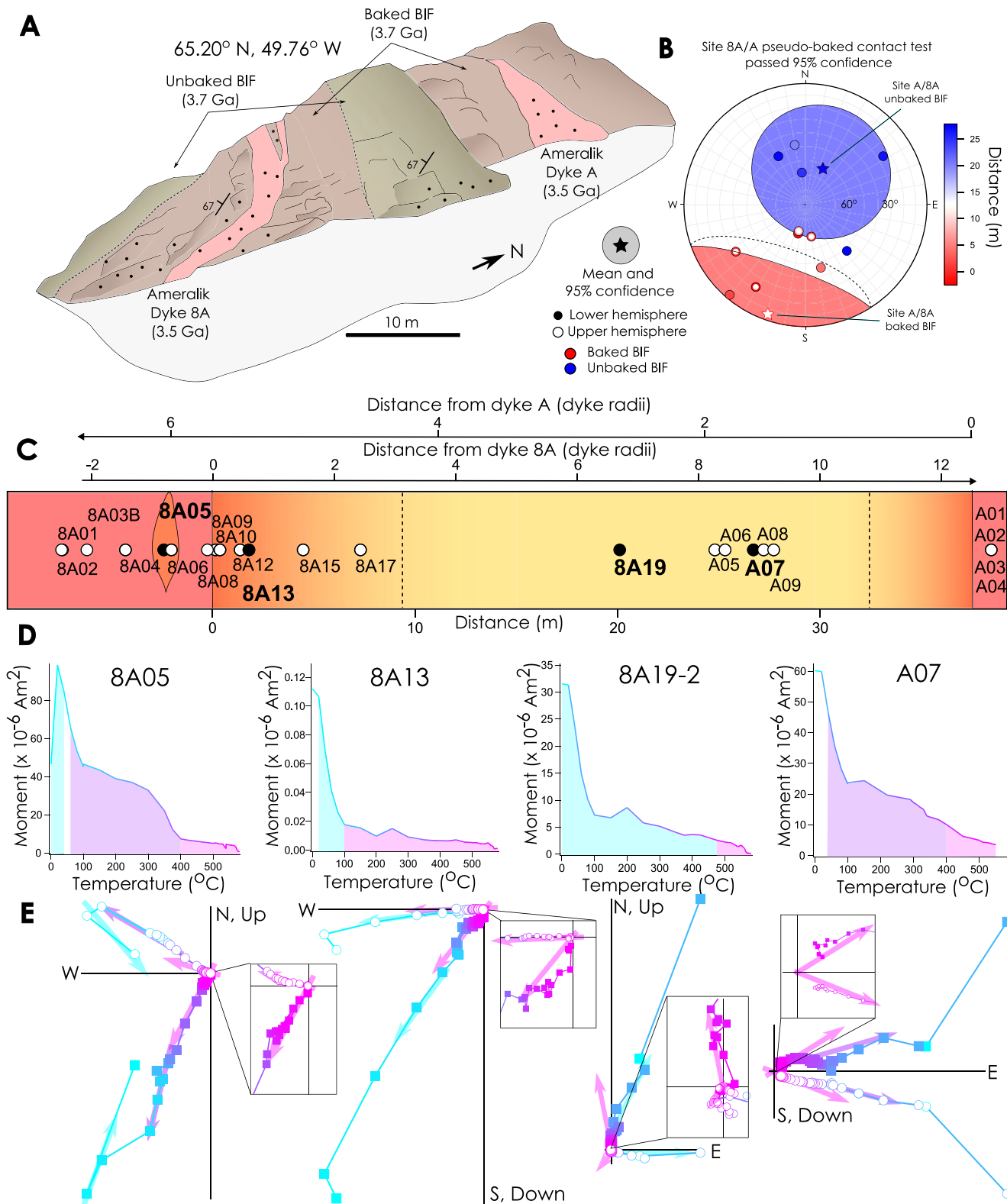


Figure 7.

northern terrane and 3.8 Ga southern terrane at 3.69 Ga (Nutman & Friend, 2009), most likely during the emplacement of the Ameralik dyke swarm 3.26–3.5 Ga (Nutman et al., 2004). It is unknown whether the original magnetization in the dykes was uniform in orientation, but at 20% tilting a magnetization direction pointing toward the south is recovered from the baked BIF (Figure 11).

For the unbaked BIF directions, the maximum value of τ_1 was recovered between 80% and 110% untilting, suggesting a passed fold test (Figure 11). This result indicates that the magnetization in the unbaked BIF was acquired pre- or syn-tilting during Eoarchean metamorphism and the juxtaposition of terranes at 3.69 Ga (Nutman & Friend, 2009). After untilting, the unbaked paleodirections converge onto a single direction.

3.6. Pseudo-Thellier Paleointensity Estimates

Three specimens (A05c, A07c and C02b) from sites 8A/A and C that passed the pseudo-baked contact test and fold test were used for Pseudo-Thellier experiments (Paterson et al. (2016); Figure 12). These specimens were also chosen because they are close to the locality where the magnetite in the BIF was U-Pb dated (Frei et al., 1999; Frei & Polat, 2007). Specimens were AF demagnetized up to 145 mT to first remove the NRM. A 50 μ T ARM was applied, and again the specimens were demagnetized up to 145 mT. Finally, the samples were given a 40 mT IRM, which was also demagnetized up to 145 mT. The ARM and IRM acquisitions were used to determine the fidelity of the samples, and they were found to be able to reliably recover an ARM paleointensity of 50 μ T (Figure S16 in Supporting Information S1, Table S11).

AF demagnetization of the NRM revealed a HC component that was origin-trending and stable to >130 mT. Paleointensity estimates were acquired by comparing the vector-subtracted NRM demagnetization to the ARM demagnetization. Three distinctive slopes were observed for specimens A05c and A07c and four for C02b. A paleointensity was calculated for each linear part of the curve between the change in slope. The recovered values vary substantially for the LC and MC components (Table S12). The HC components, which were also origin-trending components for the NRM (Figure 12) return similar paleointensity estimates of $17 \pm 1.2 \mu$ T, $15 \pm 0.4 \mu$ T, and $15 \pm 0.6 \mu$ T, respectively (uncertainties are two standard deviations). A mean paleointensity estimate of $15.1 \pm 1.2 \mu$ T (uncertainty is two standard deviations), assuming the NRM represents a TRM, was recovered by combining results for the three specimens (Figure 13). One specimen was also corrected for remanence anisotropy (Selkin et al., 2000) which slightly increased the recovered paleointensity to $16.7 \pm 0.7 \mu$ T. Since the magnetite in our samples acquired a CRM, these results are taken as evidence for the presence of a field, but should not be considered an accurate representation of its strength. CRM acquisition is usually less efficient than TRM acquisition (Stokking & Tauxe, 1987, 1990), but calibrating between the two remains challenging.

4. Discussion

4.1. The Age of Dykes and Implications for Passed Pseudo-Baked Contact Tests

We have assumed that the dykes sampled in this study are part of the Ameralik dyke swarm, following the interpretation of Nutman and Friend (2009). However, three sets of Archean dykes are discussed in the literature for this region; the Ameralik, Tarssartôq and Inaluk dykes. The Tarssartôq dykes are thought to be part of the Ameralik dyke swarm (Nutman et al., 2004), with both having basaltic compositions and common inclusion of plagioclase megacrysts. The different nomenclature for these two suites of dykes was adopted to account for the differing extent of deformation, with the Tarssartôq dykes being better preserved (Nutman, 1986). However, a genetic link between the two has never been firmly established (White et al., 2000). The Tarssartôq dykes have a U-Pb baddelyite age of $3,490 \pm 2$ Ma (Crowley et al., 2000).

Figure 7. Passed pseudo-baked contact tests for site 8A/A. (a) A field sketch of the outcrop from which samples were taken at site 8A/A. (b) An equal area, lower hemisphere stereographic projection showing high temperature (HT) and high coercivity (HC) components for the BIF at site 8A/A. Samples collected further from both dykes show a distinct direction compared to those collected closer to the dykes, indicating a positive pseudo-baked contact test. (c) A schematic diagram showing the distance of each sample from the Ameralik dykes. The samples in the yellow region are not thermally perturbed by either dyke. (d) Thermal demagnetization curves and (e) zijderveld diagrams are shown for a range of distances from the intrusion-BIF contact to show how the recovered directions change with extent of thermal perturbation imparted by the dykes.

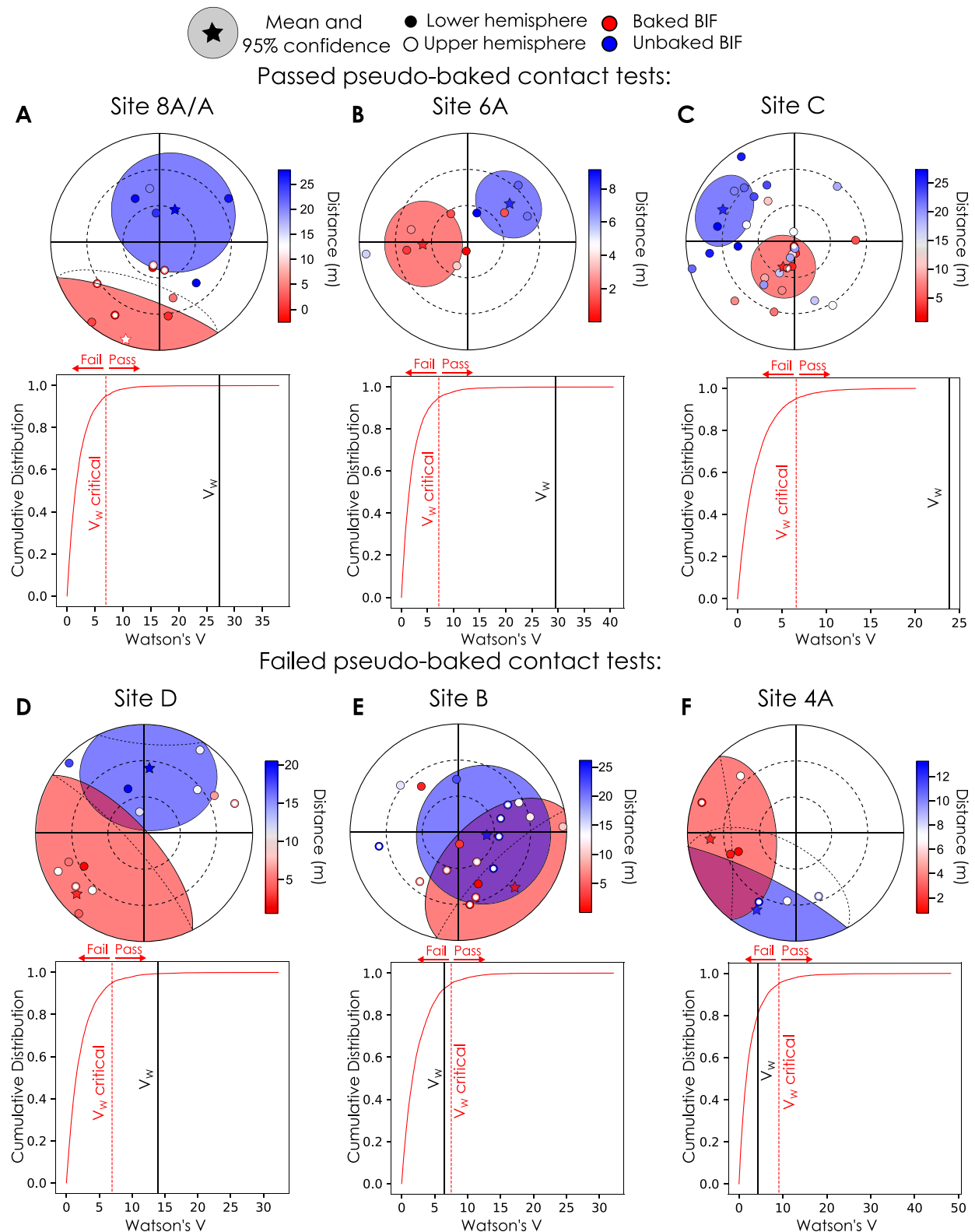


Figure 8. Bootstrapping tests to determine whether baked and unbaked BIF directions are distinct to 95% confidence by calculating Watson's V_w statistic. If $V_w > V_{w\text{critical}}$ the pseudo-baked contact test is considered to pass. We show passed tests for (a), (b), and (c), which show data for sites 8A/A, 6A and C, respectively. (d) At Site D the pseudo-baked contact test technically passes, although we do not include it in further analyses because of the high degree of scatter in the directions and the fact sampling did not extend sufficiently far from the baked zone (Figure 6D). (e) and (f) show data for sites B and 4A which fail the test.

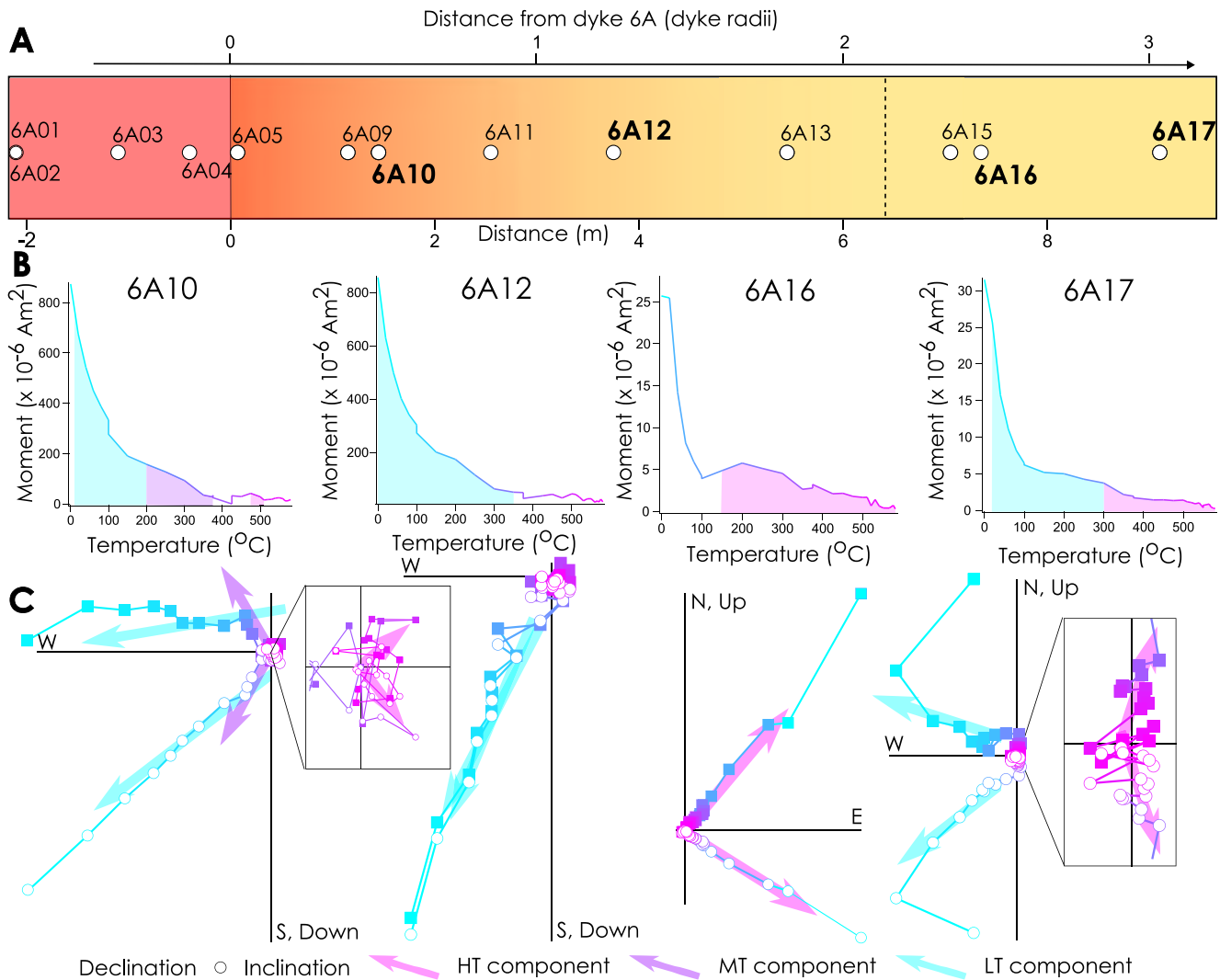


Figure 9. Passed pseudo-baked contact tests for site 6A. (a) A schematic diagram showing the distance of each sample from the Ameralik dyke. Samples that taken >7 m from the dyke are unbaked. (b) Thermal demagnetization curves and (c) zijderveld diagrams are shown for a range of distances from the intrusion-BIF contact to show how the recovered directions change with extent of thermal perturbation by the dyke.

The Inaluk dykes identified in the area are noritic in composition (Nilsson et al., 2010; A. P. Nutman, 1986), up to 4 m in diameter and generally folded (White et al., 2000). They are distinct from the large norite dyke that runs north-south across the area (Figure 1). The small size and sparse occurrence of the Inaluk dykes suggest it is unlikely they were sampled in this study. Nonetheless, they have been dated in previous studies and return ages of $3,512 \pm 6$ Ma, $3,659 \pm 2$ Ma, $3,658 \pm 1$ Ma, and $3,661 \pm 7$ Ma (Nutman et al., 2004; Crowley, 2003; Crowley et al., 2000; Friend & Nutman, 2005). Regardless of which type of dykes we sampled in the area, all of them have an age >3.26 Ga, the younger limit on the emplacement age of the Ameralik dykes. Our passed pseudo-baked contact tests therefore suggest that the magnetization in the unbaked BIF was acquired prior to 3.26 Ga.

4.2. The Tectonic History of the ISB and Implications for the Fold Test

The ISB has undergone several tectonic events resulting in shearing, tilting and folding. The first major event was the development of a juvenile arc between 3,720 and 3,690 Ma ago (Nutman & Friend, 2009; Nutman et al., 2009). The BIF forms part of the central tectonic domain described by Appel et al. (1998) and experienced tight, isoclinal folding prior to its juxtaposition against the rest of the 3.7 Ga northern terrane. The 3.7 Ga northern terrane and 3.8 Ga southern terrane collided 3,690–3,660 Ma, and subsequently both terranes were sheared by a

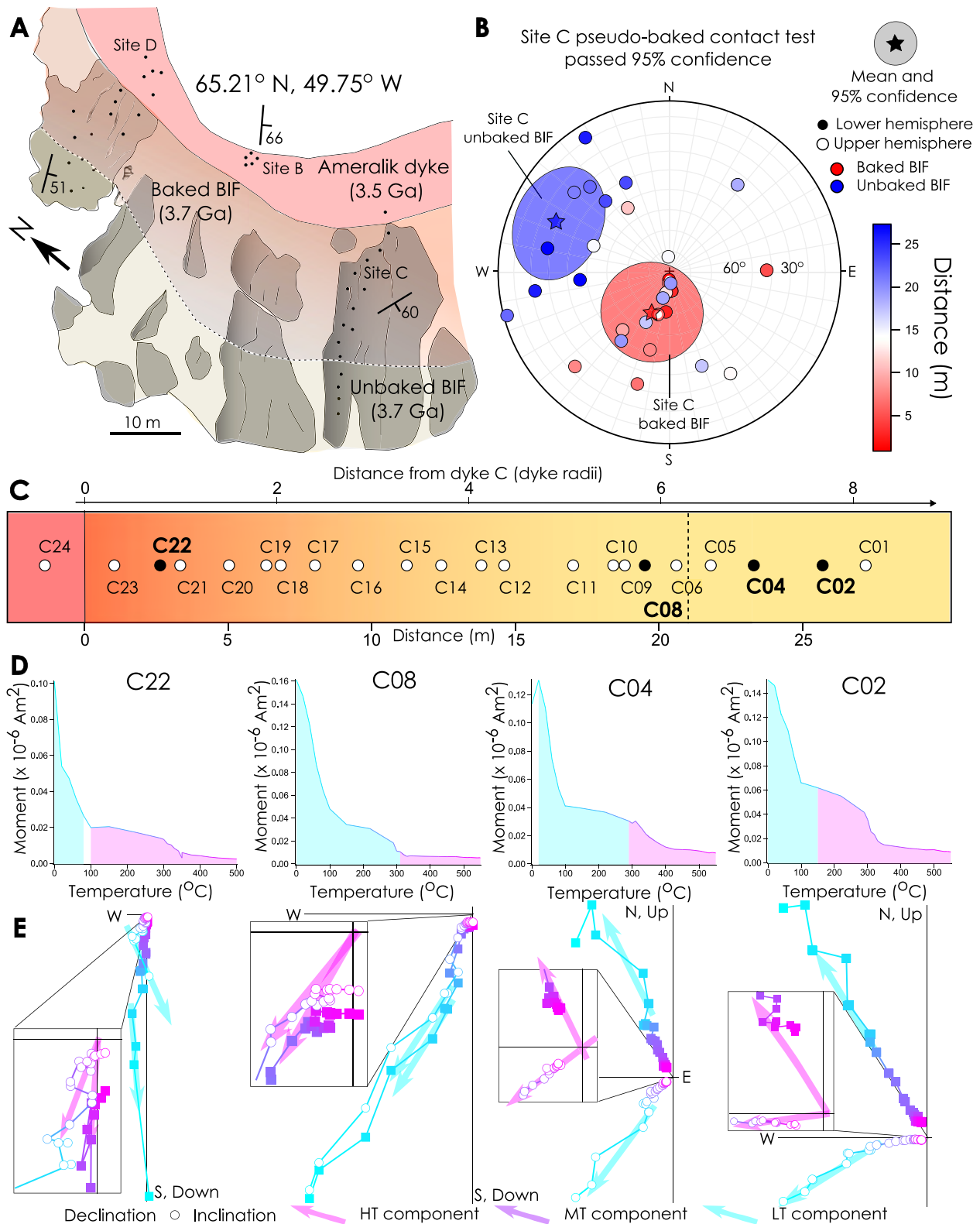


Figure 10.

common event between 3,650 and 3,600 Ma (Nutman & Friend, 2009). Arai et al. (2014) also suggest exhumation and faulting of cold, brittle Eoarchean crust following the juxtaposition of the two terranes, although the exact timing of the event is poorly constrained.

A subsequent Neoproterozoic tectonic event occurred ca. 2.85 Ga ago, where the entire northern Isukasia terrane collided with the southern Kapisilik terrane (Nutman et al., 2015). Large mylonite zones developed >20 km south of the ISB and are associated with metamorphism 2.69 Ga that metamorphosed some of the Ameralik dykes to epidote-amphibolite grade. The influence of this southern shear zone is minimal in the northern part of the ISB, and is unlikely to have resulted in any major structural deformation. Given that the baked BIF fails the fold test while the unbaked BIF passes (Figures 11 and 14), this suggests that folding occurred prior to the emplacement of the dykes >3.26 Ga, most likely during the tectonic and shearing events 3.69–3.60 Ga. This suggests the remanence in the unbaked BIF was acquired before 3.60 Ga.

4.3. Using Paleomagnetic Field Tests and Field Observations to Reinterpret the Tectonothermal History of the Northernmost Part of the ISB

The metamorphic history of the ISB is complex (Figure 1 and Table 1) and part of the difficulty in recovering the tectonothermal history of the area is that the observed metamorphic grades are spatially heterogeneous, and therefore each observation needs to be carefully considered in terms of its geographic location. Understanding the variation in metamorphic grade with geographic location is critical for determining the extent of metamorphic overprints on recovered paleomagnetic data at an outcrop scale. In the existing literature, there are differing interpretations regarding the timing and grade of Eoarchean metamorphism in the northernmost part of the field area, which must be resolved to interpret our paleomagnetic data. Arai et al. (2014) and Komiya et al. (2002) report lower greenschist grade Eoarchean metamorphism in the northernmost part of the area, while other authors (Rollinson, 2003; Nutman et al., 2009; Frei et al., 1999; Dymek, 1988) report amphibolite grade Eoarchean metamorphism in the same area. This discrepancy originates from different interpretations regarding the origin of mafic units in the area. The former authors interpret the northernmost part of the ISB as a series of repeatedly faulted pillow basalts and BIF that are both part of the 3.7 Ga northern terrane. However, Nutman and Friend (2009) interpret the mafic units in this area as Ameralik dykes emplaced 3.26–3.5 Ga, and we agree from our own field observations that the relationship between the mafics and BIF is intrusive. This suggests that the lower greenschist grade metamorphic event interpreted by Arai et al. (2014) and Komiya et al. (2002) must post-date dyke emplacement (i.e., the dykes were metamorphosed by the Neoproterozoic event). All studies (including this one) agree upon the interpretation of the large mafic units in the southern part of the area as pillow basalts, which are well-preserved and still exhibit clear pillow structures with glassy rims. Therefore, we suggest the entire area was metamorphosed to amphibolite grade during the Eoarchean metamorphic event, and subsequently from lower-greenschist grade in the north to upper-amphibolite grade in the south during Neoproterozoic metamorphism.

Our paleomagnetic observations are consistent with a single major amphibolite-grade metamorphic event at 3.69 Ga that resulted in the formation of magnetite, and the corresponding magnetization recovered from the BIFs (Table 5; Figure 14). We found that remanence in the unbaked BIF that passes both the pseudo-baked contact test and the fold test, indicating a magnetization age of ca. 3.7 Ga, was unblocked in the lab at ~550°C, consistent with an amphibolite grade Eoarchean event (Figure 2b). The Ameralik dykes were emplaced after this Eoarchean metamorphic event, and acquired their magnetization during Neoproterozoic metamorphism that resulted in the replacement of their primary igneous mineralogy to a greenschist grade metamorphic assemblage including the growth of magnetite (Table 5; Figure 14). This magnetite acquired a low temperature CRM which was unblocked in the lab at 350°C (Figure S9 in Supporting Information S1). Finally, the norite dyke acquired a thermal remanent magnetization during emplacement at 2.2 Ga and after Neoproterozoic metamorphism. The magnetization in the norite dyke was partially overprinted by the subsequent Proterozoic hydrothermal event. We show that neither the

Figure 10. Passed pseudo-baked contact tests for site C. (a) An aerial sketch showing relief of the outcrops and the location of Sites B, C and D. The large Ameralik dyke that passes through all of these sites is also shown. (b) An equal area, lower hemisphere stereographic projection showing the distinct directions recovered from the baked BIF close to the Ameralik dyke, and the unbaked BIF far from the Ameralik dyke, indicating a passed pseudo-baked contact test. (c) A schematic diagram showing the distance of each sample from the Ameralik dyke. Samples taken >21 m from the dyke were not thermally perturbed by the intrusion. (d) Thermal demagnetization curves and (e) *z*ijderveld diagrams are shown for a range of distances from the intrusion-BIF contact to show how the recovered directions change with extent of thermal perturbation.

Table 4
A Summary of the Directions Used in the Failed Pseudo-Baked Contact Tests at Sites 4A, B, and D

Sample	Distance from dyke (m)	Range (°C)	Dec (°)	Inc (°)	Origin trending?	MAD (°)	dAng (°)
Site 4A baked							
4A05	0.8	0–300	252	40	✓	6	16
4A06	1.15	413–580	288	–8	✓	18	4
4A07	1.4	100–375	252	33	✓	4	3
Site 4A unbaked							
4A10	6.4	375–450	316	–24	✓	8	9
4A11	6.8	100–300	187	33	✓	6	2
4A12	9.7	500–580	160	–34	✓	13	9
4A13	13.2	350–450	208	–25	✓	7	2
Site B baked							
B11	0.2	220–550	159	44	×	8	13
B13	0.7	290–475	171	–29	✓	5	1
B14	2.2	310–475	321	41	✓	7	0
B29	3	310–475	174	80	✓	7	2
B15	4	220–475	165	–34	✓	9	1
B30	4.9	100–450	197	–57	✓	5	3
B16	6.6	290–475	218	–38	×	6	6
B18	8.1	300–475	148	–61	✓	7	1
B33	10.1	290–450	87	3	✓	10	3
B20	12	220–340	78	29	✓	14	13
B21	12.5	300–475	64	34	✓	9	7
B22	14.4	220–375	309	28	✓	5	3
B23	22.2	300–475	358	46	✓	13	4
Site B unbaked							
B24	23.3	300–475	61	–43	✓	20	7
B25	24.4	290–475	96	–56	✓	7	3
B26	24.5	150–320	72	–53	×	20	23
B27	25.9	310–450	260	–23	✓	36	13
B28	26	100–475	136	–48	✓	6	3
Site D baked							
D10	0.7	100–475	241	33	✓	12	2
D09	4.4	220–500	219	4	✓	13	3
D08	5.1	100–500	249	23	✓	10	6
D29	5.3	330–530	232	–18	✓	13	2
D07	5.9	350–500	72	–11	✓	12	7
D06	6.7	220–475	62	24	✓	10	5
D05	10	340–500	246	–12	✓	7	1
D04	10.7	310–500	222	26	✓	17	3
Site D unbaked							
D26	11	150–530	51	33	×	9	10
D03	11.2	0–500	34	7	✓	7	2
D02	12.1	100–500	348	72	✓	20	8

Table 4
Continued

Sample	Distance from dyke (m)	Range (°C)	Dec (°)	Inc (°)	Origin trending?	MAD (°)	dAng (°)
D24	17.7	150–530	313	5	✓	5	2
D23	20.4	150–530	340	51	✓	7	4

Neoproterozoic event could have entirely overprinted the remanence acquired during Eoarchean metamorphism, even if these events lasted for >0.1 Ga (Figure 2b; Pullaiah et al. (1975)).

4.4. The Origin of Scatter in Recovered Paleodirections From the Banded Iron Formation

We find that the recovered paleodirections averaged for each site in the BIF exhibit a high degree of scatter ($\alpha_{95} \geq 25^\circ$). However, for an individual specimen, directions are often well defined (MAD < 10°; Table 3). This is similar to the observed paleosecular variation records recovered from lava flows that acquired a TRM almost instantaneously (hours to days), or from sedimentary sequences where a detrital magnetization is locked in during compaction of a narrow layer of sediment at a specific burial depth (Marco et al., 1998; C. L. Johnson et al., 2008). In these cases, a well-defined direction is recovered from each specimen, but a wide range of directions are recovered from samples with closely-related ages (<10⁴–10⁵ years). If enough samples are measured, this secular variation can be averaged out to recover a well-defined paleodirection ($\alpha_{95} < 1^\circ$). Using the TK03 model for the last 5 Ma of paleosecular variation (Tauxe & Kent, 2004), we show that a small number of specimens ($n < 10$), consistent with the results presented here, will result in high degrees of scatter ($\alpha_{95} > 25^\circ$; Figure S16 in Supporting Information S1).

We suggest CRM acquisition in the BIF may have allowed this secular variation to be captured. The BIF is heterogeneous on a centimeter-to-meter-scale, with secondary magnetite veins and brecciated carbonate layers found pervasively on this scale. It is therefore plausible that the short lengthscale spatial variations in fluid flow and temperature will result in effectively instantaneous CRM acquisition on a centimeter-scale (i.e., in each sample), while CRM acquisition is protracted on a meter-scale (i.e., across each site). Therefore, when considering CRM acquisition across the entire outcrop, it is plausible this could capture secular variation on a scale <10⁴–10⁵ years, due to subtle differences in the time of remanence acquisition during metamorphism.

Directional scatter may also partly be attributed to the remanence anisotropy in the BIFs. Previous studies have demonstrated that the remanence is predominantly parallel to the plane of the magnetite bands (Schmidt & Clark, 1994) and can be approximated as an isotropic plane of susceptibility parallel to the bands (and bedding), with a much lower susceptibility perpendicular to the bands. We carried out preliminary anisotropy of ARM (AARM) measurements on 11 specimens from Site C. We found a strong foliation defined by the principal and intermediate susceptibility axes with a ratio of $\frac{\kappa_1}{\kappa_2} = 2.16 \pm 1.34$, which is found to be on average ~4 times stronger than the susceptibility in the minor susceptibility axis, κ_3 (Jelinek (1981); Table S13). This could explain why, at some sites, the recovered α_{95} is greater than would be expected for secular variation (Figure S16 in Supporting Information S1), since a strong planar anisotropy can act to scatter the recovered directions depending on the orientation of magnetization relative to the banding (Figure S17 in Supporting Information S1).

The possible influence of a strong planar anisotropy on our field tests is also considered. For the pseudo-baked contact tests, we chose sites where the orientation of the banding (and therefore the bedding) was relatively constant. Assuming that the anisotropy is coplanar with the mean bedding orientation at each site, that it is isotropic, and is four times stronger in the plane of the bands compared to perpendicular to the bands (i.e., $\kappa_1 = \kappa_2 = 4 \times \kappa_3$) we re-evaluated the results of our field tests (Figures S18 and S19 in Supporting Information S1). We show that our pseudo-baked contact tests all still pass, although the fold tests become less well-defined with no significant clustering for a narrow range of untilting. Since this is only based on a synthetic anisotropy correction, and we have not considered other anisotropy orientations (e.g., anisotropy coplanar with the fold cleavage) we simply use this to highlight that the fold test is inconclusive without further anisotropy measurements. This introduces a degree of ambiguity when interpreting whether folding pre-dates or post-dates the emplacement of the Ameralik dykes. We therefore cannot rule out that the directions were scattered by folding that occurred during the Neoproterozoic, as discussed in Section 4.2.

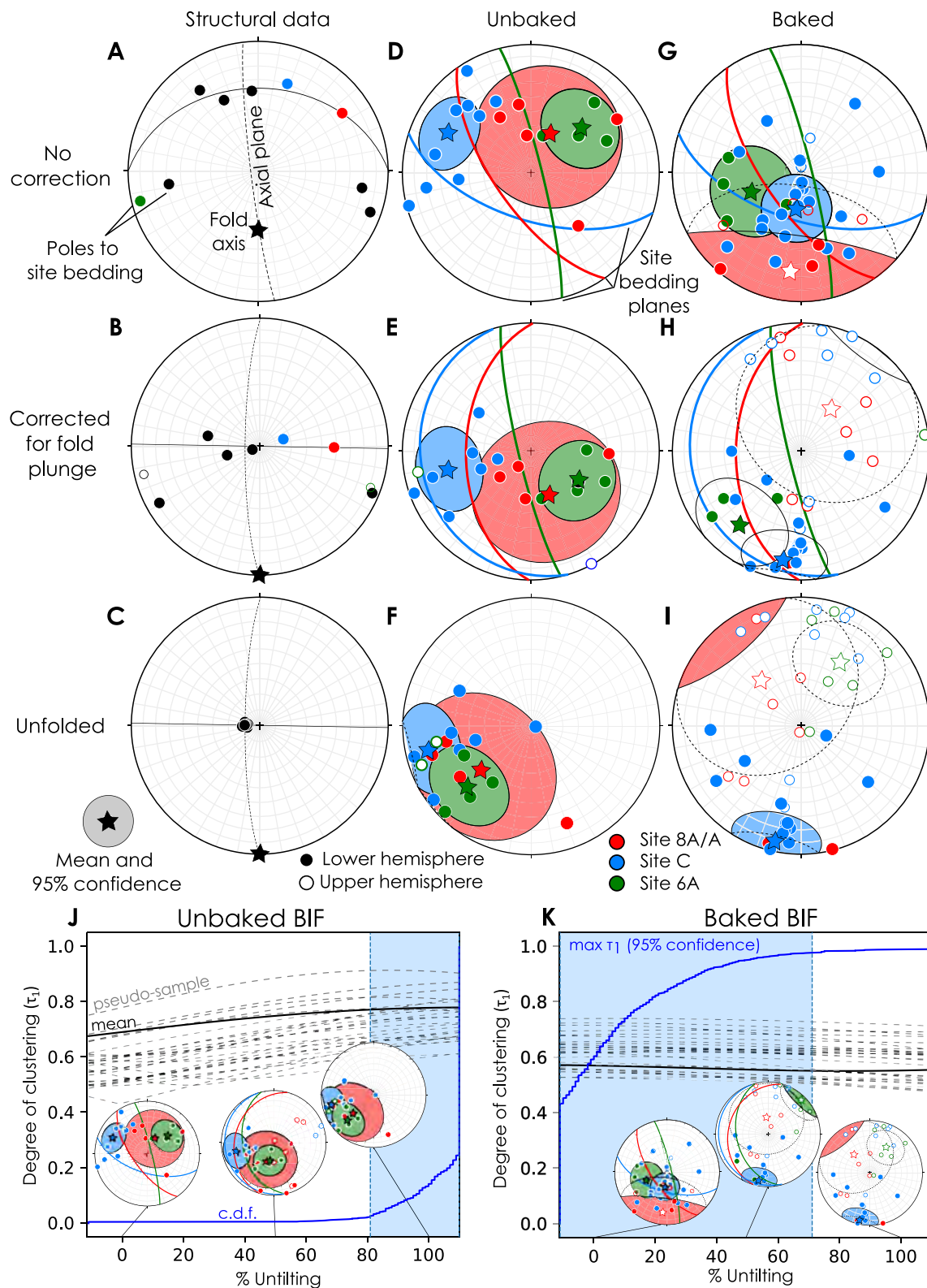


Figure 11.

4.5. Preservation of an Ancient Magnetic Field Record in the ISB and Implications for Atmospheric Escape During the Archean

Our passed pseudo baked contact tests alongside a detailed assessment of the metamorphic and hydrothermal history of the ISB, confirm that a ca. 3.7 Ga old remanence is likely preserved in the unbaked BIF in the northernmost part of the studied region. Our recovered paleointensity ($>15 \mu\text{T}$) is considered a lower limit on the field strength at this time. An exact paleointensity cannot be determined because CRM acquisition is inherently less efficient than TRM acquisition (Stokking & Tauxe, 1987, 1990). In addition, since magnetization was acquired over a relatively long time period during metamorphism, reversals may also have resulted in an underestimate of the average field strength. However, we acknowledge that magnetic anisotropy corrections could act to either increase or decrease the recovered paleointensity. Previous experiments have shown that if the principal anisotropy axis is parallel to the external field, the paleointensity can be over-estimated by 220% or more (Selkin et al., 2000). We anisotropy corrected one of our paleointensity estimates and found that it led to a small increase in field strength, but was still within the uncertainty of our uncorrected measurements. Given the small effect of our anisotropy correction, we argue it is likely that the paleointensity reported here can confidently be interpreted as a lower estimate of the ancient field strength. However, the field could be as weak as $6.8 \mu\text{T}$ if the maximum anisotropy correction were to be applied. This is similar to the 3.5 Ga paleointensity recovered in the Barberton (Herrero-Bervera et al., 2016), although this is also thought to be a lower limit on the true field strength.

Our recovered paleointensity is equivalent to a virtual dipole moment of $1.6 \times 10^{22} \text{Am}^2$, suggesting a solar wind standoff distance of ~ 5 Earth radii, consistent with previous results (Tarduno et al., 2014). This standoff distance is approximately half of that provided by Earth's magnetosphere today, although we acknowledge our results represent a lower estimate. Stronger geomagnetic fields are required to maintain a constant standoff distance during Earth's early history to account for a significantly stronger solar wind during the Hadean and Archean (Vidotto, 2021). Similarly, a stronger geomagnetic field would be required to maintain the size of the polar cap, which directly controls the amount of atmospheric loss via the polar wind (Sternborg et al., 2011). Given present day conditions, Earth's magnetic field would need to be $<10 \mu\text{T}$ atmospheric escape via the polar wind to be substantially enhanced (Gronoff et al., 2020; Gunell et al., 2018). Therefore, given the strong solar wind conditions it is likely our lower limit on the strength of the 3.7 Ga old field would have resulted in increased atmospheric escape via the polar wind compared to the present day. However, when considering the inefficiency of CRM acquisition, the 3.7 Ga old field may have been similar in strength to the present day, enhancing atmospheric escape given the increased intensity of the solar wind. Future models can now incorporate this lower limit on geomagnetic field strength to quantify the maximum escape rate of ionized species, such as hydrogen and xenon, from Earth's early atmosphere and determine whether this escape could have contributed significantly to the Great Oxygenation Event.

5. Conclusions

The ISB contains exceptionally well-preserved crustal rocks from the Eoarchean. In particular, the northernmost part of the northeastern end of the belt has only experienced one high temperature ($470\text{--}550^\circ\text{C}$) metamorphic and metasomatic episode during the Eoarchean (Rollinson, 2002, 2003). During this early metamorphic event, magnetite was formed in the BIFs with a Pb-Pb age of 3.69 Ga (Frei et al., 1999). Between 3.26 and 3.5 Ga the Ameralik dykes were emplaced (Nutman et al., 2004) and thermally reset the BIF immediately adjacent to each intrusion. The dykes were influenced by a subsequent lower greenschist grade metamorphic event in the Neoproterozoic ca. 2.85 Ga (Arai et al., 2014). A third, low temperature hydrothermal event occurred

Figure 11. A fold test of the BIF in the ISB. (a) Structural data for the fold prior to unfolding. (b) Structural data for the fold after rotating the plunge of the fold axis to horizontal. (c) Structural data for the fold after unfolding the limbs. (d–f) are the same as (a–c) for unbaked BIF directions. It can be seen that during unfolding, the directions at the three sites converge, indicating a passed fold test. (g–i) are the same as (a–c) for baked BIF directions. It can be seen that the clustering of these directions diverges during unfolding, indicating a failed baked contact test. (j) The principal eigenvalue, τ_1 , was calculated for all the unbaked BIF directions during various degrees of untilting ranging from -10% – 110% using PMagPy software (Tauxe et al., 2016). Pseudo-samples with the same distribution of directions as the real data are randomly drawn during bootstrapping, and show a systematic increase in clustering with increasing untilting. The maximum degree of clustering is found between 80% and 110% untilting with 95% confidence. (k) As for (j), for baked BIF. The clustering of directions slightly decreases during untilting, with the maximum degree of clustering below 70% untilting. This suggests that the Ameralik dykes were emplaced and thermally remagnetized the baked BIF either prior to, or during folding.

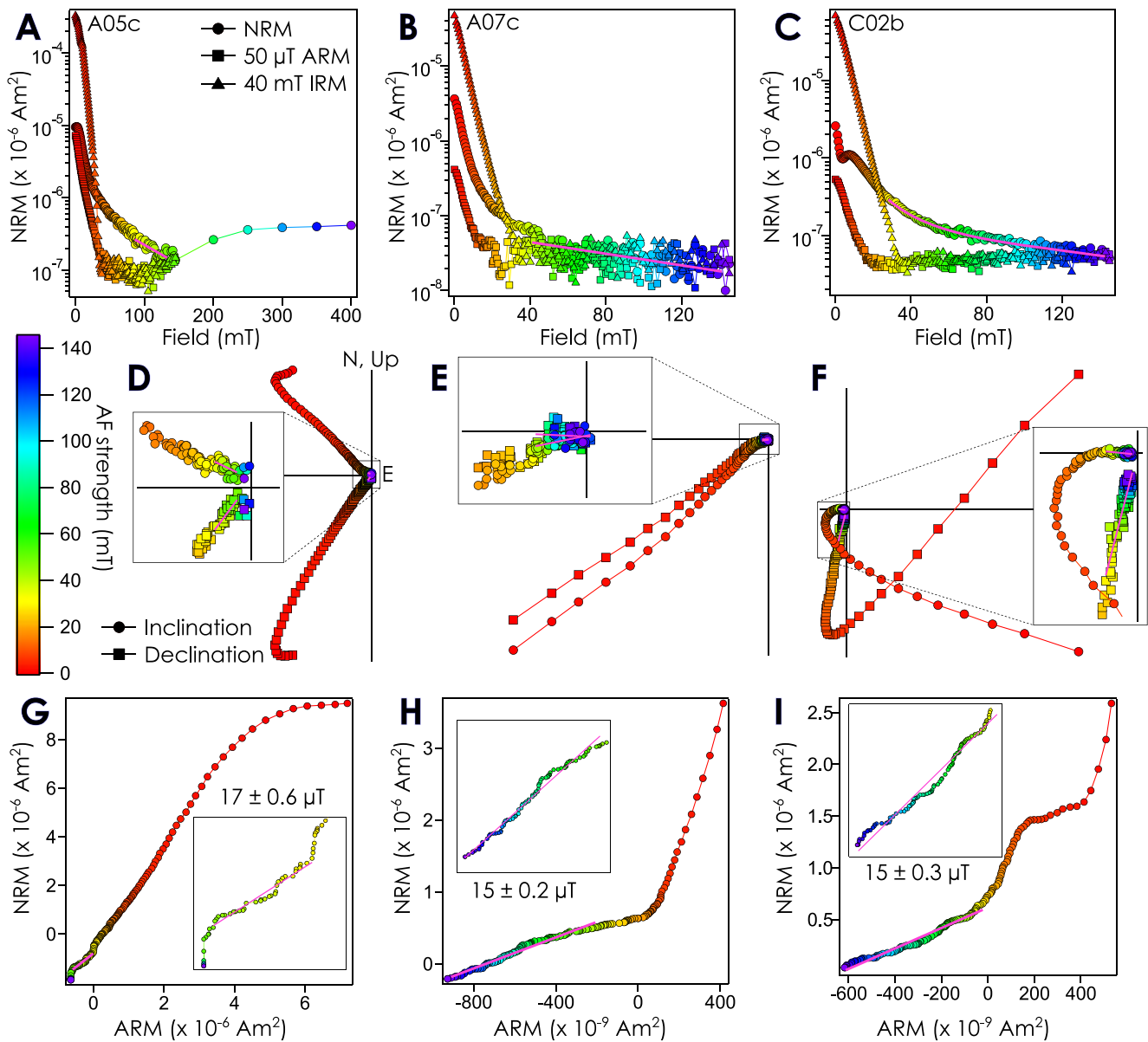


Figure 12. (a–c) show AF demagnetization of an NRM, 50 μT ARM and 40 mT IRM for unbacked BIF specimens A05c, A07c, C02b, respectively. These specimens pass both the pseudo-baked contact test and the fold test. (d–f) show zijderveld diagrams for AF demagnetization of the NRMs, exhibiting high-coercivity, origin-trending components. (g–i) show NRM versus 50 μT ARM plots used to calculate Pseudo-Thellier paleointensities. The gradient of each curve is multiplied by the strength of the applied field and calibrated to correct for non-thermal demagnetization in order to recover a paleointensity estimate.

1.5–1.6 Ga and is observed as perturbations to Pb–Pb, Rb–Sr and Sm–Nd ages (Nishizawa et al., 2005; Polat et al., 2003), but did not have any influence on the observed metamorphic assemblages in the area (Nutman et al., 2022; Arai et al., 2014).

Three sites passed both pseudo-baked contact tests and a fold test, suggesting high-temperature magnetization in the BIF was acquired during Eoarchean amphibolite-grade metamorphism and was not reset by either the Neoproterozoic metamorphic event, nor the Proterozoic hydrothermal event. The BIFs therefore likely preserve a high-temperature magnetization from the Eoarchean. Thermal relaxation times for magnetite also indicate that a tectonothermal event with peak temperatures $<350^\circ\text{C}$ would be insufficient to overprint remanences acquired up to 550°C (Pullaiah et al., 1975). Using the approach outlined in this study, whole-rock, orientable specimens with magnetization ages constrained by U–Pb dating of magnetite (E. B. Watson et al., 2023) can now be used to recover lower-limits on Earth's magnetic field strength throughout the Archean. Using these paleomagnetic

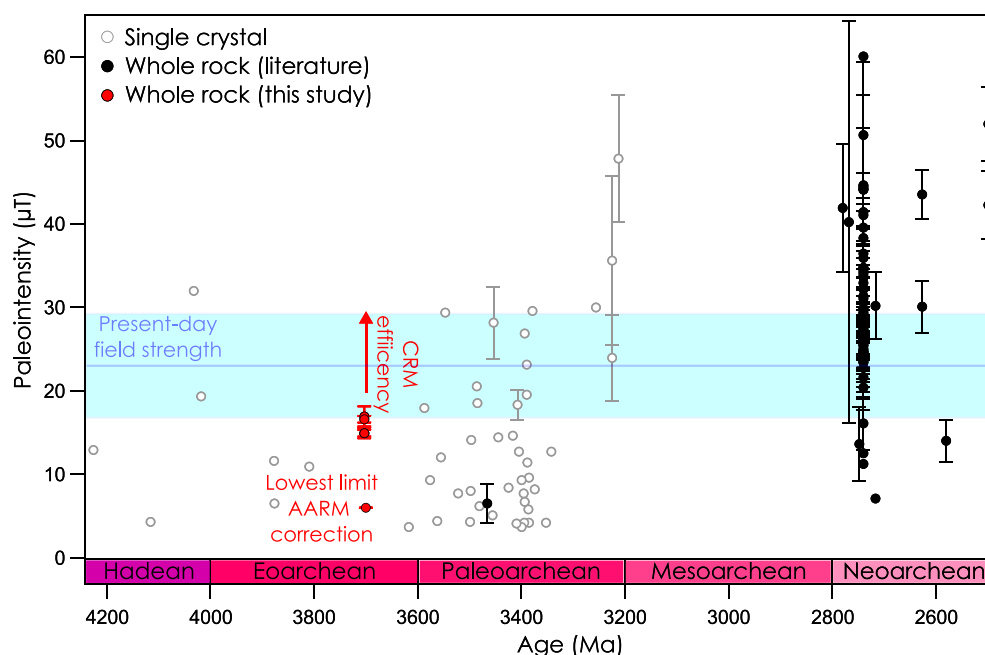


Figure 13. A summary of previous paleointensity studies throughout the Archean and Hadean compiled by Bono et al. (2021). Whole rock studies: Herrero-Bervera et al. (2016); Muxworthy et al. (2013); Biggin et al. (2009); Morimoto et al. (1997); Selkin et al. (2008); Selkin and Tauxe (2000); Yoshihara and Hamano (2000); Miki et al. (2009); Shcherbakova et al. (2017). Single crystal studies: Tarduno et al. (2015); Tarduno et al. (2010, 2007). Note that both the age and paleointensity values of the latter are disputed (Weiss et al., 2018; M. Tang et al., 2019; Borlina et al., 2020; Taylor et al., 2023). The paleointensities for the three BIF specimens measured here are shown in red. The inefficiency of CRM remanence acquisition suggests these intensities likely represent a lower estimate for the Eoarchean geomagnetic field strength. The most extreme anisotropy correction (if the external field was parallel to the principal anisotropy axis) would result in a 220% over-estimation of the ancient magnetic field strength (Selkin & Tauxe, 2000). A lower limit of 6.8 μT is included to reflect the maximum anisotropy correction that could be applied.

observations, combined with atmospheric escape models that use conditions that reflect the increased strength of the early solar wind, will allow us to determine whether Earth's magnetic field drove atmospheric escape of hydrogen, eventually culminating in the GOE (Catling, 2013; Zahnle et al., 2013, 2019).

Pseudo-Thellier paleointensity results for the BIF recover an Eoarchean geomagnetic field strength of at least $15.1 \pm 1.2 \mu\text{T}$. Our results are consistent with previous studies that suggest Earth's geomagnetic field has been active since the Eoarchean (Tarduno et al., 2015, 2020). Given the slow cooling rates post-metamorphism, it is likely that our paleointensity estimate represents a time-averaged field and may have been further reduced from the “true” value of the geomagnetic field by reversals. In addition, the strength of the magnetic field was inefficiently captured by CRM acquisition. Therefore, we cannot rule out that the Archean magnetic field was at least as strong as Earth's magnetic field today. This study highlights current challenges in accurately recovering the strength and stability of the geomagnetic field over Earth's history, although our results suggest behavior of the Eoarchean geomagnetic field was similar to that observed today. Given the much stronger solar wind during the Archean (Vidotto, 2021), our results suggest that atmospheric escape via the polar wind may have been enhanced at this time (Gunell et al., 2018; Sterenborg et al., 2011). Recent dynamo models have predicted the magnetic field declined in intensity from the Archean until the Ediacaran (Davies et al., 2022) immediately prior to inner core nucleation. Further constraints on the stability of the Archean field and how this behavior is manifest in the recovered paleointensity estimates will be required to properly characterize paleointensity trends on billion year timescales. Regardless of its exact strength and stability, our results suggest Earth has sustained an intrinsic magnetic field since at least 3.7 Ga.

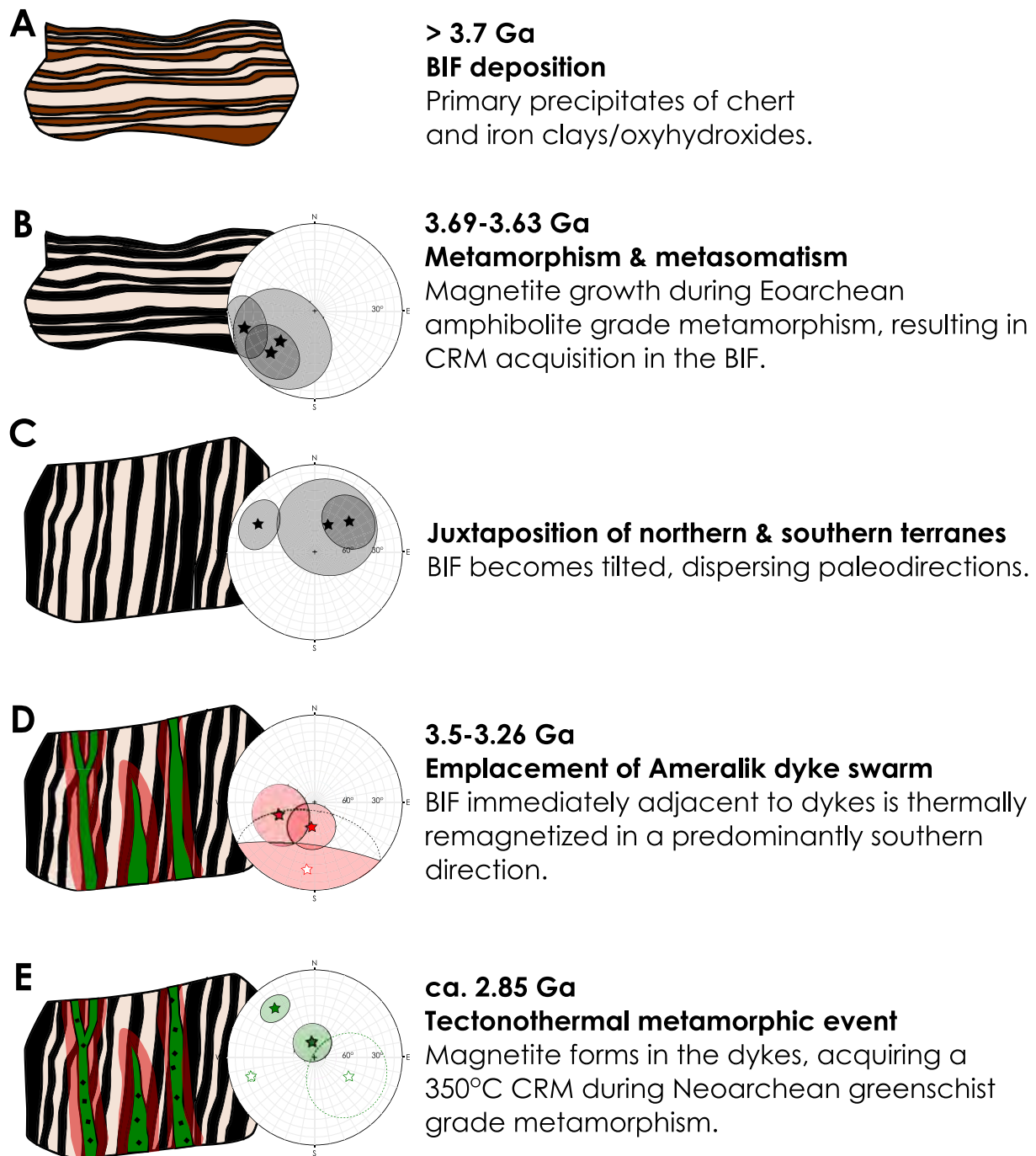


Figure 14. A cartoon schematic showing how the recovered paleomagnetic directions can be interpreted in terms of the geological history of the ISB. (a) The banded iron formation was deposited in anoxic oceans >3.7 Ga ago. The mineralogy of primary precipitates remains debated, but these are likely to include iron clays and oxyhydroxides. (b) During amphibolite grade metamorphism ca. 3.7 Ga ago, magnetite replaced the primary mineralogy in the BIF and acquired a chemical remanent magnetization (CRM). This preservation of this CRM in the BIF is confirmed by both passed pseudo-baked contact tests and a fold test. (c) The BIF experienced folding during juxtaposition of the northern and southern terranes after CRM acquisition, causing the 3.7 Ga directions to disperse. (d) The emplacement of the Ameralik dykes caused the BIF immediately adjacent to the dykes to be thermally reset. The overprints are in a coherent southern direction, and fail the fold test suggesting they post-date folding. (e) The Ameralik dykes acquire an unstable CRM during Neoproterozoic metamorphism due to protracted magnetite growth within the dykes. This metamorphic event was sufficiently low temperature to not entirely thermally overprint the directions in the baked and unbaked BIF.

Table 5

A Summary of Remanence Acquisition Timings and Mechanisms for Each Lithology at Each Site

Eoarchean metamorphic event (ca. 3.69–3.63 Ga)	
Site	Remanence acquisition
8A/A, B, C, D, 4A, 6A	Magnetite forms in the BIF and acquires a TRM during amphibolite grade metamorphism.
3AA	Magnetization in the conglomerate clasts and matrix overprinted during amphibolite grade metamorphism.
Emplacement of Ameralik dykes (3.50–3.26 Ga)	
Site	Remanence acquisition
8A/A, B, C, D, 4A, 6A	Baked BIF acquires TRM associated with reheating during dyke emplacement. Ameralik dykes are unmagnetized, since no magnetite forms in their primary mineralogy.
Neoproterozoic Metamorphic Event (ca. 2.85 Ga)	
Site	Remanence acquisition
8A/A, B, C, D, 4A, 6A	BIF acquires low temperature (<350°C) overprint. Ameralik dykes acquire a CRM as magnetite forms during greenschist grade metamorphism.
3AA	Magnetization in the conglomerate clasts and matrix overprinted during amphibolite grade metamorphism.
Emplacement of norite dyke (2.2 Ga)	
Site	Remanence acquisition
5A	Norite dyke acquires a thermal remanent magnetization during emplacement and cooling.
Proterozoic Hydrothermal Event (ca. 1.5–1.6 Ga)	
Site	Remanence acquisition
B, D, 4A	BIF and Ameralik dykes experience remagnetization during variable metasomatism, faulting and other late-stage, localized events.
3AA, 5A	Magnetization partially overprinted by low temperature hydrothermal alteration.

Acknowledgments

We thank three anonymous reviewers for their detailed and thoughtful comments that have helped to clarify the interpretations presented in this research. CION was funded by the Simons Foundation (Grant 556352), National Geographic (Grant EC-50828R-18) and a Lewis and Clark Astrobiology Grant. BPW also thanks the Simons Foundation for support. AE acknowledges support from the MIT EAPS W. O. Crosby and the Johns Hopkins EPS Morton K. Blaustein Postdoctoral Fellowships. SJM, NMK and MJZ were funded by the Collaborative for Research in Origins (CRiO), which was supported by The John Templeton Foundation (principal investigator: Steven Benner/FIAME); the opinions expressed in this publication are those of the authors and do not necessarily reflect the views of the John Templeton Foundation. We thank Tim Greenfield for assistance with fieldwork, Jeremy Rushton and Simon Tapster for SEM analysis, Jack Ryan and Richard Harrison for FORC analysis, Matt Beverley-Smith for preparation of polished blocks, Steph Halwa and Rich Palin for assistance with thin section images, and Roger Fishman for drone imagery.

Data Availability Statement

Raw data are available from Zenodo: <https://doi.org/10.5281/zenodo.8052859> (Nichols et al., 2024a). A Jupyter notebook and all relevant data used to run the paleomagnetic field tests in PMagPy is available at <https://doi.org/10.5281/zenodo.10379004> (Nichols et al., 2024b). All other details of analysis and data interpretation are included in Supporting Information S1.

References

- Allmendinger, R. W., Cardozo, N. C., & Fisher, D. (2013). Vectors tensors. In *Structural geology algorithms* (pp. 44–98). Cambridge University Press.
- Annen, C. (2017). Factors affecting the thickness of thermal aureoles. *Frontiers in Earth Science*, 5(October), 1–13. <https://doi.org/10.3389/feart.2017.00082>
- Aoki, S., Kabashima, C., Kato, Y., Hirata, T., & Komiya, T. (2016). Influence of contamination on banded iron formations in the Isua supracrustal belt, West Greenland: Reevaluation of the Eoarchean seawater compositions. *Geoscience Frontiers*, 9(4), 1049–1072. <https://doi.org/10.1016/j.gsf.2016.11.016>
- Appel, P. W. U., Fedo, C. M., Moorbath, S., & Myers, J. S. (1998). Recognizable primary volcanic and sedimentary features in a low-strain domain of the highly deformed, oldest known (~3.7 - 3.8 Gyr) Greenstone Belt, Isua, West Greenland. *Terra Nova*, 10(2), 57–62. <https://doi.org/10.1046/j.1365-3121.1998.00162.x>
- Arai, T., Omori, S., Komiya, T., & Maruyama, S. (2014). Intermediate P/T-type regional metamorphism of the Isua Supracrustal Belt, southern west Greenland: The oldest Pacific-type orogenic belt? *Tectonophysics*, 662, 22–39. <https://doi.org/10.1016/j.tecto.2015.05.020>
- Avicé, G., Marty, B., Burgess, R., Hofmann, A., Philippot, P., Zahnle, K., & Zakharov, D. (2018). Evolution of atmospheric xenon and other noble gases inferred from Archean to Paleoproterozoic rocks. *Geochimica et Cosmochimica Acta*, 232, 82–100. <https://doi.org/10.1016/j.gca.2018.04.018>
- Biggin, A. J., de Wit, M. J., Langereis, C. G., Zegers, T. E., Voûte, S., Dekkers, M. J., & Drost, K. (2011). Palaeomagnetism of Archean rocks of the Onverwacht Group, Barberton Greenstone Belt (southern Africa): Evidence for a stable and potentially reversing geomagnetic field at ca. 3.5Ga. *Earth and Planetary Science Letters*, 302(3–4), 314–328. <https://doi.org/10.1016/j.epsl.2010.12.024>

- Biggin, A. J., Strik, G. H., & Langereis, C. G. (2009). The intensity of the geomagnetic field in the late-Archaean: New measurements and an analysis of the updated IAGA palaeointensity database. *Earth Planets and Space*, *61*(1), 9–22. <https://doi.org/10.1186/BF03352881>
- Bono, R. K., Paterson, G. A., van der Boon, A., Engbers, Y. A., Grappone, J. M., Handford, B., et al. (2021). The PINT database: A definitive compilation of absolute palaeomagnetic intensity determinations since 4 billion years ago. *Geophysical Journal International*, *229*(1), 522–545. <https://doi.org/10.1093/gji/ggab490>
- Bono, R. K., Tarduno, J. A., Nimmo, F., & Cottrell, R. D. (2019). Young inner core inferred from Ediacaran ultra-low geomagnetic field intensity. *Nature Geoscience*, *12*(2), 143–147. <https://doi.org/10.1038/s41561-018-0288-0>
- Borlina, C., Weiss, B., Lima, E., Tang, F., Taylor, R., Einsle, J., et al. (2020). Re-evaluating the evidence for a Hadean-Eoarchean dynamo. *Science Advances*, *6*(15), 1–9. <https://doi.org/10.1126/sciadv.aav9634>
- Buchan, K. (2007). Baked contact test. In D. Gubbins & E. Herrero-Bervera (Eds.), *Encyclopedia of geomagnetism and paleomagnetism* (pp. 35–55). Springer. https://doi.org/10.1007/springerreference_77506
- Cardozo, N. C., & Allmendinger, R. W. (2013). Spherical projections with OSXStereonet. *Computers & Geosciences*, *51*, 193–205. <https://doi.org/10.1016/j.cageo.2012.07.021>
- Catling, D. C. (2013). The great oxidation event transition. In *Treatise on geochemistry* (2nd ed., Vol. 6, pp. 177–195). <https://doi.org/10.1016/B978-0-08-095975-7.01307-3>
- Catling, D. C., & Zahnle, K. J. (2020). The Archean atmosphere. *Science Advances*, *6*(9), eaax1420. <https://doi.org/10.1126/sciadv.aax1420>
- Cherniak, D. J., Lanford, W. A., & Ryerson, F. J. (1991). Lead diffusion in apatite and zircon using ion implantation and Rutherford Backscattering techniques. *Geochimica et Cosmochimica Acta*, *55*(6), 1663–1673. [https://doi.org/10.1016/0016-7037\(91\)90137-T](https://doi.org/10.1016/0016-7037(91)90137-T)
- Crowley, J. L. (2003). U-Pb geochronology of 3810–3630 Ma granitoid rocks south of the Isua greenstone belt, southern West Greenland. *Precambrian Research*, *126*(3–4), 235–257. [https://doi.org/10.1016/S0301-9268\(03\)00097-4](https://doi.org/10.1016/S0301-9268(03)00097-4)
- Crowley, J. L., White, R. V., Myers, J. S., & Dunning, G. R. (2000). U-Pb geochronology and geologic significance of the two oldest known mafic dyke swarms on earth: 3659 Ma Inaluk dykes and 3490 Ma Tarssartoq dykes, southern west Greenland. *Atlantic Geology*, *36*, 3659.
- Davies, C. J., Bono, R. K., Meduri, D. G., Aubert, J., Greenwood, S., & Biggin, A. J. (2022). Dynamo constraints on the long-term evolution of Earth's magnetic field strength. *Geophysical Journal International*, *228*(1), 316–336. <https://doi.org/10.1093/gji/ggab342>
- Dunlop, D. J., & Ozdemir, O. (1993). Thermal demagnetization of VRM and pTRM of single domain magnetite: No evidence for anomalously high unblocking temperatures. *Geophysical Research Letters*, *20*(18), 1939–1942. <https://doi.org/10.1029/93gl02137>
- Dymek, R. F., & Klein, C. (1988). Chemistry, petrology and origin of banded iron-formation lithologies from the 3800 Ma Isua Supracrustal Belt. *West Greenland*, *39*(4), 247–302. [https://doi.org/10.1016/0301-9268\(88\)90022-8](https://doi.org/10.1016/0301-9268(88)90022-8)
- Erel, Y., Harlavan, Y., Stein, M., & Blum, J. D. (1997). U-Pb dating of Fe-rich phases using a sequential leaching method. *Geochimica et Cosmochimica Acta*, *61*(8), 1697–1703. [https://doi.org/10.1016/S0016-7037\(97\)00028-8](https://doi.org/10.1016/S0016-7037(97)00028-8)
- Fedo, C. M. (2000). Setting and origin for problematic rocks from the >3.7 Ga Isua Greenstone Belt, southern west Greenland: Earth's oldest coarse clastic sediments. *Precambrian Research*, *101*(1), 69–78. [https://doi.org/10.1016/S0301-9268\(99\)00100-X](https://doi.org/10.1016/S0301-9268(99)00100-X)
- Fedo, C. M., Myers, J. S., & Appel, P. W. U. (2001). Depositional setting and paleogeographic implications of Earth's oldest supracrustal rocks, the >3.7 Ga Isua greenstone belt, West Greenland. *Sedimentary Geology*, *141–142*, 61–77. [https://doi.org/10.1016/S0037-0738\(01\)00068-9](https://doi.org/10.1016/S0037-0738(01)00068-9)
- Frei, R., Bridgwater, D., Rosing, M., & Stecher, O. (1999). Controversial Pb-Pb and Sm-Nd isotope results in the early Archean Isua (West Greenland) oxide iron formation: Preservation of primary signatures versus secondary disturbances. *Geochimica et Cosmochimica Acta*, *63*(3–4), 473–488. [https://doi.org/10.1016/S0016-7037\(98\)00290-7](https://doi.org/10.1016/S0016-7037(98)00290-7)
- Frei, R., & Polat, A. (2007). Source heterogeneity for the major components of ~ 3.7 Ga banded iron formations (Isua Greenstone Belt, Western Greenland): Tracing the nature of interacting water masses in BIF formation. *Earth and Planetary Science Letters*, *253*(1–2), 266–281. <https://doi.org/10.1016/j.epsl.2006.10.033>
- Friend, C. R. L., & Nutman, A. P. (2005). Complex 3670–3500 Ma orogenic episodes superimposed on juvenile crust accreted between 3850 and 3690 Ma, Itsaq gneiss complex, Southern West Greenland. *The Journal of Geology*, *113*(4), 375–397. <https://doi.org/10.1086/430239>
- Gattacceca, J., & Rochette, P. (2004). Toward a robust normalized magnetic paleointensity method applied to meteorites. *Earth and Planetary Science Letters*, *227*(3–4), 377–393. <https://doi.org/10.1016/j.epsl.2004.09.013>
- Gelcich, S., Davis, D. W., & Spooner, E. T. (2005). Testing the apatite-magnetite geochronometer: U-Pb and ⁴⁰Ar/³⁹Ar geochronology of plutonic rocks, massive magnetite-apatite tabular bodies, and IOCG mineralization in Northern Chile. *Geochimica et Cosmochimica Acta*, *69*(13), 3367–3384. <https://doi.org/10.1016/j.gca.2004.12.020>
- Graham, J. W. (1949). The stability and significance of magnetism in sedimentary rocks. *Journal of Geophysical Research*, *54*(2), 131–167. <https://doi.org/10.1029/jz054i002p00131>
- Gronoff, G., Arras, P., Baraka, S., Bell, J. M., Cessateur, G., Cohen, O., et al. (2020). Atmospheric escape processes and planetary atmospheric evolution. *Journal of Geophysical Research: Space Physics*, *125*(8), 1–77. <https://doi.org/10.1029/2019JA027639>
- Gruau, G., Rosing, M., Bridgwater, D., & Gill, R. C. (1996). Resetting of Sm-Nd systematics during metamorphism of >3.7-Ga rocks: Implications for isotopic models of early Earth differentiation. *Chemical Geology*, *133*(1–4), 225–240. [https://doi.org/10.1016/S0009-2541\(96\)00092-7](https://doi.org/10.1016/S0009-2541(96)00092-7)
- Gunell, H., Maggiolo, R., Nilsson, H., Stenberg Wieser, G., Slapak, R., Lindkvist, J., et al. (2018). Why an intrinsic magnetic field does not protect a planet against atmospheric escape. *Astronomy and Astrophysics*, *614*, 1–8. <https://doi.org/10.1051/0004-6361/201832934>
- Halevy, I., Feldman, Y., Popovitz-Biro, R., Schuster, E. M., & Alesker, M. (2017). A key role for green rust in the Precambrian oceans and the genesis of iron formations. *Nature Geoscience*, *10*(2), 135–139. <https://doi.org/10.1038/ngeo2878>
- Halgedahl, S. L., & Jarrard, R. D. (1995). Low-temperature behavior of single-domain through multidomain magnetite. *Earth and Planetary Science Letters*, *130*(1–4), 127–139. [https://doi.org/10.1016/0012-821X\(94\)00260-6](https://doi.org/10.1016/0012-821X(94)00260-6)
- Harrison, R. J., & Feinberg, J. M. (2008). FORCinel: An improved algorithm for calculating first-order reversal curve distributions using locally weighted regression smoothing. *Geochemistry, Geophysics, Geosystems*, *9*(5). <https://doi.org/10.1029/2008GC001987>
- Herrero-Bervera, E., Krasa, D., & Van Kranendonk, M. J. (2016). A whole rock absolute paleointensity determination of dacites from the Duffer Formation (ca. 3.467 Ga) of the Pilbara Craton, Australia: An impossible task? *Physics of the Earth and Planetary Interiors*, *258*, 51–62. <https://doi.org/10.1016/j.pepi.2016.07.001>
- Herzberg, C., Condie, K., & Korenaga, J. (2010). Thermal history of the Earth and its petrological expression. *Earth and Planetary Science Letters*, *292*(1–2), 79–88. <https://doi.org/10.1016/j.epsl.2010.01.022>
- Hodoch, J. P. (1982). Magnetostrictive control of coercive force in multidomain magnetite. *Nature*, *298*(5874), 542–544. <https://doi.org/10.1038/298542a0>
- Jaeger, J. C. (1964). Thermal effects of intrusions. *Reviews of Geophysics*, *2*(3), 443–466. <https://doi.org/10.1029/rg002i003p00443>
- Jelinek, V. (1981). Characterization of the magnetic fabric of rocks. *Tectonophysics*, *79*(3–4), 63–67. [https://doi.org/10.1016/0040-1951\(81\)90110-4](https://doi.org/10.1016/0040-1951(81)90110-4)

- Johnson, C. L., Constable, C. G., Tauxe, L., Barendregt, R., Brown, L. L., Coe, R. S., et al. (2008). Recent investigations of the 0-5 Ma geomagnetic field recorded by lava flows. *Geochemistry, Geophysics, Geosystems*, 9(4). <https://doi.org/10.1029/2007GC001696>
- Johnson, J. E., Muhling, J. R., Cosmidis, J., Rasmussen, B., & Templeton, A. S. (2018). Low-Fe(III) Greenalite was a primary mineral from Neoproterozoic Oceans. *Geophysical Research Letters*, 45(7), 3182–3192. <https://doi.org/10.1002/2017GL076311>
- Kirschvink, J. L. (1980). The least-squares line and plane and the analysis of palaeomagnetic data. *Geophysical Journal of the Royal Astronomical Society*, 62(3), 699–718. <https://doi.org/10.1111/j.1365-246x.1980.tb02601.x>
- Kobayashi, K. (1959). Chemical remanent magnetization of ferromagnetic minerals and its application to rock magnetism. *Journal of Geomagnetism and Geoelectricity*, 10(3), 99–117. <https://doi.org/10.5636/jgg.10.99>
- Komiya, T., Hayashi, M., Maruyama, S., & Yurimoto, H. (2002). Intermediate-P/T type Archean metamorphism of the Isua supracrustal belt: Implications for secular change of geothermal gradients at subduction zones and for Archean plate tectonics. *American Journal of Science*, 302(9), 806–826. <https://doi.org/10.2475/ajs.302.9.806>
- Komiya, T., Maruyama, S., Hirata, T., Yurimoto, H., & Nohda, S. (2004). Geochemistry of the oldest MORB and OIB in the Isua Supracrustal Belt, southern West Greenland: Implications for the composition and temperature of early Archean upper mantle. *Island Arc*, 13(1), 47–72. <https://doi.org/10.1111/j.1440-1738.2003.00416.x>
- Konhauer, K. O., Planavsky, N. J., Hardisty, D. S., Robbins, L. J., Warchola, T. J., Haugaard, R., et al. (2017). Iron formations: A global record of Neoproterozoic to Palaeoproterozoic environmental history. *Earth-Science Reviews*, 172(June), 140–177. <https://doi.org/10.1016/j.earscrv.2017.06.012>
- Landeau, M., Aubert, J., & Olson, P. (2017). The signature of inner-core nucleation on the geodynamo. *Earth and Planetary Science Letters*, 465, 193–204. <https://doi.org/10.1016/j.epsl.2017.02.004>
- Landeau, M., Fournier, A., Nataf, H.-C., C  bron, D., & Schaeffer, N. (2022). Sustaining Earth's magnetic dynamo. *Nature Reviews Earth & Environment*, 3(4), 255–269. <https://doi.org/10.1038/s43017-022-00264-1>
- Lay, T., Hernlund, J., & Buffett, B. A. (2008). Core–mantle boundary heat flow. *Nature Geoscience*, 1, 25–32. <https://doi.org/10.1038/ngeo.2007.44>
- Lowrie, W., & Fuller, M. (1971). On the alternating field demagnetization characteristics of multidomain thermoremanent magnetization in magnetite. *Journal of Geophysical Research*, 76(26), 6339–6349. <https://doi.org/10.1029/jb076i026p06339>
- Lundin, R., Lammer, H., & Ribas, I. (2007). Planetary magnetic fields and solar forcing: Implications for atmospheric evolution. *Space Science Reviews*, 129(1–3), 245–278. <https://doi.org/10.1007/s11214-007-9176-4>
- Marco, S., Ron, H., McWilliams, M. O., & Stein, M. (1998). High-resolution record of geomagnetic secular variation from late Pleistocene Lake Lisan sediments (paleo Dead Sea). *Earth and Planetary Science Letters*, 161(1–4), 145–160. [https://doi.org/10.1016/S0012-821X\(98\)00146-0](https://doi.org/10.1016/S0012-821X(98)00146-0)
- Maxbauer, D. P., Feinberg, J. M., & Fox, D. L. (2016). MAX UnMix: A web application for unmixing magnetic coercivity distributions. *Computers & Geosciences*, 95, 140–145. <https://doi.org/10.1016/j.cageo.2016.07.009>
- Miki, M., Taniguchi, A., Yokoyama, M., Gouzu, C., Hyodo, H., Uno, K., et al. (2009). Palaeomagnetism and geochronology of the proterozoic dolerite dyke from southwest Greenland: Indication of low palaeointensity. *Geophysical Journal International*, 179(1), 18–34. <https://doi.org/10.1111/j.1365-246X.2009.04258.x>
- Moorbath, S., O'Nions, R. K., & Pankhurst, R. J. (1973). Early archaean age for the Isua iron formation, West Greenland. *Nature*, 245(5421), 138–139. <https://doi.org/10.1038/s41565-017-0010-1>
- Morimoto, C., Otofuiji, Y. I., Miki, M., Tanaka, H., & Itaya, T. (1997). Preliminary palaeomagnetic results of an Archean dolerite dyke of west Greenland: Geomagnetic field intensity at 2.8 Ga. *Geophysical Journal International*, 128(3), 585–593. <https://doi.org/10.1111/j.1365-246X.1997.tb05320.x>
- Muxworthy, A. R., Evans, M. E., Scourfield, S. J., & King, J. G. (2013). Paleointensity results from the late-Archaean Modipe Gabbro of Botswana. *Geochemistry, Geophysics, Geosystems*, 14(7), 2198–2205. <https://doi.org/10.1002/ggge.20142>
- Nabelek, P. I., Hofmeister, A. M., & Whittington, A. G. (2012). The influence of temperature-dependent thermal diffusivity on the conductive cooling rates of plutons and temperature-time paths in contact aureoles. *Earth and Planetary Science Letters*, 317–318, 157–164. <https://doi.org/10.1016/j.epsl.2011.11.009>
- Newell, A. J. (2000). The Lowrie-Fuller test: Single-domain and micromagnetic theory. *Earth and Planetary Science Letters*, 183(1–2), 335–346. [https://doi.org/10.1016/S0012-821X\(00\)00271-5](https://doi.org/10.1016/S0012-821X(00)00271-5)
- Nichols, C. I. O., Weiss, B. P., Eyster, A., Martin, C. R., Maloof, A. C., Kelly, N. M., et al. (2024a). Possible Eoarchean records of the geomagnetic field preserved in the Isua Supracrustal Belt, southern west Greenland [Dataset]. *Zenodo*. <https://doi.org/10.5281/zenodo.8052859>
- Nichols, C. I. O., Weiss, B. P., Eyster, A., Martin, C. R., Maloof, A. C., Kelly, N. M., et al. (2024b). TinySpaceMagnet/Greenland_Paleomagnetic_Data: Greenland paleomagnetic data (version 1.0) [Analysed Dataset]. *Zenodo*. <https://doi.org/10.5281/zenodo.1037900>
- Nilsson, M. K., S  derlund, U., Ernst, R. E., Hamilton, M. A., Scherst  n, A., & Armitage, P. E. (2010). Precise U-Pb baddeleyite ages of mafic dykes and intrusions in southern West Greenland and implications for a possible reconstruction with the Superior craton. *Precambrian Research*, 183(3), 399–415. <https://doi.org/10.1016/j.precamres.2010.07.010>
- Nishizawa, M., Takahata, N., Terada, K., Komiya, T., Ueno, Y., & Sano, Y. (2005). Rare-earth element, lead, carbon, and nitrogen geochemistry of apatite-bearing metasediments from the 3.8 Ga Isua supracrustal belt, West Greenland. *International Geology Review*, 47(9), 952–970. <https://doi.org/10.2747/0020-6814.47.9.952>
- Nutman, A. P., Bennett, V., & Friend, C. (2015). The emergence of the Eoarchean proto-arc: Evolution of a c. 3700 Ma convergent plate boundary at Isua, southern West Greenland. *Geological Society - Special Publications*, 389(1), 113–133. <https://doi.org/10.1144/SP389.5>
- Nutman, A. P. (1986). The early Archaean to Proterozoic history of the Isukasia area, southern West Greenland. *Gronlands Geologiske Unders  gelse Bulletin*, 154(22295), 1–80. <https://doi.org/10.34194/bullggu.v154.6696>
- Nutman, A. P. (2017). Isua Stromatolites – Understanding the field setting [Technical Report]. <https://doi.org/10.13140/RG.2.2.13602.63681>
- Nutman, A. P., Allaart, J. A. N. H., Bridgwater, D., Dimroth, E., & Rosing, M. (1984). Stratigraphic and geochemical evidence for the depositional environment of the early Archean Isua Supracrustal Belt, southern west Greenland. *Precambrian Research*, 25(4), 365–396. [https://doi.org/10.1016/0301-9268\(84\)90010-x](https://doi.org/10.1016/0301-9268(84)90010-x)
- Nutman, A. P., Bennett, V. C., Friend, C. R., Yi, K., & Lee, S. R. (2015). Mesoarchaean collision of Kapisilik terrane 3070 Ma juvenile arc rocks and > 3600 Ma Isukasia terrane continental crust (Greenland). *Precambrian Research*, 258, 146–160. <https://doi.org/10.1016/j.precamres.2014.12.013>
- Nutman, A. P., & Friend, C. R. (2009). New 1:20,000 scale geological maps, synthesis and history of investigation of the Isua supracrustal belt and adjacent orthogneisses, southern West Greenland: A glimpse of Eoarchaean crust formation and orogeny. *Precambrian Research*, 172(3–4), 189–211. <https://doi.org/10.1016/j.precamres.2009.03.017>

- Nutman, A. P., Friend, C. R., Bennett, V. C., Yi, K., & Van Kranendonk, M. (2022). Review of the Isua supracrustal belt area (Greenland) Eoarchean geology from integrated 1:20,000 scale maps, field observations and laboratory data: Constraints on early geodynamics. *Precambrian Research*, 379(June), 106785. <https://doi.org/10.1016/j.precamres.2022.106785>
- Nutman, A. P., Friend, C. R., & Paxton, S. (2009). Detrital zircon sedimentary provenance ages for the Eoarchean Isua supracrustal belt southern West Greenland: Juxtaposition of an imbricated ca. 3700 Ma juvenile arc against an older complex with 3920-3760 Ma components. *Precambrian Research*, 172(3–4), 212–233. <https://doi.org/10.1016/j.precamres.2009.03.019>
- Nutman, A. P., Friend, C. R. L., Bennett, V. C., & MCGregor, V. R. (2004). Dating of the Ameralik dyke swarms of the Nuuk district, southern West Greenland: Mafic intrusion events starting from c. 3510 Ma. *Journal of the Geological Society*, 161(3), 421–430. <https://doi.org/10.1144/0016-764903-043>
- Nutman, A. P., Hagiya, H., & Maruyama, S. (1995). SHRIMP U-Pb single zircon geochronology of a Proterozoic mafic dyke, Isukasia, southern West Greenland. *Bulletin of the Geological Society of Denmark*, 42, 17–2210. <https://doi.org/10.37570/bgsd-1995-42-02>
- Olson, P. (2013). The new core paradox. *Science*, 342(6157), 431–432. <https://doi.org/10.1126/science.1243477>
- Paterson, G. A., Heslop, D., & Pan, Y. (2016). The pseudo-Thellier palaeointensity method: New calibration and uncertainty estimates. *Geophys*, 207(3), 1596–1608. <https://doi.org/10.1093/gji/ggw349>
- Pearson, D. G., Scott, J. M., Liu, J., Schaeffer, A., Wang, L. H., van Hunen, J., et al. (2021). Deep continental roots and cratons. *Nature*, 596(7871), 199–210. <https://doi.org/10.1038/s41586-021-03600-5>
- Polat, A., Hofmann, A. W., Münker, C., Regelous, M., & Appel, P. W. (2003). Contrasting geochemical patterns in the 3.7-3.8 Ga pillow basalt cores and rims, Isua greenstone belt, Southwest Greenland: Implications for postmagmatic alteration processes. *Geochimica et Cosmochimica Acta*, 67(3), 441–457. [https://doi.org/10.1016/S0016-7037\(02\)01094-3](https://doi.org/10.1016/S0016-7037(02)01094-3)
- Pullaiah, G., Irving, E., Buchan, K., & Dunlop, D. (1975). Magnetization changes caused by burial and uplift. *Earth and Planetary Science Letters*, 28(2), 133–143. <https://doi.org/10.1017/s0252921100050831>
- Rasmussen, B., & Muhling, J. R. (2018). Making magnetite late again: Evidence for widespread magnetite growth by thermal decomposition of siderite in Hamersley banded iron formations. *Precambrian Research*, 306, 64–93. <https://doi.org/10.1016/j.precamres.2017.12.017>
- Rollinson, H. (2002). The metamorphic history of the Isua Greenstone Belt, West Greenland. *Geological Society, London, Special Publications*, 199(1), 329–350. <https://doi.org/10.1144/GSL.SP.2002.199.01.16>
- Rollinson, H. (2003). Metamorphic history suggested by garnet-growth chronologies in the Isua Greenstone Belt, West Greenland. *Precambrian Research*, 126(3–4), 181–196. [https://doi.org/10.1016/S0301-9268\(03\)00094-9](https://doi.org/10.1016/S0301-9268(03)00094-9)
- Sasselov, D. D., Grotzinger, J. P., & Sutherland, J. D. (2020). The origin of life as a planetary phenomenon. *Science Advances*, 6(6), 1–10. <https://doi.org/10.1126/sciadv.aax3419>
- Schmidt, P. W., & Clark, D. A. (1994). Palaeomagnetism and magnetic anisotropy of proterozoic banded-iron formations and iron ores of the Hamersley Basin Western Australia. *Exploration Geophysics*, 24(2), 223–226. <https://doi.org/10.1071/EG993223>
- Selkin, P. A., Gee, J. S., Meurer, W. P., & Hemming, S. R. (2008). Paleointensity record from the 2.7 Ga stillwater complex, Montana. *Geochemistry, Geophysics, Geosystems*, 9(12). <https://doi.org/10.1029/2008GC001950>
- Selkin, P. A., Gee, J. S., Tauxe, L., Meurer, W. P., & Newell, A. J. (2000). The effect of remanence anisotropy on paleointensity estimates: A case study from the Archean stillwater complex. *Earth and Planetary Science Letters*, 183(3–4), 403–416. [https://doi.org/10.1016/S0012-821X\(00\)00292-2](https://doi.org/10.1016/S0012-821X(00)00292-2)
- Selkin, P. A., & Tauxe, L. (2000). Long-term variations in palaeointensity. *Philosophical Transactions of the Royal Society A: Mathematical, Physical & Engineering Sciences*, 358(1768), 1065–1088. <https://doi.org/10.1098/rsta.2000.0574>
- Shcherbakova, V. V., Lubnina, N. V., Shcherbakov, V. P., Zhidkov, G. V., & Tsel'movich, V. A. (2017). Paleointensity determination on Neoproterozoic dikes within the Vodlozerskii terrane of the Karelian craton. *Izvestiya - Physics of the Solid Earth*, 53(5), 714–732. <https://doi.org/10.1134/S1069351317050111>
- Sterenberg, M. G., Cohen, O., Drake, J. J., & Gombosi, T. I. (2011). Modeling the young Sun's solar wind and its interaction with Earth's paleomagnetosphere. *Journal of Geophysical Research*, 116(1), 1–17. <https://doi.org/10.1029/2010JA016036>
- Stokking, L. B., & Tauxe, L. (1987). Acquisition of chemical remanent magnetization by synthetic iron oxide. *Nature*, 18–20.
- Stokking, L. B., & Tauxe, L. (1990). Properties of chemical remanence in synthetic hematite: Testing theoretical predictions. *Journal of Geophysical Research*, 95(89), 639–652. <https://doi.org/10.1029/jb095ib08p12639>
- Tang, F., Taylor, R. J. M., Einsle, J. F., Borlina, C. S., Fu, R. R., Weiss, B. P., et al. (2019). Secondary magnetite in ancient zircon precludes analysis of a Hadean geodynamo. *Proceedings of the National Academy of Sciences*, 116(2), 407–412. <https://doi.org/10.1073/pnas.1811074116>
- Tang, M., Lee, C. T. A., Costin, G., & Höfer, H. E. (2019). Recycling reduced iron at the base of magmatic orogens. *Earth and Planetary Science Letters*, 528, 115827. <https://doi.org/10.1016/j.epsl.2019.115827>
- Tarduno, J. A., Blackman, E. G., & Mamajek, E. E. (2014). Detecting the oldest geodynamo and attendant shielding from the solar wind: Implications for habitability. *Physics of the Earth and Planetary Interiors*, 233, 68–87. <https://doi.org/10.1016/j.pepi.2014.05.007>
- Tarduno, J. A., Cottrell, R. D., Bono, R. K., Oda, H., Davis, W. J., Fayek, M., et al. (2020). Paleomagnetism indicates that primary magnetite in zircon records a strong Hadean geodynamo. *Proceedings of the National Academy of Sciences*, 117(5), 1–10. <https://doi.org/10.1073/pnas.1916553117>
- Tarduno, J. A., Cottrell, R. D., Bono, R. K., Rayner, N., Davis, W. J., Zhou, T., et al. (2023). Hadaean to Palaeoarchaean stagnant-lid tectonics revealed by zircon magnetism. *Nature*, 618(7965), 531–536. <https://doi.org/10.1038/s41586-023-06024-5>
- Tarduno, J. A., Cottrell, R. D., Davis, W. J., Nimmo, F., & Bono, R. K. (2015). A Hadean to Paleoproterozoic geodynamo recorded by single zircon crystals. *Science*, 352(July), 521–524. <https://doi.org/10.1126/science.aaa9114>
- Tarduno, J. A., Cottrell, R. D., Watkeys, M. K., & Bauch, D. (2007). Geomagnetic field strength 3.2 billion years ago recorded by single silicate crystals. *Nature*, 446(7136), 657–660. <https://doi.org/10.1038/nature05667>
- Tarduno, J. A., Cottrell, R. D., Watkeys, M. K., Hofmann, A., Dubrovine, P. V., Mamajek, E. E., et al. (2010). Geodynamo, solar wind, and magnetopause 3.4 to 3.45 billion years ago. *Science*, 327(5970), 1238–1240. <https://doi.org/10.1126/science.1183445>
- Tauxe, L., & Kent, D. V. (2004). A simplified statistical model for the geomagnetic field and the detection of shallow bias in paleomagnetic inclinations: Was the ancient magnetic field dipolar? *Geophysical Monograph Series*, 145, 101–115. <https://doi.org/10.1029/145GM08>
- Tauxe, L., Klystra, N., & Constable, C. (1991). Bootstrap statistics for paleomagnetic data. *Journal of Geophysical Research*, 96(B7), 11723–11740. <https://doi.org/10.1029/91jb00572>
- Tauxe, L., Shaar, R., Jonestrask, L., Swanson-Hysell, N., Minnett, R., Koppers, A., et al. (2016). PmagPy: Software package for paleomagnetic data analysis and a bridge to the magnetics information consortium (MagIC) database. *Geochemistry, Geophysics, Geosystems*, 17(6), 2450–2463. <https://doi.org/10.1002/2015GC006307>

- Tauxe, L., & Watson, G. S. (1994). The fold test: An eigen analysis approach. *Earth and Planetary Science Letters*, *122*(3–4), 331–341. [https://doi.org/10.1016/0012-821X\(94\)90006-X](https://doi.org/10.1016/0012-821X(94)90006-X)
- Taylor, R. J., Reddy, S. M., Saxey, D. W., Rickard, W. D., Tang, F., Borlina, C. S., et al. (2023). Direct age constraints on the magnetism of Jack Hills zircon. *Science Advances*, *9*(1), eadd1511. <https://doi.org/10.1126/sciadv.add1511>
- Tosca, N. J., Guggenheim, S., & Pufahl, P. K. (2016). An authigenic origin for Precambrian greenalite: Implications for iron formation and the chemistry of ancient seawater. *Bulletin of the Geological Society of America*, *128*(3–4), 511–530. <https://doi.org/10.1130/B31339.1>
- Valet, J. P. (2003). Time variations in geomagnetic intensity. *Reviews of Geophysics*, *41*(1). <https://doi.org/10.1029/2001RG000104>
- Vidotto, A. A. (2021). The evolution of the solar wind. *Living Reviews in Solar Physics*, *18*(1), 1–86. <https://doi.org/10.1007/s41116-021-00029-w>
- Watson, E. B., Cherniak, D. J., Nichols, C. I., & Weiss, B. P. (2023). Pb diffusion in magnetite: Dating magnetite crystallization and the timing of remanent magnetization in banded iron formation. *Chemical Geology*, *640*, 121748. <https://doi.org/10.1016/j.chemgeo.2023.121748>
- Watson, G. S. (1965). A test for randomness of directions. *Geophysical Supplements to the Monthly Notices of the Royal Astronomical Society*, *7*(4), 160–161. <https://doi.org/10.1111/j.1365-246x.1956.tb05561.x>
- Watson, G. S. (1983). Large sample theory of the Langevin distribution. *Journal of Statistical Planning and Inference*, *8*(3), 245–256. [https://doi.org/10.1016/0378-3758\(83\)90043-5](https://doi.org/10.1016/0378-3758(83)90043-5)
- Weiss, B. P., Fu, R. R., Einsle, J. F., Glenn, D. R., Kehayias, P., Bell, E. A., et al. (2018). Secondary magnetic inclusions in detrital zircons from the Jack Hills, Western Australia and implications for the origin of the geodynamo microscopy. *Geology*, *46*(5), 427–430. <https://doi.org/10.1130/G39938.1>
- Weiss, B. P., Maloof, A. C., Tailby, N., Ramezani, J., Fu, R. R., Hanus, V., et al. (2015). Pervasive remagnetization of detrital zircon host rocks in the Jack Hills, Western Australia and implications for records of the early geodynamo. *Earth and Planetary Science Letters*, *430*, 115–128. <https://doi.org/10.1016/j.epsl.2015.07.067>
- White, R. V., Crowley, J. L., & Myers, J. S. (2000). Earth's oldest well-preserved mafic dyke swarms in the vicinity of the Isua greenstone belt, southern West Greenland. *Episodes*, *72*, 65–72. <https://doi.org/10.34194/ggub.v186.5217>
- Yoshihara, A., & Hamano, Y. (2000). Intensity of the Earth's magnetic field in late Archean obtained from diabase dikes of the Slave Province, Canada. *Physics of the Earth and Planetary Interiors*, *117*(1–4), 295–307. [https://doi.org/10.1016/S0031-9201\(99\)00103-X](https://doi.org/10.1016/S0031-9201(99)00103-X)
- Zahnle, K. J., Catling, D. C., & Claire, M. W. (2013). The rise of oxygen and the hydrogen hourglass. *Chemical Geology*, *362*, 26–34. <https://doi.org/10.1016/j.chemgeo.2013.08.004>
- Zahnle, K. J., Gacesa, M., & Catling, D. C. (2019). Strange messenger: A new history of hydrogen on Earth, as told by Xenon. *Geochimica et Cosmochimica Acta*, *244*, 56–85. <https://doi.org/10.1016/j.gca.2018.09.017>
- Zhou, T., Tarduno, J. A., Nimmo, F., Cottrell, R. D., Bono, R. K., Ibanez-mejia, M., et al. (2022). Early Cambrian renewal of the geodynamo and the origin of inner core structure. *Nature Communications*, *13*, 1–7. <https://doi.org/10.1038/s41467-022-31677-7>

1 **Supporting Information for “Possible Eoarchean**
2 **records of the geomagnetic field preserved in the Isua**
3 **Supracrustal Belt, southern west Greenland”**

4 **Claire I. O. Nichols^{a,b}, Benjamin P. Weiss^a, Athena Eyster^c, Craig R. Martin^a.**
5 **Adam C. Maloof^d, Nigel M. Kelly^e, Mike J. Zawaski^{f,g}, Stephen J. Mojzsis**
6 **^{f,h,i,j}, E. Bruce Watson^k, Daniele J. Cherniak^l**

7 ^aDepartment of Earth, Atmospheric and Planetary Sciences, Massachusetts Institute of Technology, 77
8 Massachusetts Avenue, Cambridge, MA 02139, USA

9 ^bDepartment of Earth Sciences, University of Oxford, South Parks Road, Oxford, OX1 3AN, UK

10 ^cDepartment of Earth and Climate Sciences, Tufts University, Medford, MA 02155, USA

11 ^dDepartment of Geosciences, Princeton University, Guyot Hall, Princeton, NJ 08544, USA

12 ^eBruker Nano Analytics, 5465 E. Cheryl Parkway, Madison, Wisconsin 53711, USA

13 ^fDepartment of Geological Sciences, University of Colorado Boulder, UCB 399, Boulder, CO 80309, USA

14 ^gDepartment of Geology and Geophysics, Texas A&M University, 108 Halbouty Building, 3115 TAMU,
15 College Station, Texas 77843-3115, USA

16 ^hOrigins Research Institute, Research Centre for Astronomy and Earth Sciences, MTA Centre of

17 Excellence, 15-17 Konkoly Thege Miklos ut Budapest, 1121 Hungary

18 ⁱDepartment of Lithospheric Research, University of Vienna UZA 2, Josef-Holaubek-Platz 2 A-1090
19 Vienna, Austria

20 ^jInstitute for Earth Sciences, Friedrich-Schiller University Burgweg 11 07749 Jena, Germany

21 ^kDepartment of Earth and Environmental Sciences, Rensselaer Polytechnic Institute, 110 Eighth Street,
22 Troy, NY 12180, USA

23 ^lIon Beam Laboratory, State University of New York at Albany, 1400 Washington Avenue Albany, NY
24 12222, USA

25 **Contents of this file**

- 26 1. Text S1 to S5
27 2. Caption for Dataset S1
28 3. Captions for Tables S1 to S13
29 4. Figures S1 to S19

30 **Additional Supporting Information (Files uploaded separately)**

- 31 1. Dataset S1 (Jupyter notebook)
32 2. Tables S1 to S13 (Excel files)

33 **S1. Geological mapping of the Isua Supracrustal Belt (ISB)**

34 The northernmost part of the northeastern ISB is surrounded by the Greenland ice sheet
 35 and the degree of exposure is controlled by the extent of perennial snow. In July 2019,
 36 there was extensive melting of the perennial snow and the area was well-exposed. Ex-
 37 amples of the types of exposures we are sampled are shown in Figure 6 and 11. Previ-
 38 ous work has not mapped this area in detail (Nutman et al., 2009). We therefore mapped
 39 the newly-exposed region with 5–10 m resolution (Figure 5). Mafic intrusives were found
 40 to intrude exclusively into the banded iron formation (BIF), while the feldspar-rich in-
 41 trusives intrude exclusively into the bedded chert. The contact between the chert and
 42 BIF was not exposed and may be unconformable. Patches of plagioclase megacrysts have
 43 been observed in some Ameralik dykes (White et al., 2000; Komiya et al., 2002; Nutman
 44 et al., 2004).

45 **S2. Petrography**

46 Thin sections were prepared by Spectrum Petrographics Inc. and polished cores were pre-
 47 pared in the Department of Earth Sciences, University of Oxford. Thin sections were ex-
 48 amined using a petrographic microscope under both plane and crossed polarized trans-
 49 mitted light. Scanning electron microscopy (SEM) analyses were carried out at the British
 50 Geological Survey on carbon-coated, polished core slices. Backscatter electron (BSE) im-
 51 ages were acquired using an accelerating voltage of 15 kV, a working distance of 10 mm,
 52 a 20 ms dwell time and a 5 μm stepsize. Mineral compositions were semi-quantified us-
 53 ing electron dispersive X-ray spectroscopy (EDS) phase mapping. Measurements were
 54 analysed using the Zeiss Mineralogic software.

55 Thin sections of the BIF and chert lithologies were examined using a petrographic
 56 microscope (Figure 10). The cherts are quartz-rich and bands are defined by minor mag-
 57 netite. Finer scale laminations within the quartz-rich layers are defined by cummingtonite
 58 and grunerite as previously observed in the quartz-silicate-rich iron-formation defined
 59 by ref. Dymek (1988). The presence of abundant cummingtonite and grunerite gives this
 60 lithology its beige colouration in outcrop (Figure 5C).

61 The BIF is characterised by sharp mm-scale bands of quartz and magnetite (Fig-
 62 ure 10). The amphiboles grunerite, cummingtonite and actinolite are observed growing
 63 along the edges of the magnetite-rich bands and most likely formed during greenschist-
 64 grade metamorphism at 2.57 Ga (Arai et al., 2014; Polat et al., 2003). The low grade
 65 metamorphism and slight deformation is also observed in quartz grains under cross po-
 66 larised light. The quartz grains are equant in size and have grain boundaries approach-
 67 ing equilibrium (120° angles). A crenulation cleavage is also observed in specimen C06
 68 at an oblique angle to the magnetite-quartz bands (Figure 10).

69 Figure 4 shows BSE images of the BIF. EDS phase mapping shows that the light
 70 bands are predominantly quartz and the dark bands are predominantly magnetite. No
 71 other iron-oxide or iron-sulfide phases are present. Along the edges of the bands, the am-
 72 phiboles cummingtonite/grunerite and actinolite are observed and are likely evidence of
 73 amphibolite-grade Eoarchean metamorphism (Dymek, 1988; Arai et al., 2014; Polat et
 74 al., 2003). Small apatite grains are observed and range in size from 10–100 μm and most
 75 likely formed during hydrothermal events at 3.9 and 1.5 Ga (Nishizawa et al., 2005; Frei
 76 et al., 1999). These apatite grain sizes observed in the EDS phase maps are used to in-
 77 terpret the closure temperature of U-Pb system for apatite dating of the Isua BIF (Nishizawa
 78 et al., 2005).

79 **S3. Paleointensity Fidelity Tests**

80 Fidelity tests were carried out by comparing the 50 μT anhysteretic remanent magne-
 81 tization (ARM) to the 40 mT isothermal remanent magnetization (IRM). Since the IRM
 82 was only acquired over 40 mT (Figure 15), paleointensity estimates were retrieved be-
 83 tween 0–40 mT. The difference, D' (Bryson et al., 2017), between the retrieved paleoin-

84 tensity, I , and the applied ARM field, L was calculated using:

$$D' = \left| \frac{I - L}{L} \right| \quad (1)$$

85 and the error, E , was calculated from the uncertainty on the paleointensity W , using:

$$E = \frac{W}{L} \quad (2)$$

86 and the fidelity parameters are summarised in Table 11. We found good agreement be-
87 tween the applied field and recovered field, with specimens A05c and A07c both return-
88 ing a paleointensity within 10% of the ARM imparted (Figure 15).

89 **S4. Pb diffusion measurements in magnetite**

90 The following section summarises the method and results from E. B. Watson et al. (2023).
91 Lead diffusion in natural magnetite (Fe_3O_4) was characterized over the temperature range
92 500–675°C using the powder-source method (E. B. Watson & Dohmen, 2010). Magnetite
93 crystals (Moriah, New York, U.S.A.) were sawn into slabs 5–8 mm² in area and ~ 1 mm
94 thick using a low-speed diamond saw, with slab orientations parallel to cubic 001 or oc-
95 tahedral 111 forms. One surface of each slab was polished using routine procedures of
96 the Rensselaer Polytechnic Institute laboratory that have been demonstrated to yield
97 surfaces free of dislocations and other lattice damage (E. B. Watson et al., 2016).

98 A mixture of PbSO_4 and Fe_2O_3 (1:1 mass proportions) was prepared for use as a
99 powder source to provide Pb^{2+} ions at the surfaces of the magnetite crystals for diffu-
100 sive exchange with Fe^{2+} in the magnetite. The combination of Fe_2O_3 in the source and
101 the magnetite samples themselves constituted a solid-state oxygen fugacity buffer (magnetite-
102 hematite; MH), ensuring that the stable oxidation of Pb during the diffusion experiments
103 was 2+, as expected in natural settings where both magnetite and hematite are present.

104 Preparation for a diffusion experiment involved packing a polished magnetite slab
105 in PbSO_4 - Fe_2O_3 powder source at the pre-sealed end of a silica-glass tube, which was
106 then evacuated with a mechanical pump and sealed off with an H₂-O₂ torch. This en-
107 closed, fO₂-buffered system (SiO_2 ampoule and contents) was suspended in a vertical-
108 tube furnace and held at temperature for a preset duration to allow Pb^{2+} from the source
109 to exchange diffusively with Fe^{2+} from the magnetite. The diffusion experiment was ter-
110 minated by removing the SiO_2 ampoule from the furnace and allowing it to cool in air.
111 The magnetite slab was cleaned of source powder by sonication in ethanol, and Pb up-
112 take was characterized by depth-profiling perpendicular to the surface using Rutherford
113 backscattering spectroscopy (RBS; see Cherniak et al. (2010); E. B. Watson and Dohmen
114 (2010)). Diffusivities were recovered from Pb profiles by fitting the concentration vs. depth
115 data to the solution to the non-steady state diffusion equation for 1-D diffusion into a
116 semi-infinite medium with constant surface concentration. A time series was conducted
117 at 650°C to ensure that our approach yielded diffusivities independent of experiment du-
118 ration.

119 The activation energy, E , and pre-exponential factor, D_o , for Pb in magnetite were
120 found to be 98 kJ mol⁻¹ and 9.0×10^{-17} m²s⁻¹, respectively. The diffusion rate of Pb^{2+}
121 in apatite was previously experimentally determined and E and D_o were found to be 229 kJ mol⁻¹
122 and 2×10^{-8} m s⁻², respectively (Cherniak et al., 1991). The Dodson closure temper-
123 ature, T_c of the system can then be calculated using the approach described by (Dodson,
124 1973) where

$$T_c = \frac{E}{R \ln A \tau \frac{D_o}{a^2}} \quad (3)$$

125 R is the gas constant (8.314 J mol⁻¹ K⁻¹), A is a numerical constant which depends on
126 the geometry and decay constant of the parent and is assumed to be 55 here, represent-
127 ing diffusion from a sphere (Dodson, 1973). τ is the time constant which is given by $\tau =$

128 $\frac{-RT}{E \frac{dT}{dt}}$ where T is absolute temperature and taken to be 50°C and $\frac{dT}{dt}$ is the cooling rate.
 129 We conservatively assume that the cooling rate following metamorphism was between
 130 1–100°C Myr⁻¹ given the uncertainty in the definition of Archean ‘tectonics’ and there-
 131 fore the mechanism of exhumation during early ‘tectonothermal’ events (Webb et al., 2020;
 132 Arai et al., 2014; Kaczmarek et al., 2016). a is the grain size, which is varied from 1 nm
 133 to 1 mm to cover magnetite grains with magnetic properties varying from superparam-
 134 agnetic to multidomain.

135 Representative grain sizes of magnetite in BIF samples from sites A, C and D were
 136 estimated magnetically. We measured the magnitude of the magnetic moment of the NRM
 137 at room temperature (M_{NRM}) and then measured the moment again after having cooled
 138 the samples down to -210°C by submerging them in liquid nitrogen ($M_{-210^\circ C}$). The amount
 139 of remanence removed allows average grain size to be estimated using the relationship
 140 empirically defined by Halgedahl and Jarrard (1995):

$$\frac{M_{-210^\circ C}}{M_{NRM}} = 0.714 - 0.618 \ln a \quad (4)$$

141 We found that the specimens retained between 49–71% of their remanence, correspond-
 142 ing to an average grain size of $\sim 1\text{--}26 \mu\text{m}$ (Figure 3). The closure temperature of Pb in
 143 magnetite therefore varies from 120–400°C in the Isua BIF (Figure 1).

144 The grain size of apatite in the BIF was previously assumed to be 30 μm (Nishizawa
 145 et al., 2005). However, from our EDS phase maps (see *Petrography* section) we find the
 146 grains range in size from $\sim 10\text{--}100 \mu\text{m}$. Based on our grain size and cooling rate esti-
 147 mates, the closure temperature of Pb in apatite varies from 360–530°C (Figure 2).

148 **S5. The demagnetization behaviour of the conglomerate, BIF and Ameralik dykes**

149 In order to confirm that the high temperature (HT) components of demagnetization in
 150 the BIF were carried by stable, single domain or single vortex magnetite grains, we also
 151 carried out alternating field (AF) demagnetization to verify these components are also
 152 high coercivity (HC). We found that HC and HT components define the same direction,
 153 although AF demagnetization did a slightly better job of removing unstable components
 154 carried by multidomain magnetite (Figure 7).
 155

156 Paleomagnetic field tests were carried out at seven sites: 3AA, 4A, 6A, 8A/A, B,
 157 C and D. At site 3AA we conducted a conglomerate test. We found that both matrix
 158 and clasts defined coherent LT and HT directions, suggesting pervasive overprinting of
 159 the magnetization after deposition, most likely during Eoarchean and Neoproterozoic meta-
 160 morphism (Figure 8).

161 At sites 4A, 6A, 8A/A, B, C and D, Ameralik dykes are intruded through the BIF.
 162 We sampled these localities with the intention of carrying out baked contact tests. How-
 163 ever, we found that the magnetization in the Ameralik dykes, which were emplaced 3.26–
 164 3.5 Ga (Nutman et al., 2004) had been overprinted during greenschist-grade Neoproterozoic
 165 metamorphism, resulting in unstable demagnetization trends that unblock at 350°C (Fig-
 166 ure 9).

167 Pseudo-baked contact tests at sites 4A, B and D compared the directions of the
 168 baked BIF, immediately adjacent to each Ameralik dyke intrusion, with unbaked BIF
 169 at a sufficient distance from the intrusion to have avoided being thermally reset. The lo-
 170 cation of each specimen, and representative thermal demagnetization trends are shown
 171 in Figures 14, 13 and 12. At sites 4A and B, the magnetization has been overprinted fol-
 172 lowing dyke emplacement, most likely due to localized faulting and associated metasoma-
 173 tism. At site D, sampling was not extended to a sufficient distance to avoid the ther-
 174 mal affects of the intrusion. All three of these sites failed our pseudo-baked contact test.

175

References

176

Arai, T., Omori, S., Komiya, T., & Maruyama, S. (2014). Intermediate P/T-type regional metamorphism of the Isua Supracrustal Belt, southern west Greenland: The oldest Pacific-type orogenic belt? *Tectonophysics*, *662*, 22–39. doi: 10.1016/j.tecto.2015.05.020

180

Bryson, J. F., Weiss, B. P., Harrison, R. J., Herrero-Albillos, J., & Kronast, F. (2017). Paleomagnetic evidence for dynamo activity driven by inward crystallization of a metallic asteroid. *Earth and Planetary Science Letters*, *472*(April), 152–163. doi: 10.1016/j.epsl.2017.05.026

184

Cashman, K. V. (1993). Relationship between plagioclase crystallization and cooling rate in basaltic melts. *Contributions to Mineralogy and Petrology*, *113*(1), 126–142. doi: 10.1007/BF00320836

187

Cherniak, D. J., Hervig, R., Koepke, J., Zhang, Y., & Zhao, D. (2010). Analytical methods in diffusion studies. *Reviews in Mineralogy and Geochemistry*, *72*, 107–170. doi: 10.2138/rmg.2010.72.4

190

Cherniak, D. J., Lanford, W. A., & Ryerson, F. J. (1991). Lead diffusion in apatite and zircon using ion implantation and Rutherford Backscattering techniques. *Geochimica et Cosmochimica Acta*, *55*(6), 1663–1673. doi: 10.1016/0016-7037(91)90137-T

194

Dodson, M. H. (1973). Closure temperature in cooling geochronological and petrological systems. *Contributions to Mineralogy and Petrology*, *40*, 259–274. Retrieved from <http://www.raco.cat/index.php/Dovella/article/view/20118> doi: 10.1007/BF00373790

196

Dymek, R. F. (1988). Chemistry, Petrology and Origin of Banded Iron-Formation Lithologies From the 3800 Ma Isua Supracrustal Belt, West Greenland. *Journal of Metamorphic Geology*, *39*, 247–302.

201

Frei, R., Bridgwater, D., Rosing, M., & Stecher, O. (1999). Controversial Pb-Pb and Sm-Nd isotope results in the early Archean Isua (West Greenland) oxide iron formation: Preservation of primary signatures versus secondary disturbances. *Geochimica et Cosmochimica Acta*, *63*(3-4), 473–488. doi: 10.1016/S0016-7037(98)00290-7

206

Halgedahl, S. L., & Jarrard, R. D. (1995). Low-temperature behavior of single-domain through multidomain magnetite. *Earth and Planetary Science Letters*, *130*(1-4), 127–139. doi: 10.1016/0012-821X(94)00260-6

208

Jelinek, V. (1981). Characterization of the magnetic fabric of rocks. *Tectonophysics*, *79*(3-4), 63–67. doi: 10.1016/0040-1951(81)90110-4

209

Kaczmarek, M. A., Reddy, S. M., Nutman, A. P., Friend, C. R., & Bennett, V. C. (2016). Earth's oldest mantle fabrics indicate Eoarchean subduction. *Nature Communications*, *7*, 1–7. Retrieved from <http://dx.doi.org/10.1038/ncomms10665> doi: 10.1038/ncomms10665

211

Komiya, T., Hayashi, M., Maruyama, S., & Yurimoto, H. (2002). Intermediate-P/T type Archean metamorphism of the Isua supracrustal belt: Implications for secular change of geothermal gradients at subduction zones and for Archean plate tectonics. *American Journal of Science*, *302*(9), 806–826. doi: 10.2475/ajs.302.9.806

215

Maxbauer, D. P., Feinberg, J. M., & Fox, D. L. (2016). MAX UnMix: A web application for unmixing magnetic coercivity distributions. *Computers and Geosciences*, *95*, 140–145. doi: 10.1016/j.cageo.2016.07.009

220

Nishizawa, M., Takahata, N., Terada, K., Komiya, T., Ueno, Y., & Sano, Y. (2005). Rare-earth element, lead, carbon, and nitrogen geochemistry of apatite-bearing metasediments from the similar to 3.8 Ga Isua supracrustal belt, West Greenland. *International Geology Review*, *47*(9), 952–970. doi: 10.2747/0020-6814.47.9.952

223

Nutman, A. P., Friend, C. R. L., Bennett, V. C., & MCGregor, V. R. (2004). Dating of the Ameralik dyke swarms of the Nuuk district, southern West Greenland:

228

- 230 mafic intrusion events starting from c. 3510 Ma. *Journal of the Geological*
 231 *Society*, 161(3), 421–430. Retrieved from [http://jgs.lyellcollection.org/](http://jgs.lyellcollection.org/cgi/doi/10.1144/0016-764903-043)
 232 [cgi/doi/10.1144/0016-764903-043](http://jgs.lyellcollection.org/cgi/doi/10.1144/0016-764903-043) doi: 10.1144/0016-764903-043
- 233 Nutman, A. P., Friend, C. R. L., & Paxton, S. (2009). Detrital zircon sedimentary
 234 provenance ages for the Eoarchaeon Isua supracrustal belt southern West
 235 Greenland: Juxtaposition of an imbricated ca. 3700 Ma juvenile arc against
 236 an older complex with 3920–3760 Ma components. *Precambrian Research*,
 237 172(3–4), 212–233. doi: 10.1016/j.precamres.2009.03.019
- 238 Polat, A., Hofmann, A. W., Münker, C., Regelous, M., & Appel, P. W. (2003). Con-
 239 trasting geochemical patterns in the 3.7–3.8 Ga pillow basalt cores and rims,
 240 Isua greenstone belt, Southwest Greenland: Implications for postmagmatic
 241 alteration processes. *Geochimica et Cosmochimica Acta*, 67(3), 441–457. doi:
 242 10.1016/S0016-7037(02)01094-3
- 243 Samperton, K. M., Bell, E. A., Barboni, M., Brenhin Keller, C., & Schoene, B.
 244 (2017). Zircon age-temperature-compositional spectra in plutonic rocks. *Geol-*
 245 *ogy*, 45(11), 983–986. doi: 10.1130/G38645.1
- 246 Tauxe, L., & Kent, D. V. (2004). A simplified statistical model for the geomagnetic
 247 field and the detection of shallow bias in paleomagnetic inclinations: Was the
 248 ancient magnetic field dipolar? *Geophysical Monograph Series*, 145, 101–115.
 249 doi: 10.1029/145GM08
- 250 Warren, C. J., Kelley, S. P., Sherlock, S. C., & McDonald, C. S. (2012). Meta-
 251 morphic rocks seek meaningful cooling rate: Interpreting $^{40}\text{Ar}/^{39}\text{Ar}$ ages
 252 in an exhumed ultra-high pressure terrane. *Lithos*, 155, 30–48. Re-
 253 trieved from <http://dx.doi.org/10.1016/j.lithos.2012.08.011> doi:
 254 10.1016/j.lithos.2012.08.011
- 255 Watson, E. B., Cherniak, D. J., Nichols, C. I., & Weiss, B. P. (2023). Pb diffusion
 256 in magnetite: Dating magnetite crystallization and the timing of remanent
 257 magnetization in banded iron formation. *Chemical Geology*, 640(September),
 258 121748. doi: 10.1016/j.chemgeo.2023.121748
- 259 Watson, E. B., Cherniak, D. J., Thomas, J. B., Hanchar, J. M., & Wirth, R. (2016).
 260 Crystal surface integrity and diffusion measurements on Earth and plane-
 261 tary materials. *Earth and Planetary Science Letters*, 450, 346–354. Re-
 262 trieved from <http://dx.doi.org/10.1016/j.epsl.2016.06.043> doi:
 263 10.1016/j.epsl.2016.06.043
- 264 Watson, E. B., & Dohmen, R. (2010). Non-traditional and emerging methods for
 265 characterizing diffusion in minerals and mineral aggregates. *Reviews in Miner-*
 266 *alogy and Geochemistry*, 72(November), 61–105. doi: 10.2138/rmg.2010.72.3
- 267 Watson, G. S. (1965). A test for randomness of directions. *Geophysical Supplements*
 268 *to the Monthly Notices of the Royal Astronomical Society*, 7(4), 160–161.
- 269 Webb, A. A. G., Müller, T., Zuo, J., Haproff, P. J., & Ramírez-Salazar, A. (2020).
 270 A non-plate tectonic model for the Eoarchean Isua supracrustal belt. *Litho-*
 271 *sphere*, 12(1), 166–179. doi: 10.1130/L1130.1
- 272 White, R. V., Crowley, J. L., & Myers, J. S. (2000). Earth ’ s oldest well-preserved
 273 mafic dyke swarms in the vicinity of the Isua greenstone belt , southern West
 274 Greenland. *Episodes*, 72, 65–72.

275 **Data Set S1. Jupyter Notebook - Paleomagnetic Field Tests**

276 All directional data and an accompanying Jupyter Notebook are available at [https://](https://github.com/TinySpaceMagnet/GreenlandPaleomagneticData)
 277 github.com/TinySpaceMagnet/GreenlandPaleomagneticData to run the paleomag-
 278 netic field tests analyses including the pseudo-baked contact tests, the fold test and the
 279 reversal tests.

Table 1. Components and their coercivity spectra calculated using MAX UnMix (Maxbauer et al., 2016).

Table 2. A table summarizing the paleomagnetic components identified during a conglomerate test at site 3AA. The first column is the specimen name, the second column is the lithology (either clast or matrix), the third and fourth column and the start and end temperature across which the component was fitted, the fifth column is the number of points in the component fit, the sixth and seventh column are the declination and inclination of the identified component, the eighth column indicates whether the component is origin-trending (where $MAD > dAng$), the ninth column is the maximum angular deviation, the tenth column is the deviation angle and the eleventh column indicates whether the component fit was anchored to the origin.

Table 3. A table of the critical resultant vector values R_o for Watson's randomness test (G. S. Watson, 1965).

Table 4. A table summarizing the paleomagnetic components identified in the 2.2 Ga norite dyke at site 5A. The first column is the specimen name, the second column is the lithology, the third column is the distance from the dyke contact, the fourth and fifth column are the start and end temperature across which the component was fitted, the sixth column is the component, the seventh column is the number of points in the component fit, the eighth and ninth column are the declination and inclination of the identified component, the tenth column indicates whether the component is origin-trending (where $MAD > dAng$), the eleventh column is the maximum angular deviation, the twelfth column is the deviation angle and the thirteenth column indicates whether the component fit was anchored to the origin.

Table 5. A table summarizing the paleomagnetic components identified during a baked contact test at site 8A and A. The first column is the specimen name, the second column is the lithology, the third column is the distance from the dyke 8A-BIF contact, the fourth column is the distance from the dyke A-BIF contact, the fifth and sixth column and the start and end temperature across which the component was fitted, the seventh temperature is the component, the eighth column is the number of points in the component fit, the ninth and tenth column are the declination and inclination of the identified component, the eleventh column indicates whether the component is origin-trending (where $MAD > dAng$), the twelfth column is the maximum angular deviation, the thirteenth column is the deviation angle and the fourteenth column indicates whether the component fit was anchored to the origin.

Table 6. A table summarizing the paleomagnetic components identified during a baked contact test at site 6A. The first column is the specimen name, the second column is the lithology, the third column is the distance from the dyke-BIF contact, the fourth and fifth column and the start and end temperature across which the component was fitted, the sixth column is the number of points in the component fit, the seventh and eighth column are the declination and inclination of the identified component, the ninth column indicates whether the component is origin-trending (where $MAD > dAng$), the tenth column is the maximum angular deviation, the eleventh column is the deviation angle and the twelfth column indicates whether the component fit was anchored to the origin.

Table 7. A table summarizing the paleomagnetic components identified during a baked contact test at site C. The first column is the specimen name, the second column is the lithology, the third column is the distance from the dyke 8A-BIF contact, the fourth column is the distance from the dyke A-BIF contact, the fifth and sixth column and the start and end temperature across which the component was fitted, the seventh and eighth column are the start and end field for AF demagnetized specimens, the ninth column is the component, the tenth column is the number of points in the component fit, the eleventh and twelfth column are the declination and inclination of the identified component, the thirteenth column indicates whether the component is origin-trending (where $MAD > dAng$), the fourteenth column is the maximum angular deviation, the fifteenth column is the deviation angle and the sixteenth column indicates whether the component fit was anchored to the origin.

Table 8. A table summarizing the paleomagnetic components identified during a baked contact test at site D. The first column is the specimen name, the second column is the lithology, the third column is the distance from the dyke contact, the fourth and fifth column are the start and end temperature across which the component was fitted, the sixth column is the component, the seventh column is the number of points in the component fit, the eighth and ninth column are the declination and inclination of the identified component, the tenth column indicates whether the component is origin-trending (where $MAD > dAng$), the eleventh column is the maximum angular deviation, the twelfth column is the deviation angle and the thirteenth column indicates whether the component fit was anchored to the origin.

Table 9. A table summarizing the paleomagnetic components identified during a baked contact test at site B. The first column is the specimen name, the second column is the lithology, the third column is the distance from the dyke 8A-BIF contact, the fourth column is the distance from the dyke A-BIF contact, the fifth and sixth column and the start and end temperature across which the component was fitted, the seventh and eighth column are the start and end field for AF demagnetized specimens, the ninth column is the component, the tenth column is the number of points in the component fit, the eleventh and twelfth column are the declination and inclination of the identified component, the thirteenth column indicates whether the component is origin-trending (where $MAD > dAng$), the fourteenth column is the maximum angular deviation, the fifteenth column is the deviation angle and the sixteenth column indicates whether the component fit was anchored to the origin.

Table 10. A table summarizing the paleomagnetic components identified during a baked contact test at site 4A. The first column is the specimen name, the second column is the lithology, the third column is the distance from the dyke-BIF contact, the fourth and fifth column and the start and end temperature across which the component was fitted, the sixth column is the number of points in the component fit, the seventh and eighth column are the declination and inclination of the identified component, the ninth column indicates whether the component is origin-trending (where $MAD > dAng$), the tenth column is the maximum angular deviation, the eleventh column is the deviation angle and the twelfth column indicates whether the component fit was anchored to the origin.

Table 11. A summary of fidelity tests by comparing the AF demagnetization of the $50 \mu T$ ARM against a 40 mT IRM for specimens A05c, A07c and C02b. Paleointensities were calculated for each distinct change in gradient. Uncertainties are one standard deviation.

Table 12. A summary of paleointensity estimates by comparing the AF demagnetization of the NRM against a $50 \mu T$ ARM for specimens A05c, A07c and C02b. Paleointensities were calculated for each distinct change in gradient. High coercivity paleointensities are taken to represent the original paleointensity. Uncertainties are stated to two standard deviations.

Table 13. Anisotropy of anhysteretic remanence magnetization (AARM) data collected for 11 specimens. Specimens were given a $50 \mu T$ ARM in 6 directions (xx, yy, zz, xy, xz, yz). The principal susceptibilities ($\kappa_1, \kappa_2, \kappa_3$) and their logarithmic values (η_1, η_2, η_3) are calculated for each specimen. The values were used to calculate the lineation degree (L), foliation degree (F), anisotropy degree (P) and the corrected anisotropy degree (P'). Details of calculations are given in Jelinek (1981).

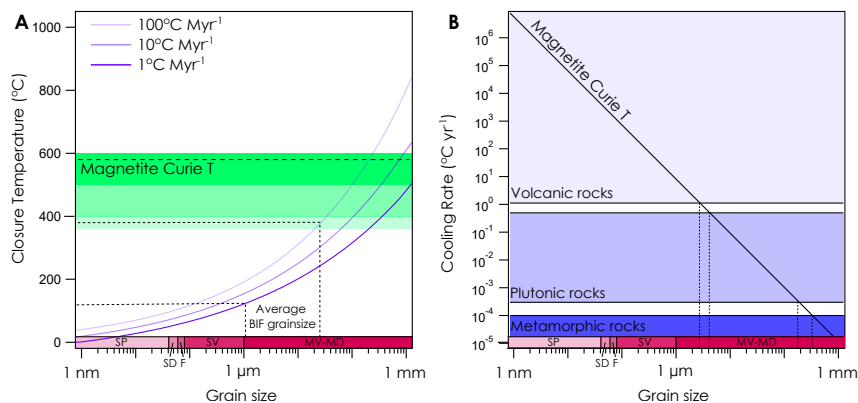


Figure 1. **A** The Dodson closure temperature of Pb in magnetite plotted against the grain size of magnetite (Dodson, 1973). The closure temperature is plotted for a range of cooling rates (purple curves) assuming cooling from amphibolite grade metamorphism (peak temperature 500°C). The average grain size of magnetite in the BIFs studied here are plotted between the dashed lines to show their expected Pb closure temperatures depending on cooling rate. The green regions show greenschist to amphibolite grade metamorphic conditions. The magnetic state of the magnetite grains is shown by the red band, where SP = superparamagnetic, SD = single domain, F = flower state, SV = single vortex, MV = multivortex and MD = multi-domain. **B** The cooling rate and magnetite grain size at which the magnetite Pb-Pb age would directly correspond to the magnetite Curie temperature. This is particularly important for igneous rocks, which cool through the Curie temperature and acquire a thermal remanent magnetization (TRM). The representative cooling rates for volcanic and plutonic igneous rocks and metamorphic rocks are shown (Cashman, 1993; Samperton et al., 2017; Warren et al., 2012)

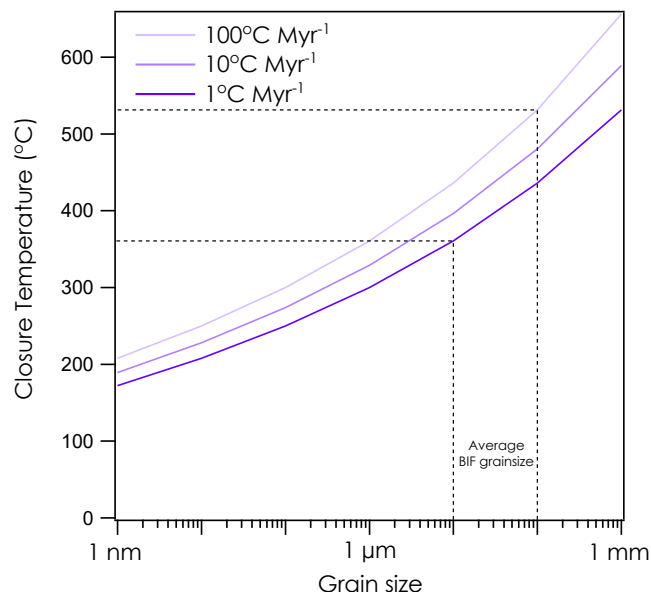


Figure 2. The Dodson closure temperature of the U-Pb apatite system for cooling rates ranging from 1–100°C Myr⁻¹ and grain sizes of 10–100 μm estimated from SEM images (Figure 4). The closure temperature ranges from 360–530°C. The activation energy of the system is 229 kJ mol⁻¹ and the pre-exponential factor is 2×10^{-8} m² s⁻¹ (Nishizawa et al., 2005).

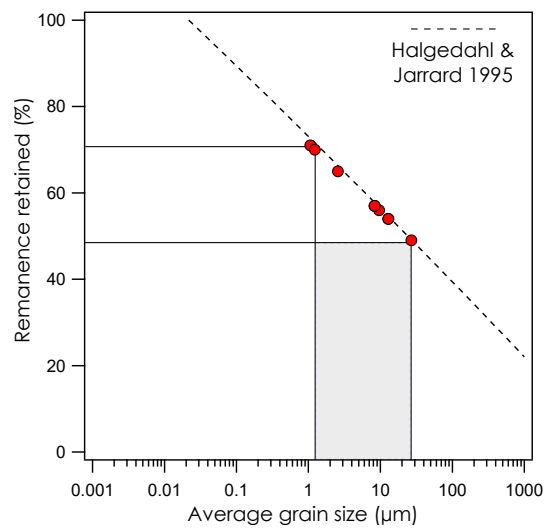


Figure 3. The percentage of magnetic remanence retained after cooling specimens to -210°C can be used as an indication of the grain size. The dashed line shows the empirically-estimated relationship between magnetite grain size and remanence retention (Halgedahl & Jarrard, 1995). The grey region shows the average magnetite grain size distribution in the measured BIF specimens.

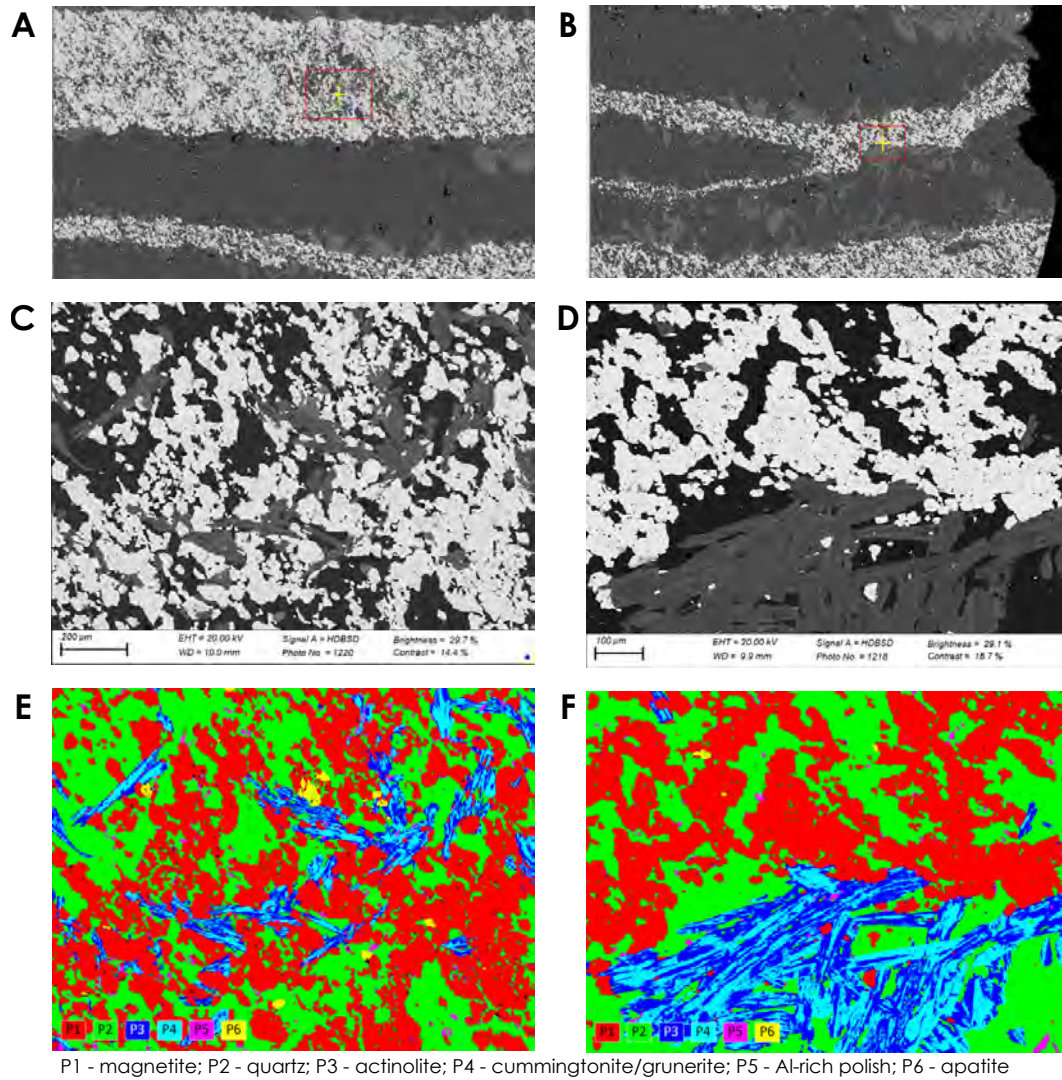


Figure 4. SEM analysis of BIF specimen C18. **A** and **B** show the regions of interest outlined in red. **C** and **D** show backscattered electron images of the regions of interest. **E** and **F** Show EDS phase maps highlighting the bands defined by quartz (green) and magnetite (red), with minor amphibole (intergrown cummingtonite/grunerite and actinolite; light and dark blue) and apatite (yellow). The pink phase is aluminium from the polish and is not a real phase.

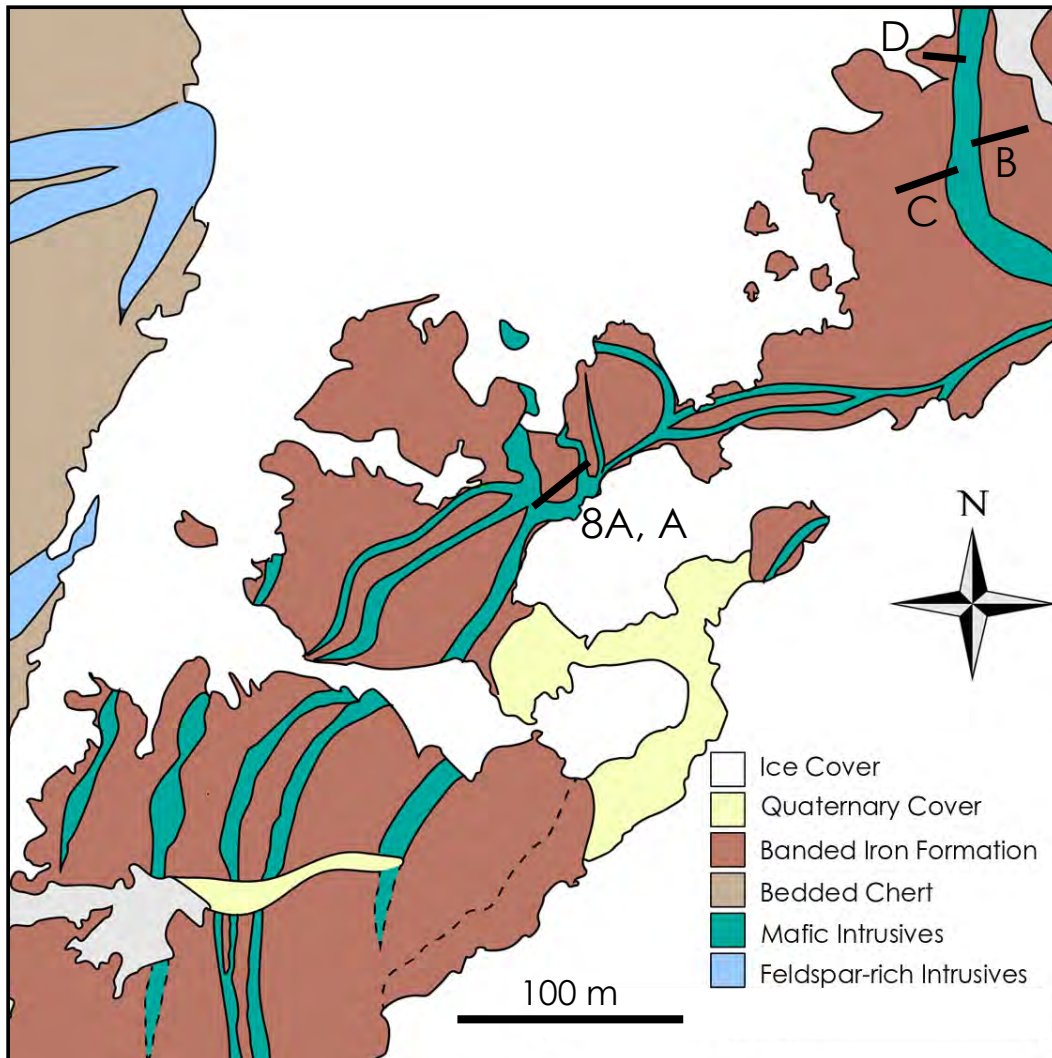


Figure 5. A Geological map of the northernmost extent of the northeast ISB ($65^{\circ}9.6'$ – $12.6'$ N and $49^{\circ}48'$ – $45'$ W), which was well-exposed due to minimal perennial snow in July 2019. The location of baked contact tests 8A/A, B, C and D are shown by black lines. Field photographs showing **B** the mafic intrusives and banded iron formation units and **C** the bedded chert and feldspar-rich intrusive units shown on the geological map. Pencil for scale.

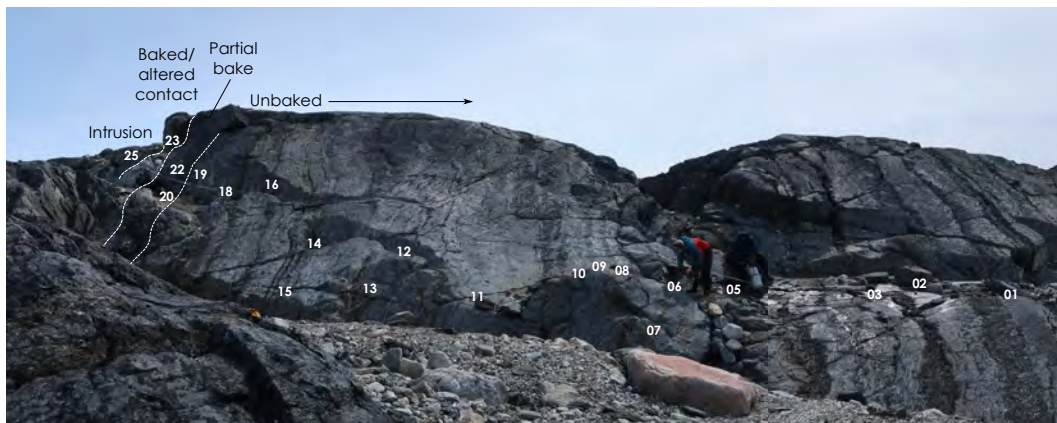


Figure 6. An example of a paleomagnetic baked contact test at Site C. The numbers show the location of each specimen drilled across the section. People for scale.

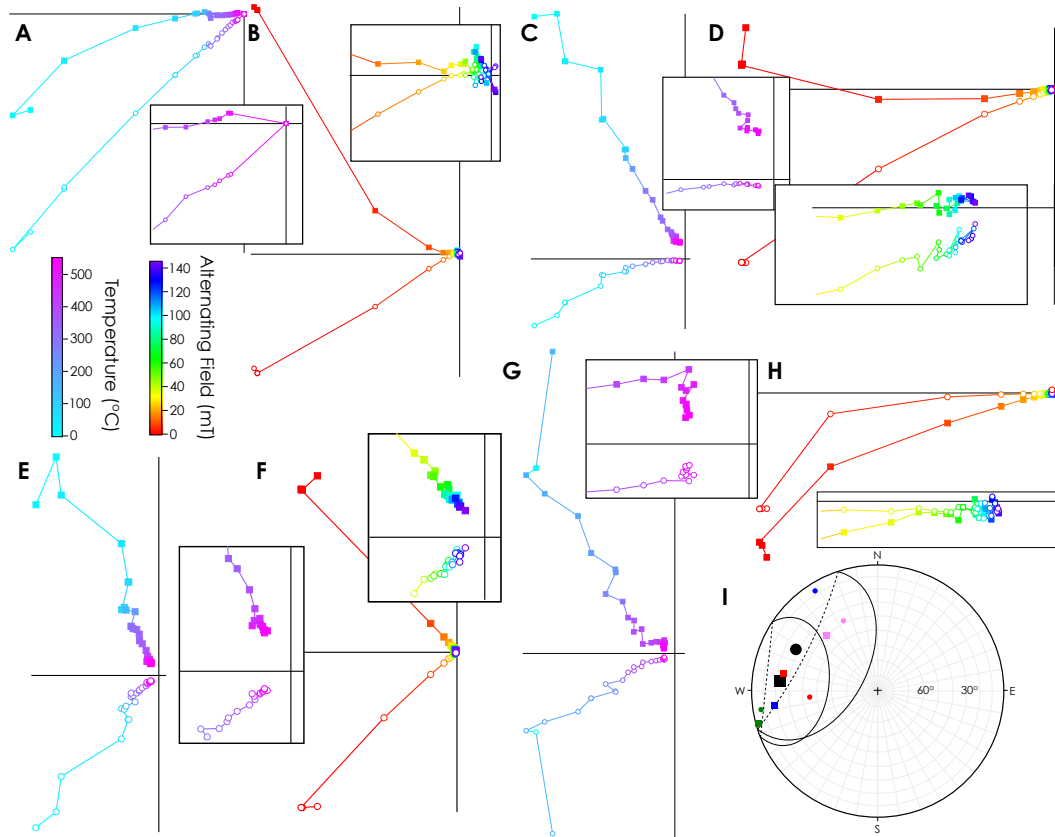


Figure 7. Thermal and AF demagnetization zijderveld diagrams for unbaked BIF specimens C01, C02, C04 and C05 from site C. Zijderveld diagrams are shown using ‘E, Horizontal’ and ‘N, Up’ as the x, y projection and inclination and declination are shown by open circles and closed squares, respectively. Thermal demagnetization zijderveld diagrams are shown with temperature increasing from cyan to magenta. AF demagnetization zijderveld diagrams are shown with AF strength increasing from red to blue. For each zijderveld, the high temperature or high coercivity component is shown by the inset. (A), (C), (E) and (G) show the thermal demagnetization zijderveld diagrams for C01, C02, C04 and C05, respectively. (B), (D), (F) and (H) show the AF demagnetization zijderveld diagrams for C01, C02, C04 and C05, respectively. (I) An equal area, lower hemisphere stereonet projection showing recovered HT and HC directions as circles and squares, respectively. C01 is shown in red, C02 is shown in blue, C04 is shown in green and C05 is shown in pink.

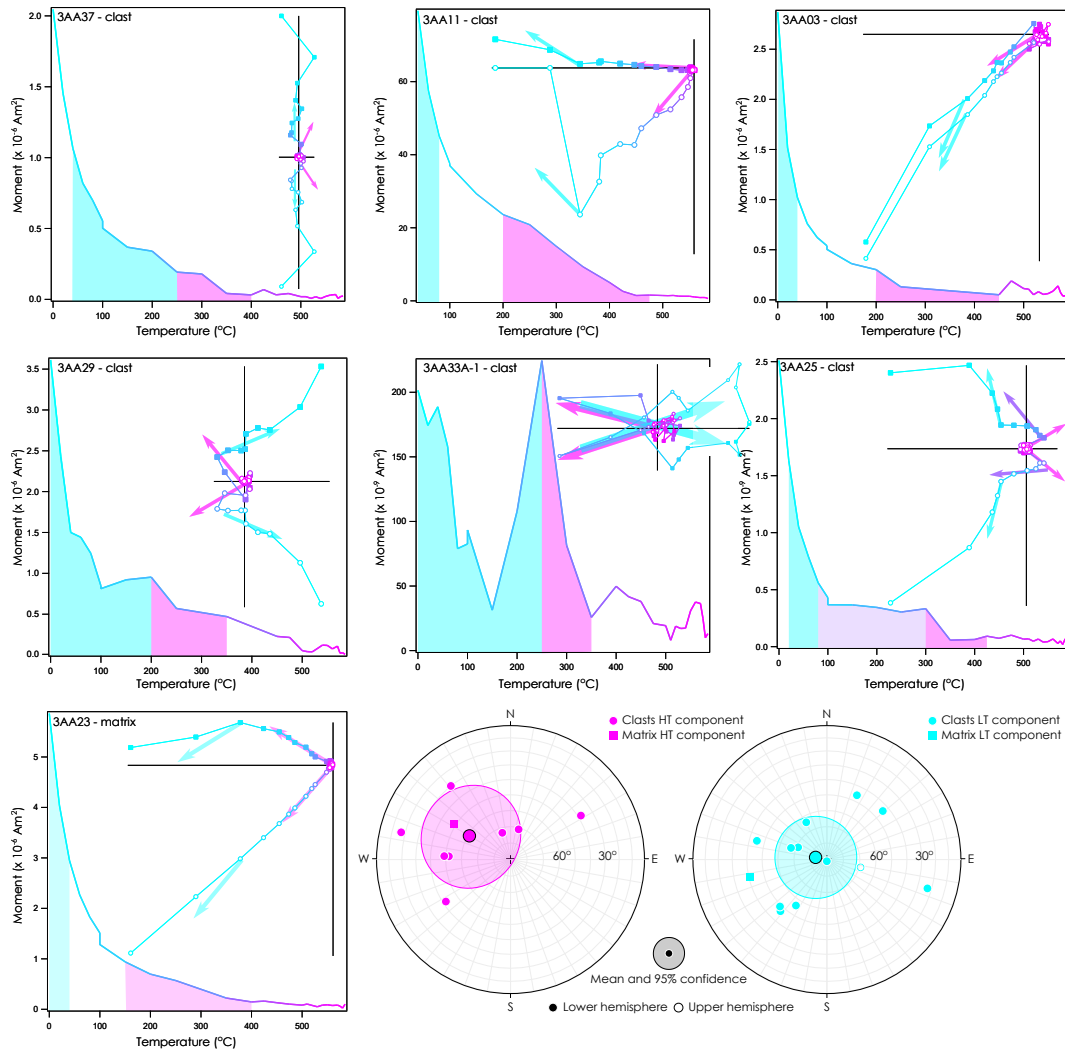


Figure 8. Six clasts (3AA11, 3AA03, 3AA29, 3AA33A-1, 3AA37 and 3AA25) and 1 matrix specimen (3AA23) exhibit well defined high ($> 200^{\circ}\text{C}$) and low ($< 200^{\circ}\text{C}$) temperature components. For each specimen, a moment vs demagnetization step plot is shown. The area under the plot indicates the temperature range over which high (pink) and low (blue) temperature components were fitted. Zijderveld diagrams are shown using ‘E, Horizontal’ and ‘N, Up’ as the x, y projection and inclination and declination are shown by open circles and closed squares, respectively. Closed square show the declination and open circles shown the inclination. The direction of components are highlighted by pink, purple and blue arrows for HT, MT and LT components, respectively. The two equal area stereonet projections show the HT and low temperature components, which both show a statistically significant direction indicating their magnetization is non-random.

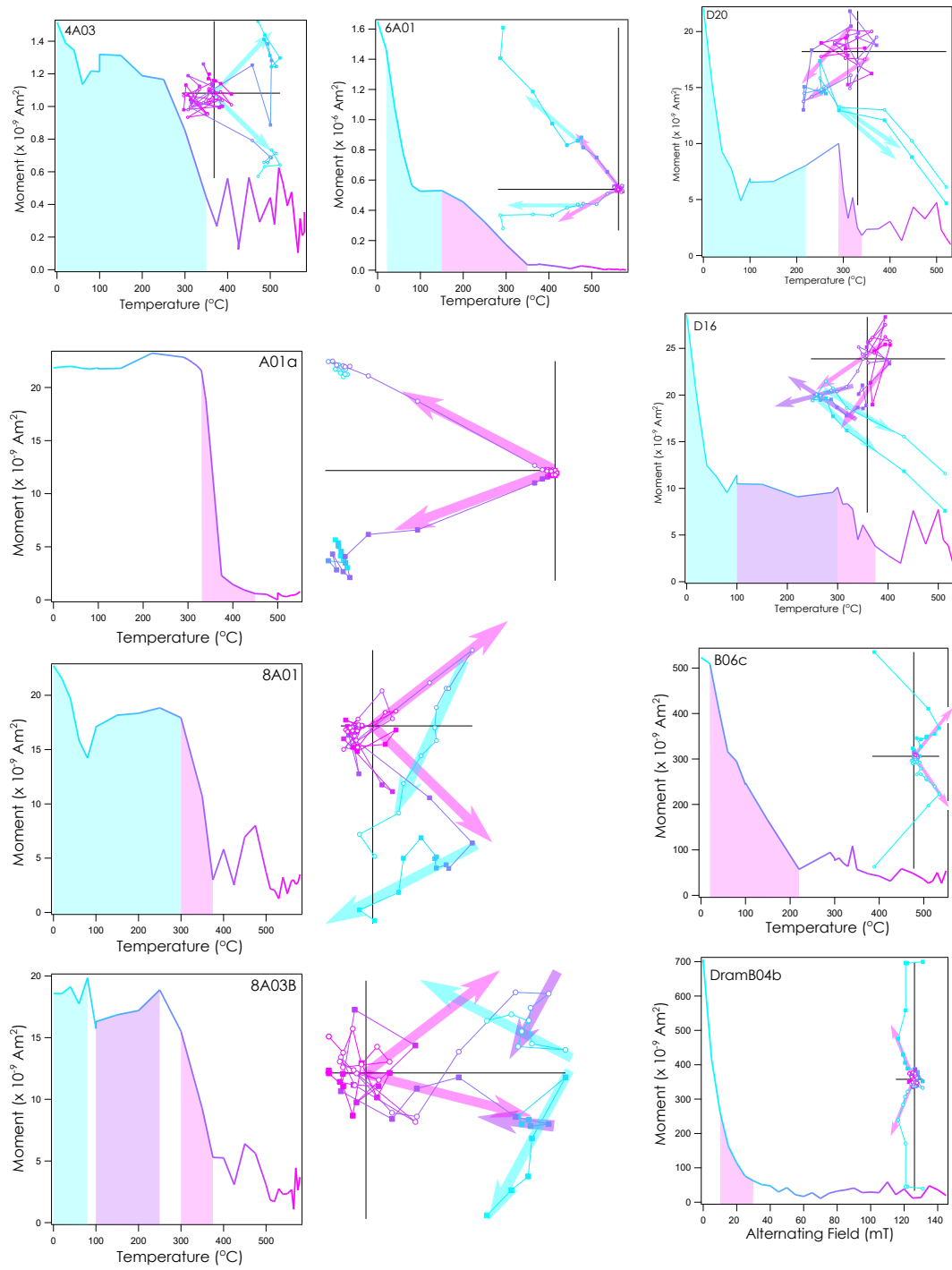


Figure 9. The thermal and AF demagnetization behaviour of the Ameralik dykes observed at sites 4A, 6A, 8A/A, B and D.

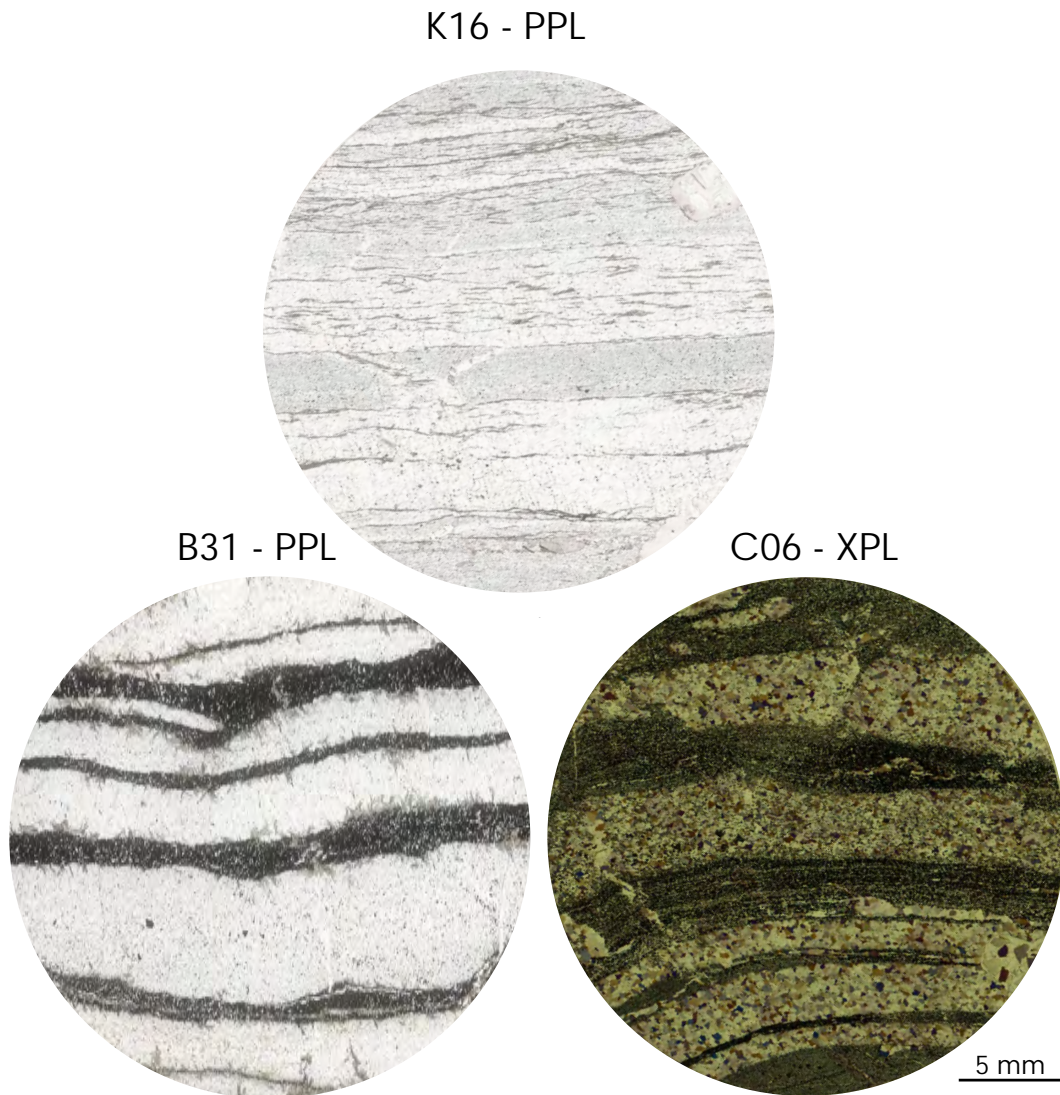


Figure 10. Top: A plane polarized light (PPL) image of specimen K16 shows an example of the bedded chert in the northernmost part of the northeast ISB. Bands are visible, although the darker bands contain only minimal magnetite, in contrast to the BIF. Bottom left: A PPL image of B31, a typical specimen of BIF exhibiting grunerite, actinolite and cummingtonite growing along the edges of the magnetite-quartz bands. Bottom right: A cross-polarized light (XPL) image of specimen C06 showing the grain size of and distribution of quartz. Note that the section is slightly thick and therefore the birefringence colours of quartz are higher than typical.

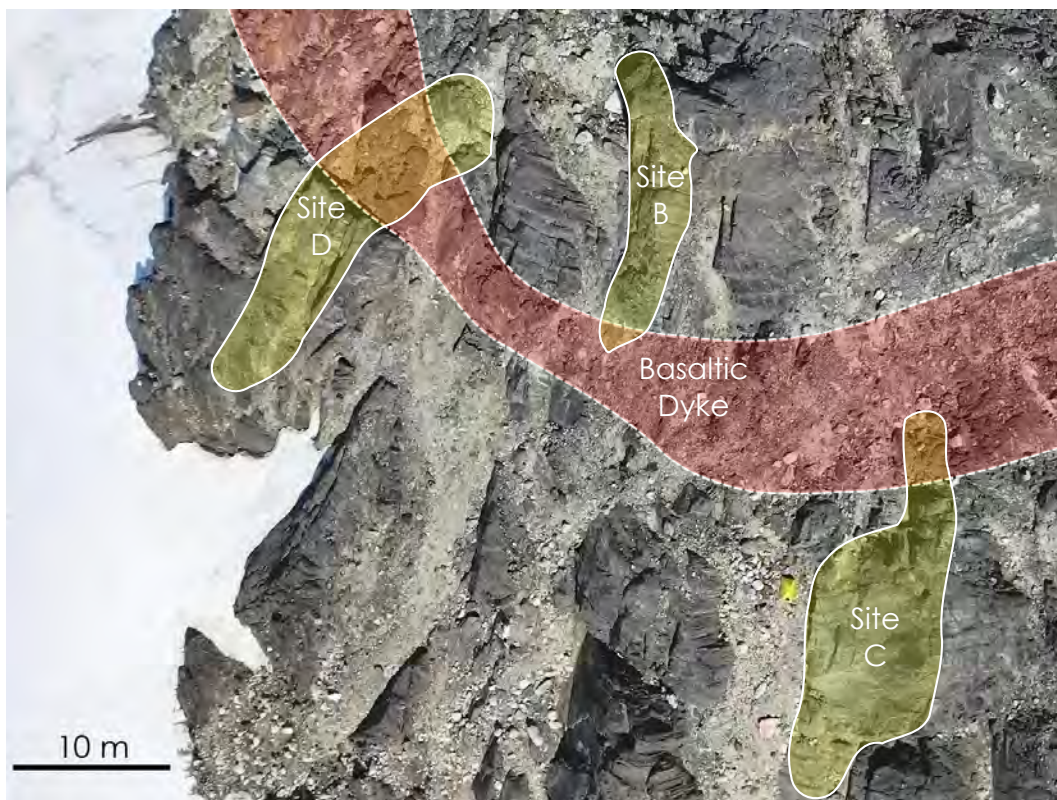


Figure 11. The relative locations of sites B, C and D which all sample the same Ameralik dyke. Aerial image taken by drone.

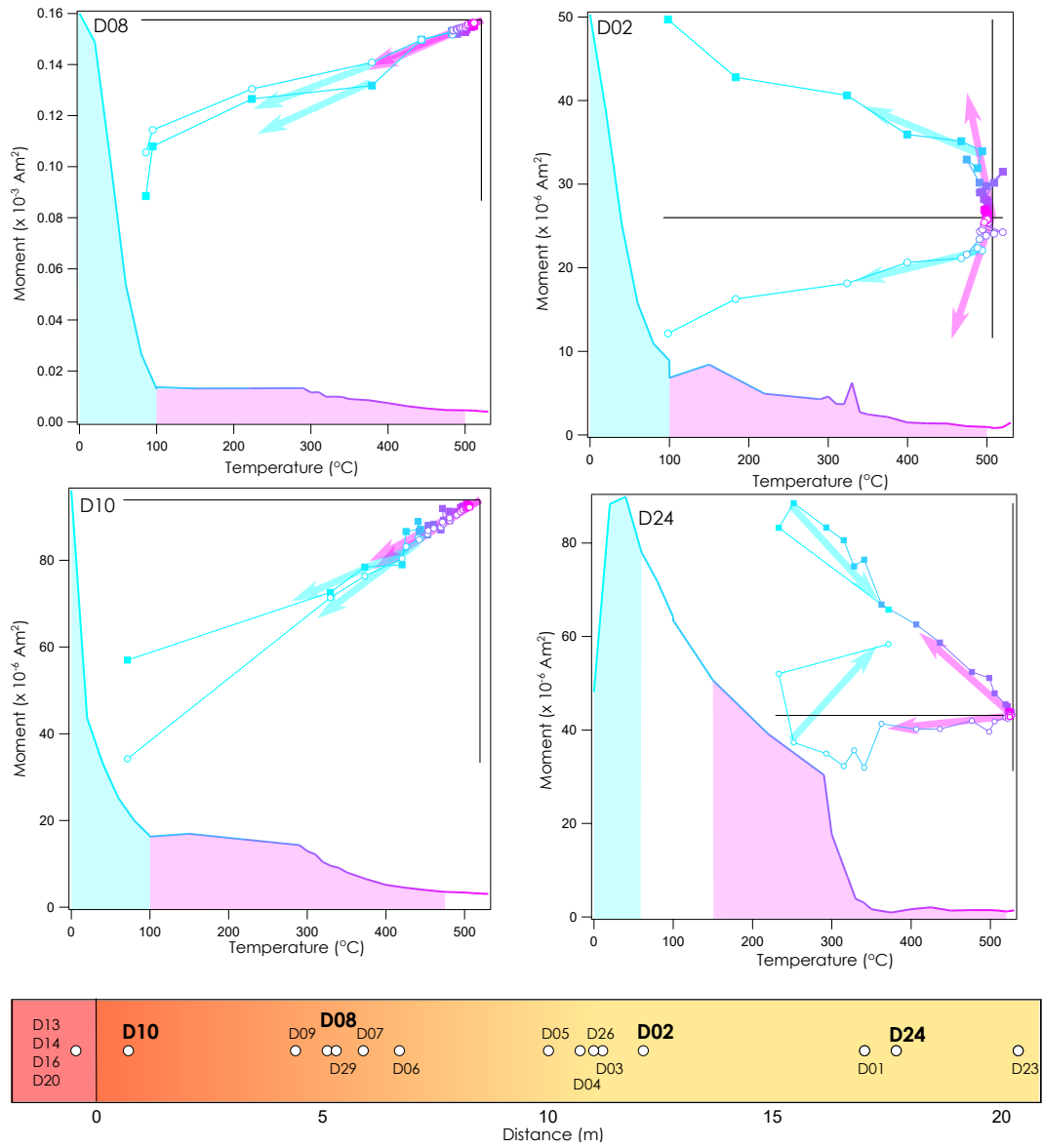


Figure 12. Site D baked contact test. Representative demagnetization behaviour is shown for specimens D10, D08, D02 and D24 which represent the BIF close to the contact and the BIF far from the contact, respectively. The distances of each specimen from the contact are shown in the bottom panel. Zijderveld diagrams are shown using ‘E, Horizontal’ and ‘N, Up’ as the x, y projection and inclination and declination are shown by open circles and closed squares, respectively. LT, MT and HT components are shown in blue, purple and pink, respectively.

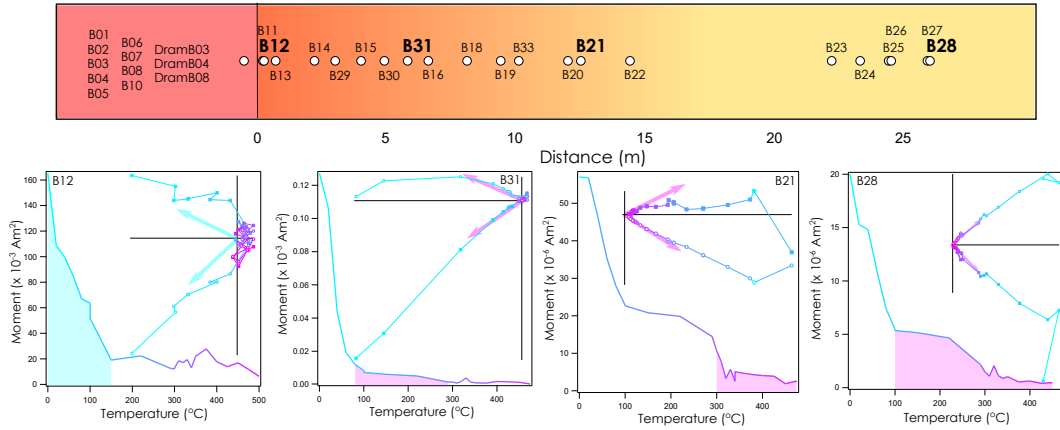


Figure 13. Site B baked contact test. Representative demagnetization behaviour is shown for specimens B12, B31, B21 and B28 which represent the BIF close to the contact and the BIF far from the contact, respectively. The distances of each specimen from the contact are shown in the bottom panel. Zijderveld diagrams are show using ‘E, Horizontal’ and ‘N, Up’ as the x, y projection and inclination and declination are shown by open circles and closed squares, respectively. LT, MT and HT components are shown in blue, purple and pink, respectively.

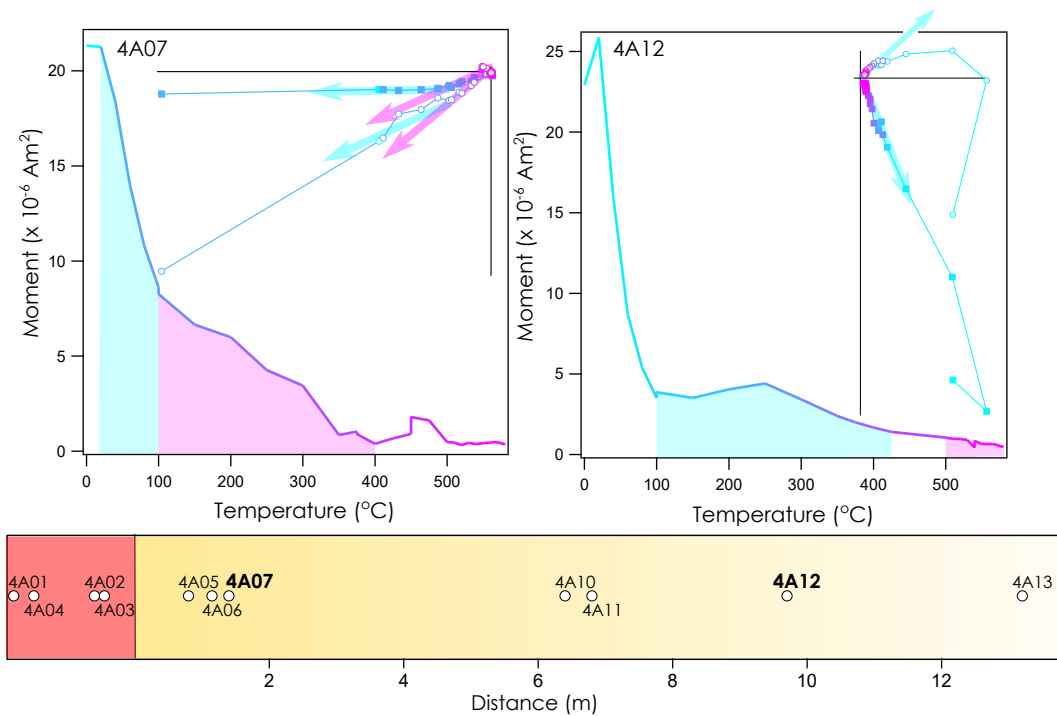


Figure 14. Site 4A baked contact test. Representative demagnetization behaviour is shown for specimens 4A07 and 4A12, which represent the BIF close to the contact and the BIF far from the contact, respectively. The distances of each specimen from the contact are shown in the bottom panel. Zijderveld diagrams are show using ‘E, Horizontal’ and ‘N, Up’ as the x, y projection and inclination and declination are shown by open circles and closed squares, respectively. LT, MT and HT components are shown in blue, purple and pink, respectively.

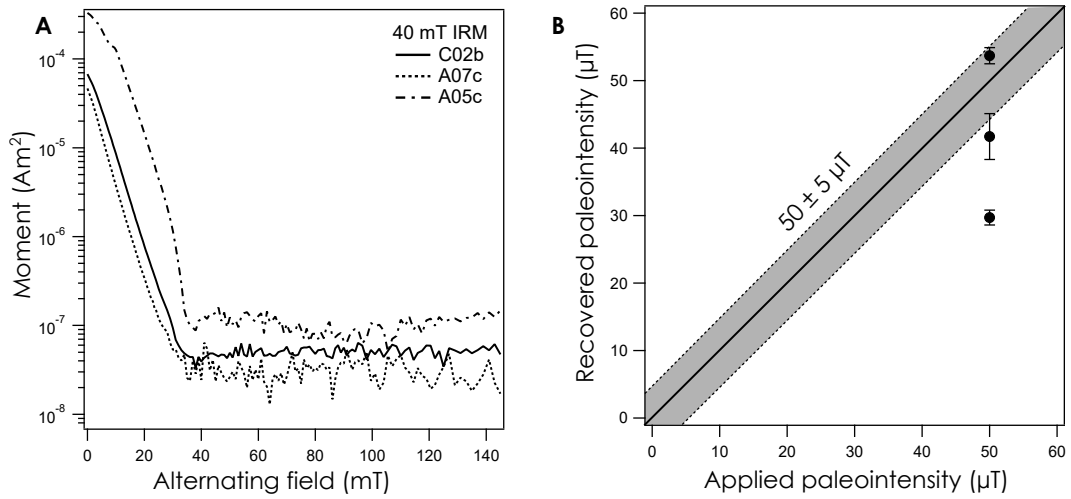


Figure 15. **A** A 40 mT IRM was applied to each sample and was efficiently acquired over that field range for specimens A05c, A07c and C02b. **B** The fidelity of specimens was tested by calculating paleointensities by comparing a $50 \mu\text{T}$ ARM to the 40 mT IRM. The grey region shows the arbitrary cut-off for acceptable paleointensity estimates, which represents values within 10 % of the true value

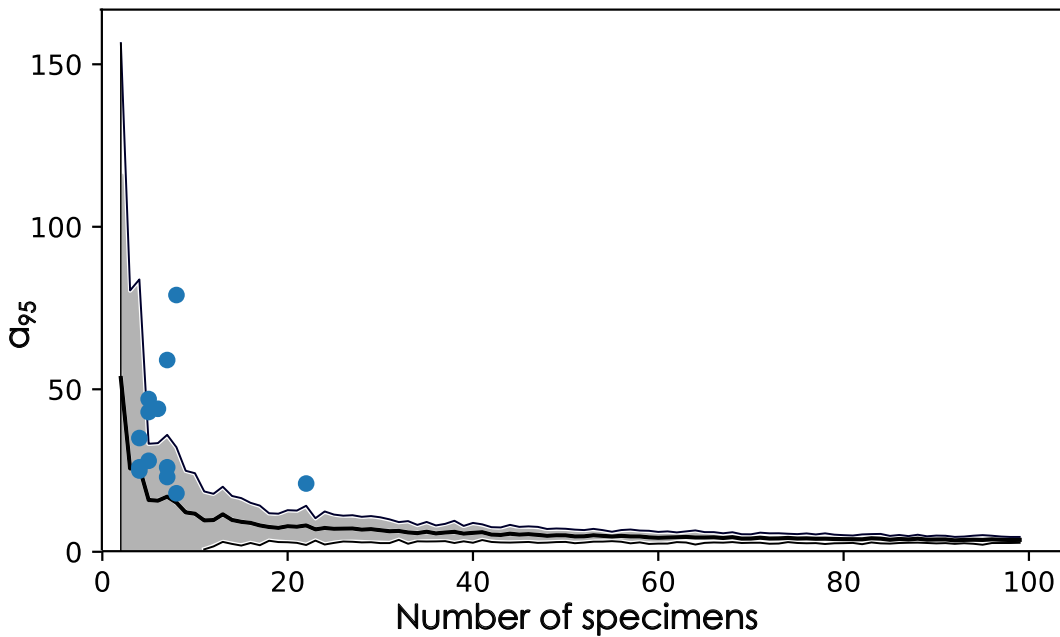


Figure 16. A graph showing the mean and two standard deviations in the value of α_{95} versus the number of specimens used to calculate Fisher statistics sampled from a model for paleosecular variation of the geomagnetic field (Tauxe & Kent, 2004). The blue dots show the number of specimens and α_{95} directions recovered from the BIF at Sites 6A, 8A/A, B, C and D demonstrating that most of the observed scatter can be explained by secular variation and averaging over a small number of specimens.

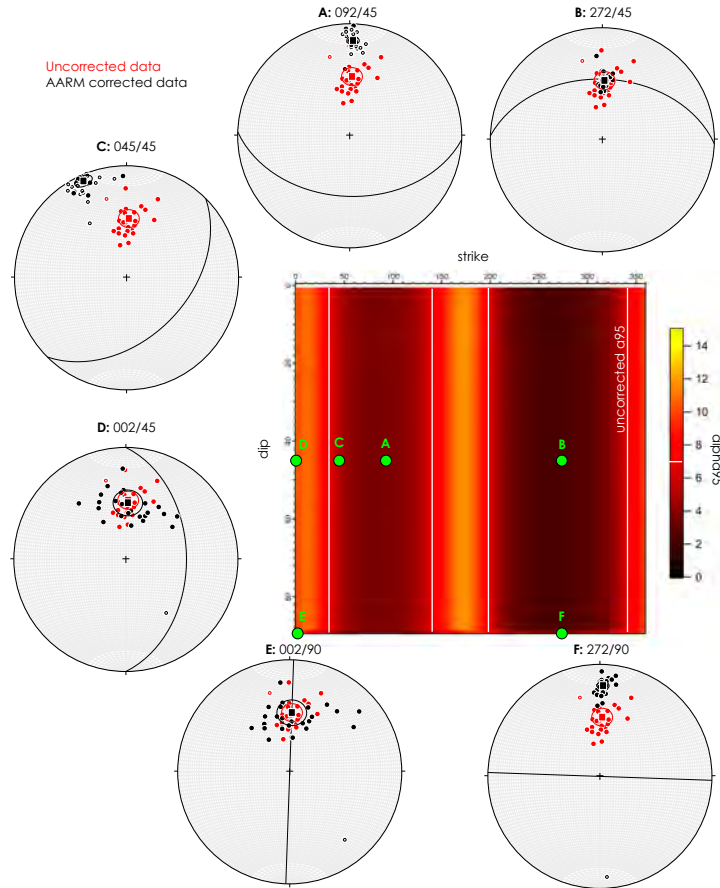


Figure 17. We take a sample of 25 directions with a mean trend and plunge of $46^\circ/002^\circ$ and $\alpha_{95} = 7^\circ$ and apply an anisotropy correction assuming anisotropy that is isotropic within a plane and the magnetic susceptibility is four times stronger in the plane compared to perpendicular to the plane (i.e., the anisotropy factor is $P = 4$). We change the orientation of the plane to show how α_{95} varies. The directions become more scattered if the strike of the plane is parallel or anti-parallel to the magnetization direction. The clustering improves if the strike of the plane is perpendicular to the magnetization direction.

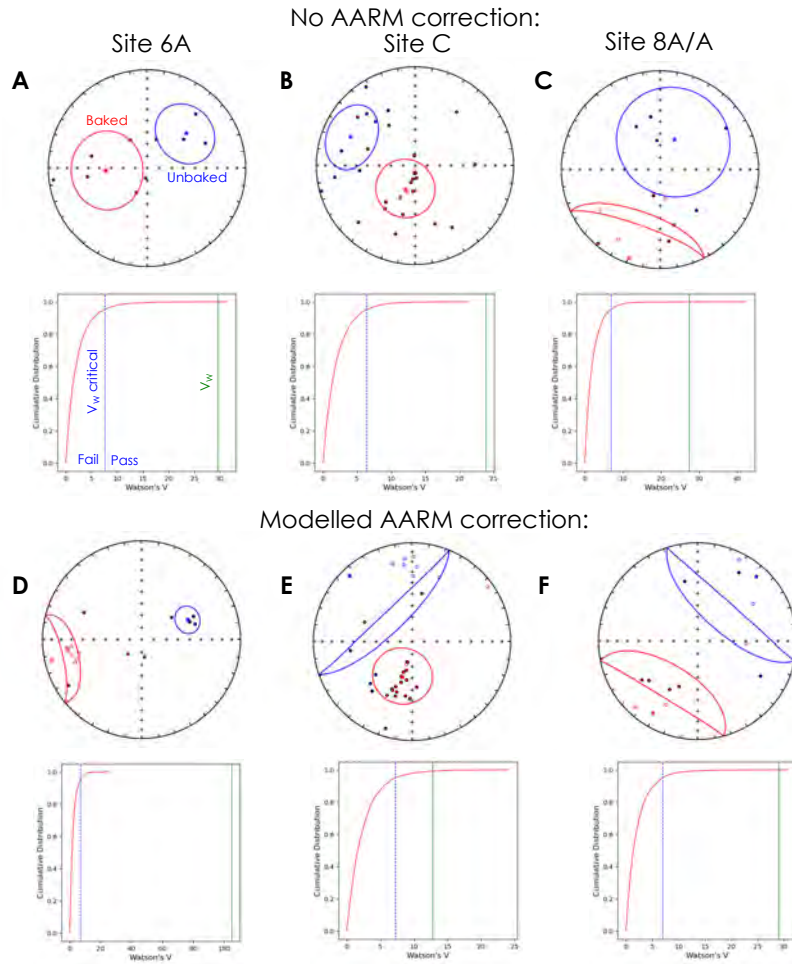


Figure 18. A hypothetical AARM correction was applied to each site assuming the anisotropy is coplanar with the bands, isotropic in the plane of the bands and that the magnetic susceptibility is four times stronger in the plane compared to perpendicular to the plane (i.e., the anisotropy factor is $P = 4$). **A**, **B** and **C** show the directions of the unbaked and baked directions prior to any AARM correction for sites 6A, C and 8A/A, respectively. All three sites pass our pseudo-baked contact tests. **D**, **E** and **F** show the same three sites after applying our hypothetical AARM correction. They all still pass the pseudo-baked contact test showing that the anisotropy correction does not impact our results.

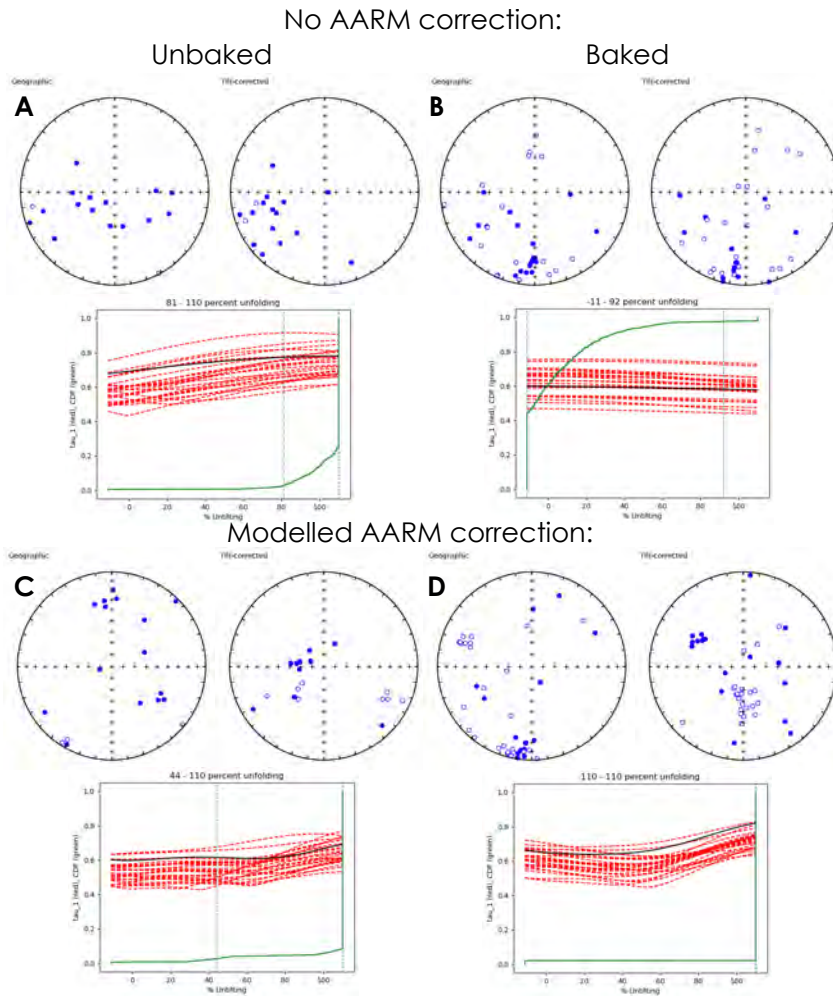


Figure 19. A hypothetical AARM correction was applied to each site assuming the anisotropy is coplanar with the bands, isotropic in the plane of the bands and that the magnetic susceptibility is four times stronger in the plane compared to perpendicular to the plane (i.e., the anisotropy factor is $P = 4$). **A** and **B** show the fold test for the unbaked and baked directions that passed our pseudo-baked contact tests prior to any AARM correction. The unbaked fold test passes while the baked fold test fails. **C** and **D** show the unbaked and baked fold test after applying our hypothetical fold test. In this case, we find that both the unbaked and baked fold tests pass.